RRFM

EUROPEAN RESEARCH REACTOR CONFERENCE 2013

Transactions

St. Petersburg, Russia
21 -25 April 2013

EUROPEAN NUCLEAR SOCIETY

ENS CONFERENCE

supported by:

ROSATOM

organised in collaboration with:

IAEA

European Nuclear Society
avenue des Arts 56
1000 Brussels, Belgium
Phone + 32 2 505 30 54
Fax +32 2 502 39 02
E-mail ens@euronuclear.org
Internet www.euronuclear.org

ISBN 978-92-95064-18-8

These transactions contain all contributions submitted by 19 April 2013.

Table of Contents:

BENCHMARK CRITICALITY EXPERIMENTS FOR URANIUM-WATER HETEROGENEOUS CONFIGURATIONS WITH UZRCN LOW ENRICHED NUCLEAR FUEL	Sikorin, S. (1); Mandzik, S. (1); Polazau, S. (1); Hryharovich, T. (1); Damarad, Y. (1); Palahina, Y. (1) 1 - The Joint Institute for Power and Nuclear Research – Sosny of the National Academy of Sciences of Belarus, Belarus
CONCEPT OF THE RESEARCH REACTOR FOR THE REPUBLIC OF BELARUS	Sikorin, S. (1); Kuvshinov, V. (1); Kazazyan, V. (1); Hryharovich, T. (1); Mikhalevich, A. (2); Akhramovich, A. (2); Kolos, V. (2) 1 - The Joint Institute for Power and Nuclear Research – Sosny of the National Academy of Sciences of Belarus, Belarus 2 - The Institute of Power of the National Academy of Sciences of Belarus, Belarus
EXPERIMENTAL MEASUREMENTS OF A VOLUME, PRESSURE AND COMPOSITION OF GAS INSIDE SWELLING BUBBLES FORMED IN IRRADIATED FUEL ELEMENTS CONTAINING U-MO DISPERSION FUEL	Gosolov, O. A. (1); Nickolkin, V. N. (1); Lyutikova, M. S. (1); Bedin, V. V. (1) 1 - Institute of Nuclear Materials, Russian Federation

HIGH RESOLUTION REACTOR MODELING FOR THE SIMULATION OF THE ACTIVITY DISTRIBUTION AND RADIATION FIELD AT THE GERMAN FRJ-2 RESEARCH REACTOR	Winter, D. (1); Abbasi, F. (1); Nabbi, R. (1); Simons, F. (1); Thomauske, B. (1); Damm, G. (2) 1 - RWTH Aachen - Institute of Nuclear Fuel Cycle (INBK), Germany 2 - Research Centre Juelich - Technical Infrastructure (TB), Germany

CALCULATED AND EXPERIMENTAL JUSTIFICATION OF A POSSIBILITY TO PROVIDE TEMPERATURE CONDITIONS FOR STRUCTURAL MATERIALS IRRADIATED IN REACTOR BOR-60	Varivtcev, A. (1); Eremin, S. (1); Zhemkov, I. (1); Kozolup, A. (1); Plotnikov, A. (1); Poglyad, N. (1) 1 - JSC "SSC RIAR", Russian Federation
LIFETIME TESTS OF FUEL RODS WITH LOW NEUTRON POISONING	Klinov, A. (1); Kalinina, N. (1); Marikhin, N. (1); Pimenov, V. (1); Petelin, A. (1); Starkov, V. (1); Fedoseyev, V. (1); Mainskov, S. (1) 1 - JSC "SCC Research Institute of Atomic Reactors", Russian Federation


RRFM
EUROPEAN RESEARCH REACTOR CONFERENCE 2013
Russia
Saint Petersburg
21 - 25 April 2013

Poster

DIFFUSION COUPLES OF UMo/Zry IN DIFFERENT CONDITIONS

B. PICCHETTI, L. LEMOS, M. LOPEZ
Gerencia Ciclo Combustible Nuclear - CNEA
Avenida Libertador 8250, 1429, Buenos Aires - Argentina

Abstract

According to the results obtained in the fabrication process of UMo/Zry-4 miniplates [1], we decided to study diffusion couples in different conditions in order to evaluate the effect on the final product.

With this method we could assume that the temperature and compressive stress are important parameters that can modify the interaction between the components.

In this report we present the results obtained with diffusion couples in different conditions and a comparison with the observations made in the fabrication process.

Introduction

The decision to employ monolithic material was to increase the density of the fuel. Considering the properties of the zircalloy in the nuclear industry [2], it was employed as cladding in order to avoid the interaction between the nuclear material and the cladding. However, when the interaction lets to a stable compound, it can benefit the binding between the core and the cladding materials; when the compound is unstable, it can imply an obstacle in maintaining the pieces together.

According to the Mo-U-Zr Phase Diagram [3] at different temperatures, is expected to find compound variety in the interlayer observed in miniplates fabrication.

The parameters evaluated are: temperature, exposure time to the heat and compressive stress.

Materials and Methods

Two kinds of samples were studied: diffusion couples (specially made for this work) consisting of a piece of UMo and a piece of Zry-4 put in contact by a press; and samples taken from co-rolled miniplates.

Samples Preparation

The presses were exposed to two different temperatures: 760ºC and 950ºC.

The couple at 760ºC was made employing two samples of 10 mm width, 15 mm length and 4 mm thickness for zircalloy and 3 mm thickness for U7Mo alloy. The samples were polished up to #1500 grain paper and then finished with diamond paste. Two plates of stainless steel made the press tight with the pressure of two screws. Taking into account that at this temperature the UMo is in gamma phase and bcc structure and the zircalloy is in alpha phase and hcp structure [4,5], the couple was left in the furnace at 760ºC during 90 hours. After reaching this time, the sample was taken off and template in water to avoid the decomposition of gamma phase of UMo during the cooling.

The same treatment was applied to samples treated at 950ºC; one was left 90 hours in the furnace and the other 6 hours. Another different sample was made at 760ºC but without the press.

All the samples were mounted in an acrylic mould and, afterwards, polished. Finally, they were observed under Scanning Electron Microscope.

The miniplates were made by picture and frame process, employing as fuel different alloys of UMo (8 and 10 %) and Zry-4 as cladding. These materials were assembled and TIG welded at external borders. After that, the miniplates were hot co-rolled at 650ºC, 700ºC, 750ºC and 800ºC, all under the same compressive stress. One additional sample was co rolled at 650ºC under conditions of higher compressive stress.

The experimental conditions of each sample can be found in *tables 1* and *2*.

Sample	950-90-P	950-6-P	760-90-P	760-90
Temperature (ºC)	950	950	760	760
Exposure time (hours)	90	6	90	90
Press	Yes	Yes	Yes	No

Table 1: preparation conditions for the diffusion couples.

Sample	MP650	MP700	MP750	MP800	MP650-HF
Temperature (ºC)	650	700	750	800	650
Compressive Stress (MPa)	371-2394				4372-29152

Table 2: co-rolling conditions for the miniplates.

Results

The samples treated at 760ºC with and without press are shown in *figure 1*. According to this figure, no interaction layer is found in the sample without press; in contrast, the one with press do show a thin interlayer.

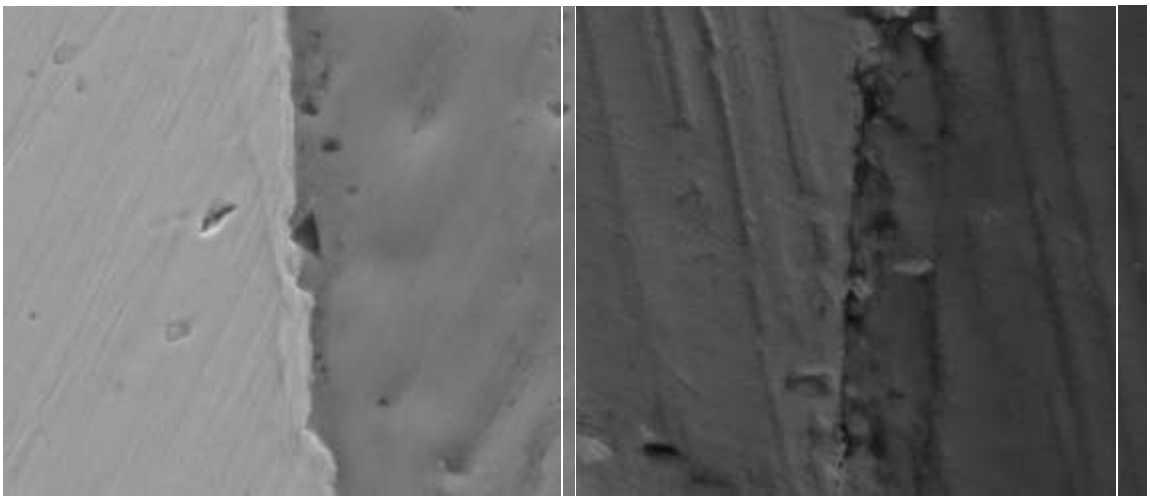

Figure 1: Presses treated at 760ºC and exposure time of 90 hours. Left: with press; Right: without press.

In *figure 2*, a similar interaction layer can be observed in both cases. These samples were made at 950ºC, with press and at different exposure times (6 and 90 hours).

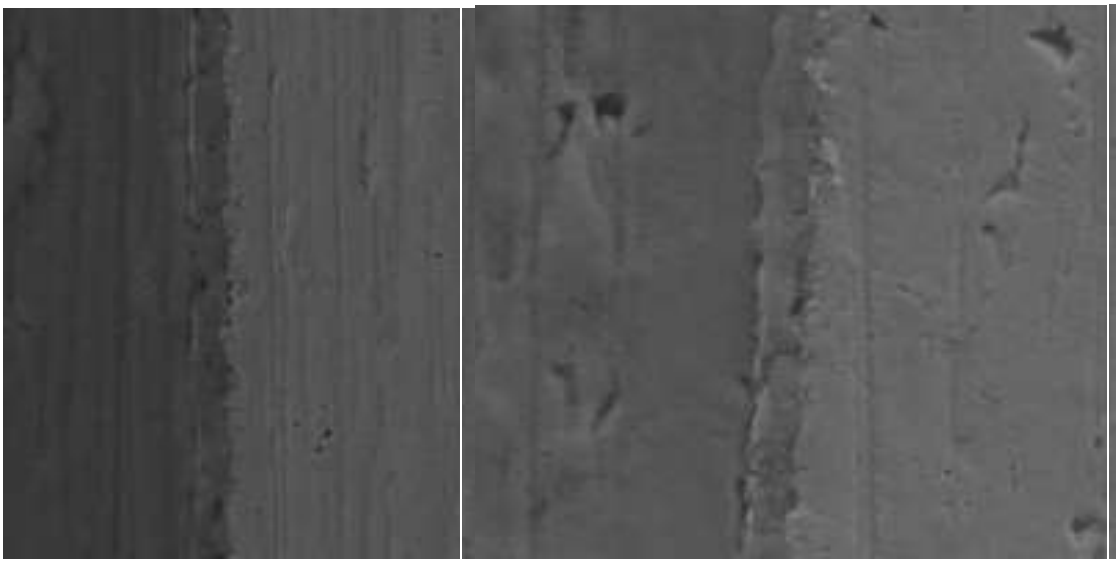

Figure 2: Presses treated at 950ºC with different exposure time. Left: 90 hours; Right: 6 hours.

In *figure 3* two SEM images are shown. Each one belongs to two samples made in the same condition of exposure time (90 hours), but at different temperature (760ºC and 950ºC). In the sample made at 950ºC can be seen that the interlayer is thicker than the one made at 760ºC.

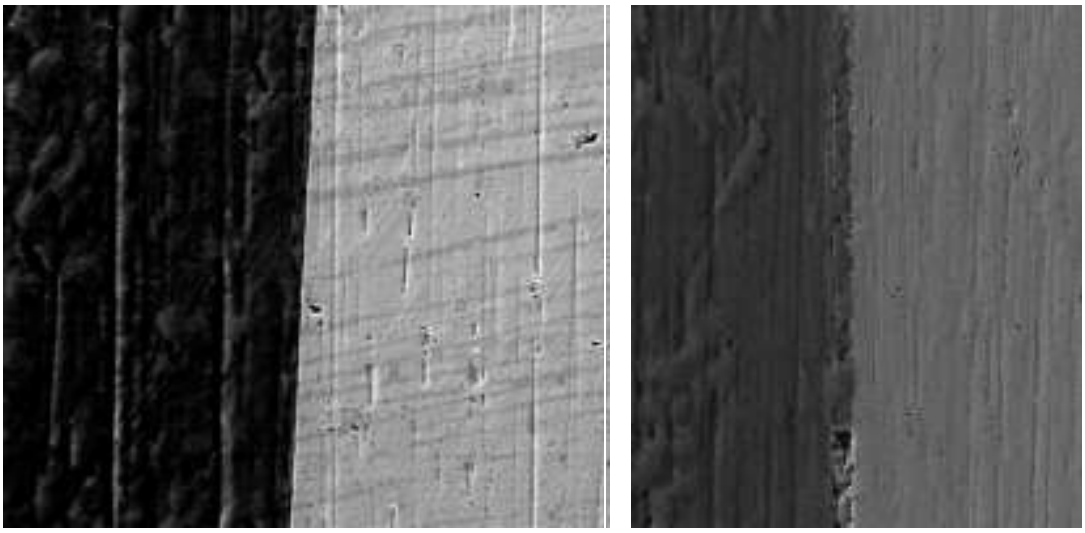

Figure 3: Samples with presses and exposure time of 90 hours, treated at different temperatures. Left: 760ºC; Right: 950ºC.

The study of the miniplates was performed at different temperatures, in each case, an EDAX analysis was done. In *figure 4 and 5* a SEM image and EDAX results obtained for a miniplate co-rolled at 650ºC and a compressive stress between 371 and 2394 MPa are shown; samples made in identical conditions but co-rolled at 700ºC, 750ºC and 800ºC can be seen in *figures 6 to 11*. When the temperature increases, a difference in the aspect and the composition of the interlayer is observed; the interlayer became thicker, and the relation U/Zr and U/Mo varies in that region. In the case of 800ºC can be clearly seen a zone rich in Mo (*Figure 10 and 11, EDAX 5,* the dark spots on the interlayer correspond to Molybdenum). In the proximity, a region poor in Mo could let Uranium to precipitate in alpha phase. More studies are needed to verify this fact.

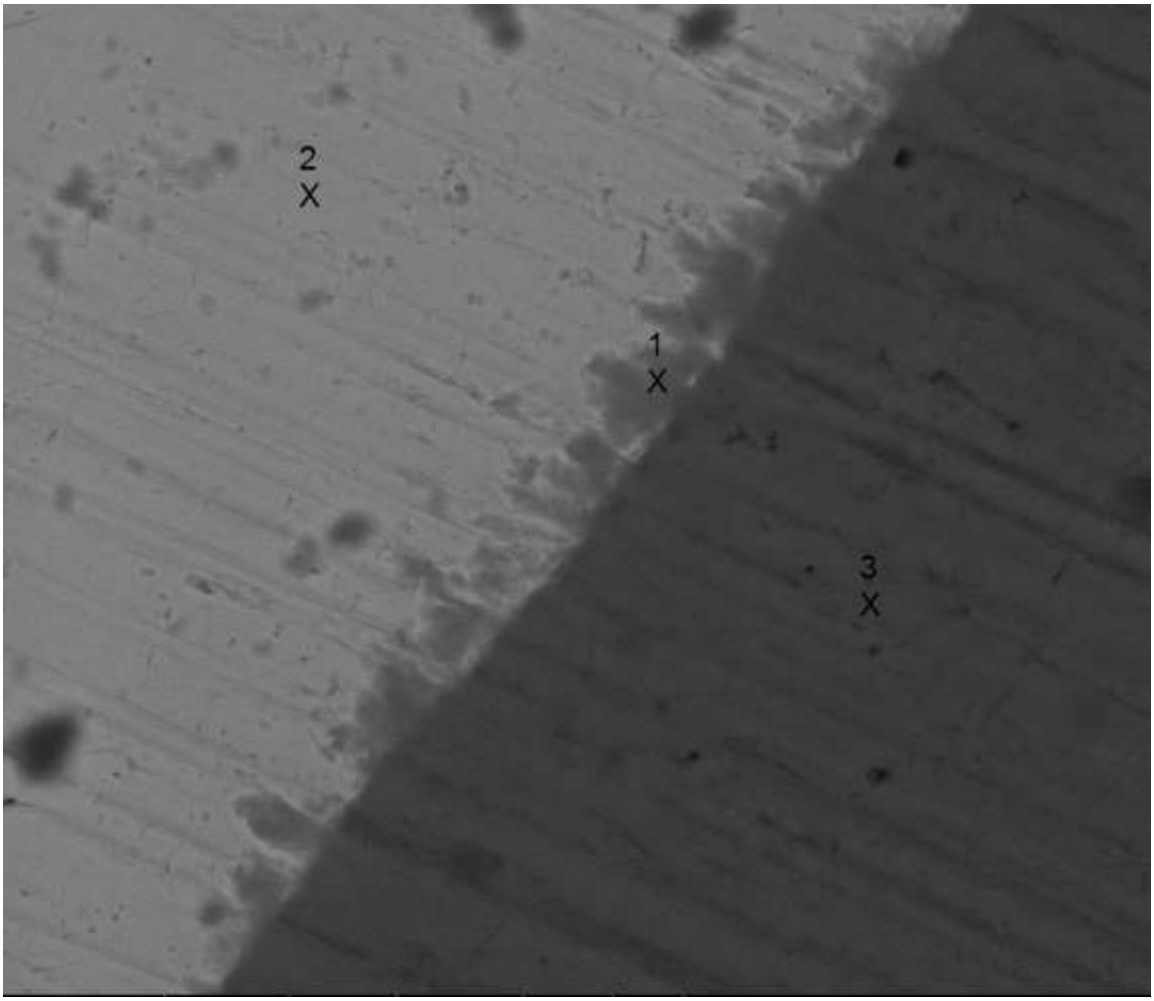

Figure 4: Miniplate co-rolled at 650ºC. In the SEM image the regions where and EDAX analysis was made are indicated. The results are shown in *figure 5*.

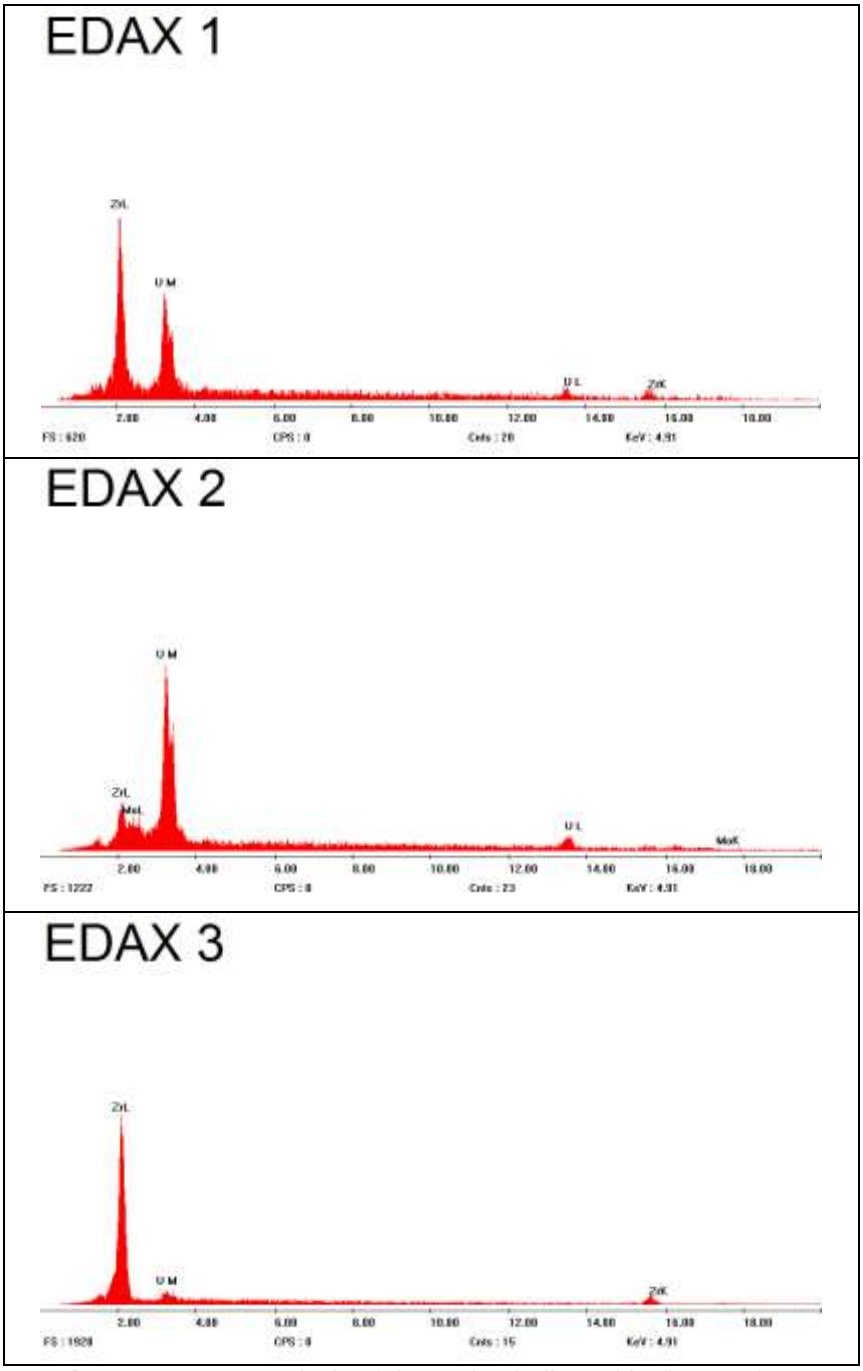

Figure 5: EDAX analysis of the region indicated in *figure 4* for a sample co-rolled at 650ºC.

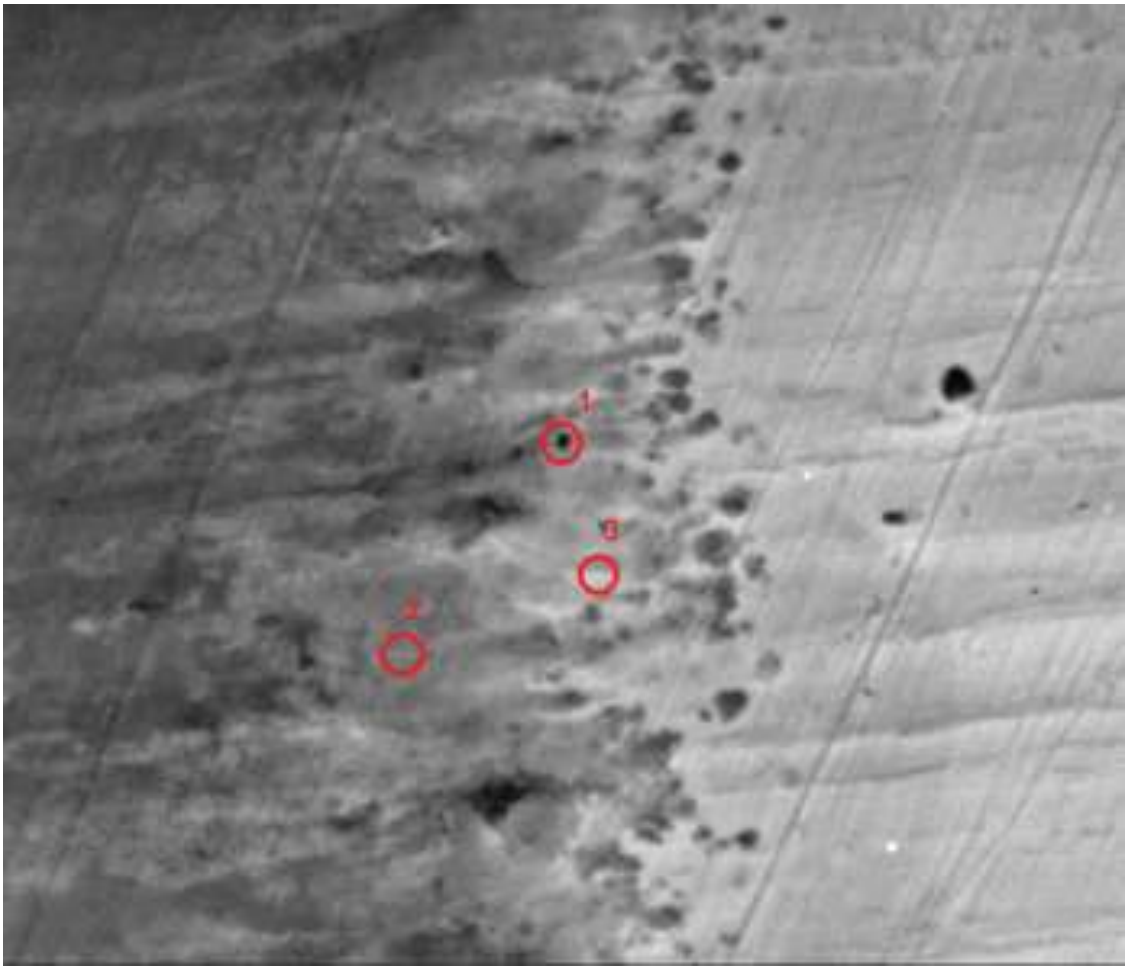

Figure 6: Miniplate co-rolled at 700ºC. In the SEM image the regions where and EDAX analysis was made are indicated. The results are shown in *figure 7*.

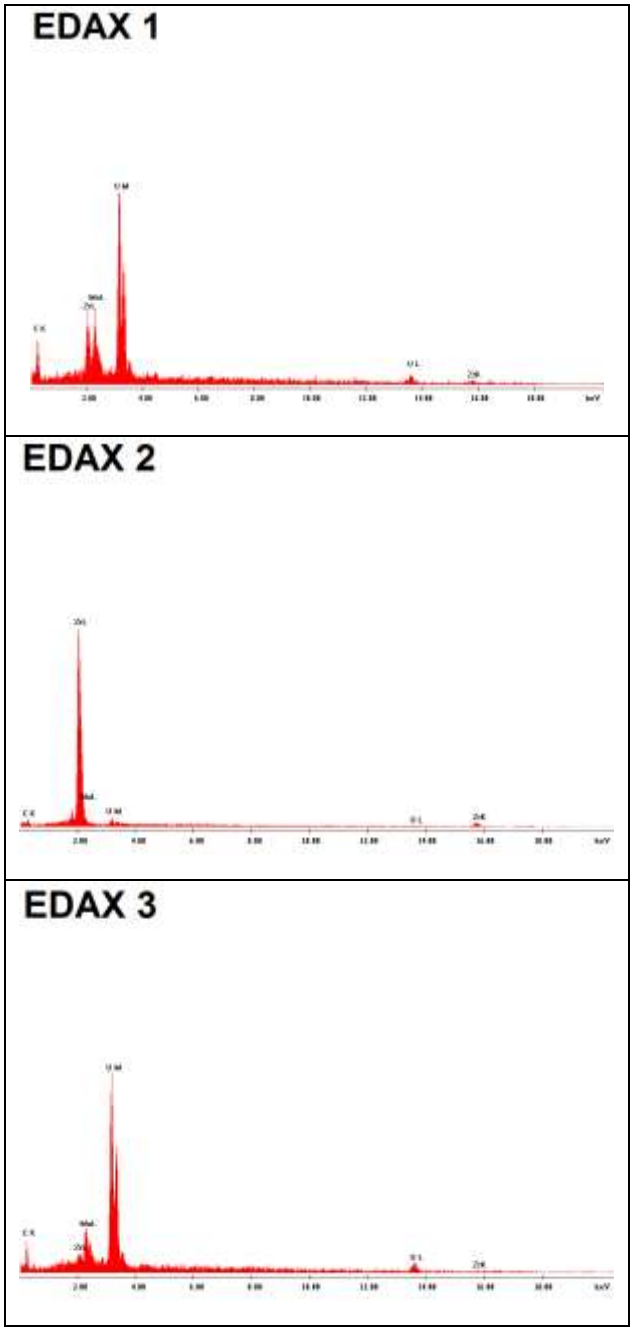

Figure 7: EDAX analysis of the region indicated in *figure 6* for a sample co-rolled at 700ºC.

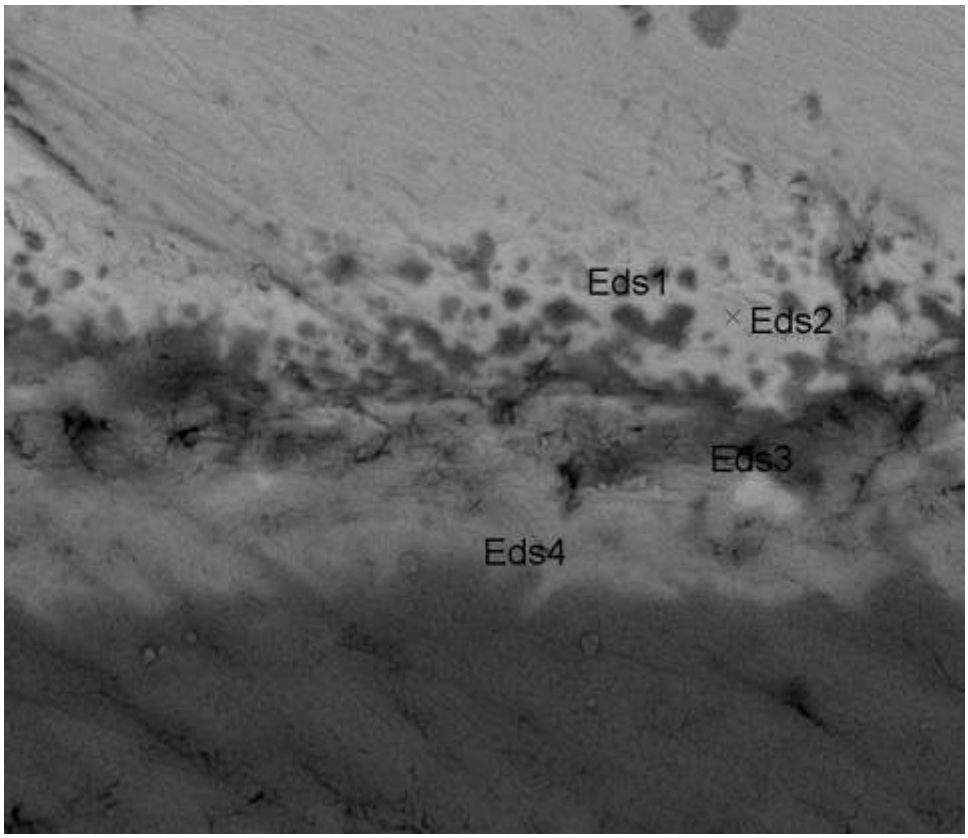

Figure 8: Miniplate co-rolled at 750ºC. In the SEM image the regions where and EDAX analysis was made are indicated. The results are shown in *figure 9*.

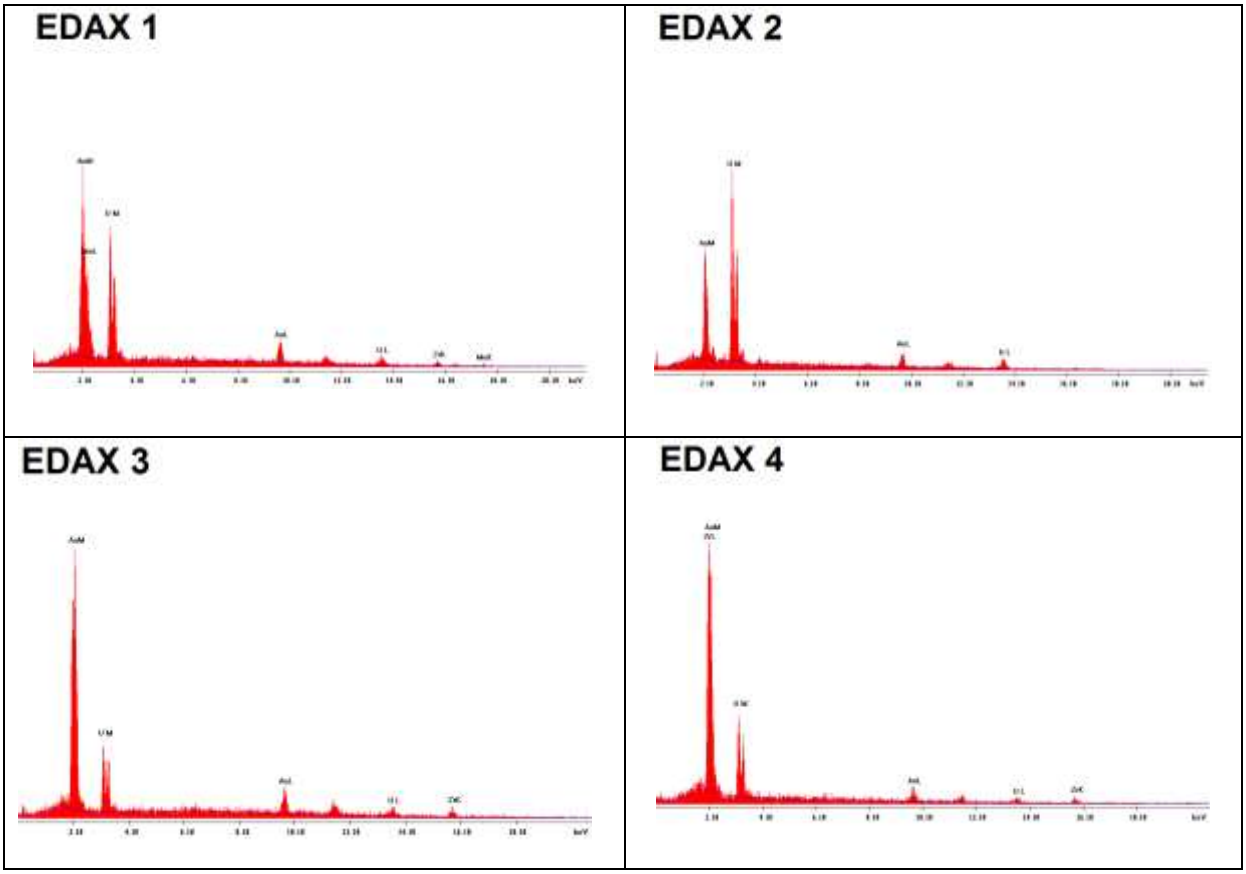

Figure 9: EDAX analysis of the region indicated in *figure 8* for a sample co-rolled at 750ºC.

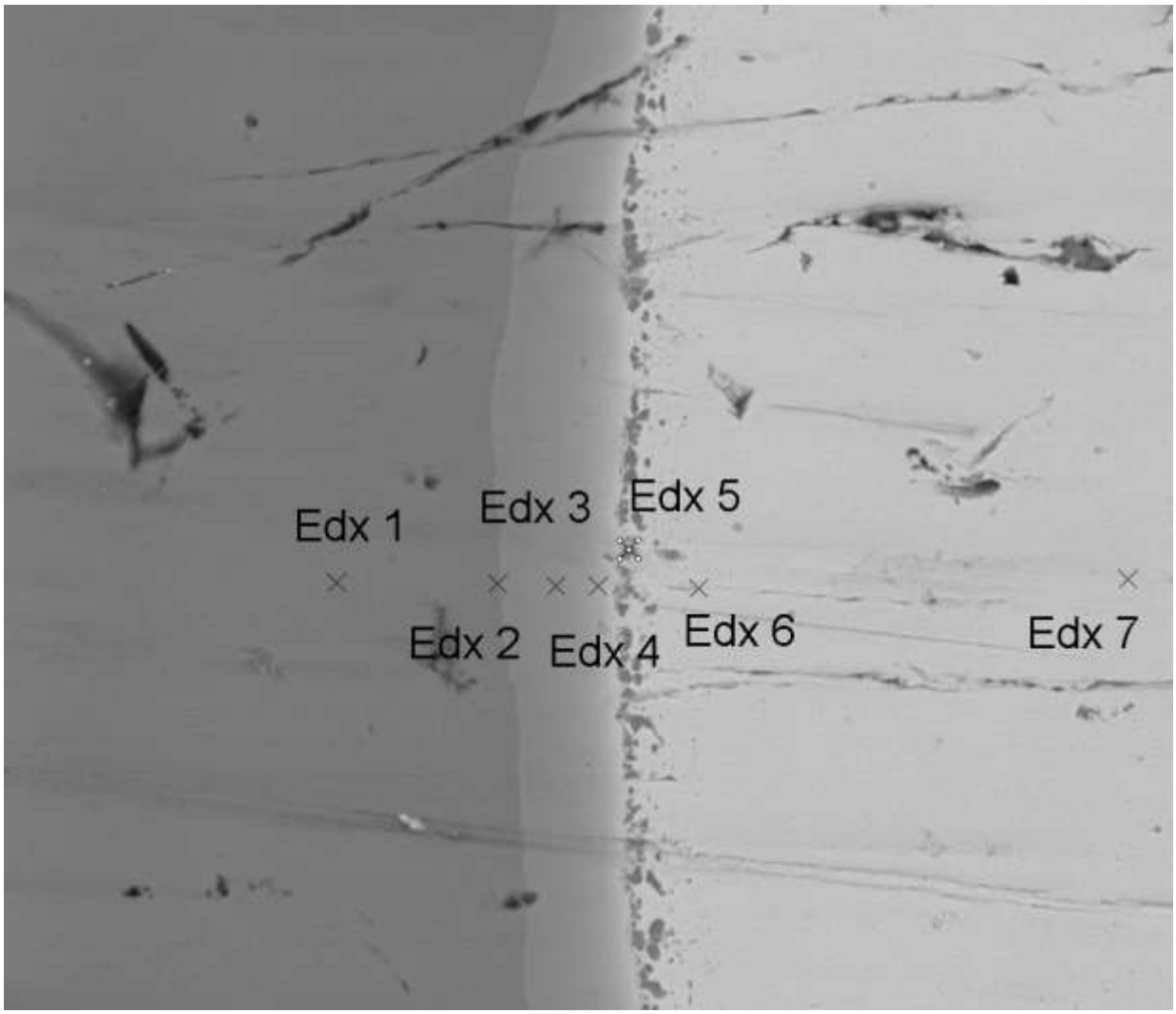

Figure 10: Miniplate co-rolled at 800ºC. In the SEM image the regions where and EDAX analysis was made are indicated. The results are shown in *figure 11*.

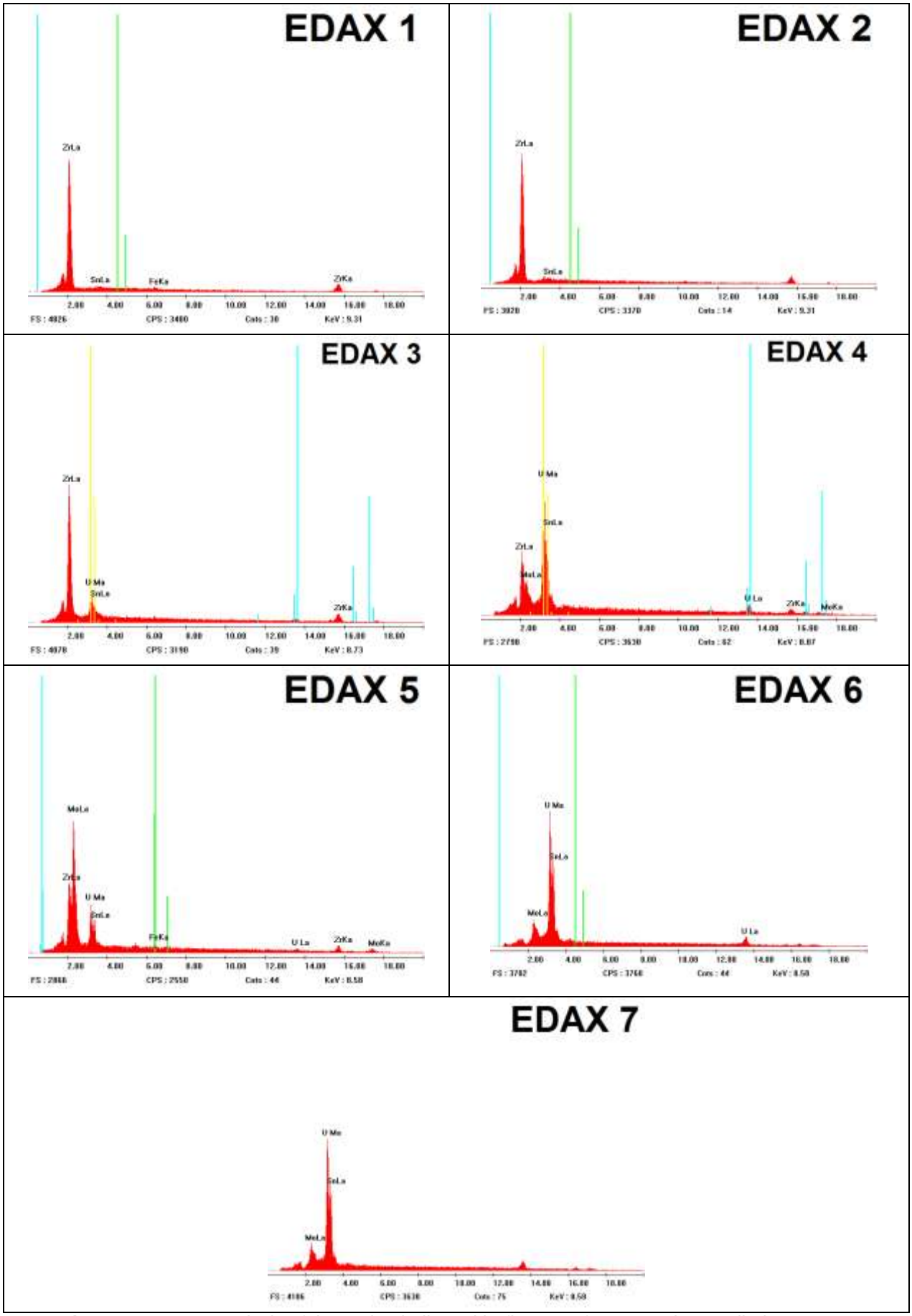

Figure 11: EDAX analysis of the region indicated in *figure 10* for a sample co-rolled at 800ºC.

The influence of the compressive stress on the interlayer appearance was studied on a miniplate co-rolled at 650ºC and compressive stress between 4372 and 29152 MPa. The results can be found in *figure 12*.

In these conditions can be clearly seen the interlayer. Different regions were analysed by EDAX, obtaining interesting results from the regions 1 and 2. The quantification indicates that in region 2, which corresponds to one of the dark spots seen on the interlayer, the relation U/Mo is smaller than in regions 1 and 3. This result leads to the conclusion that not only does the temperature benefits the accumulation of Molybdenum compounds in the interlayer, but so does the compressive stress.

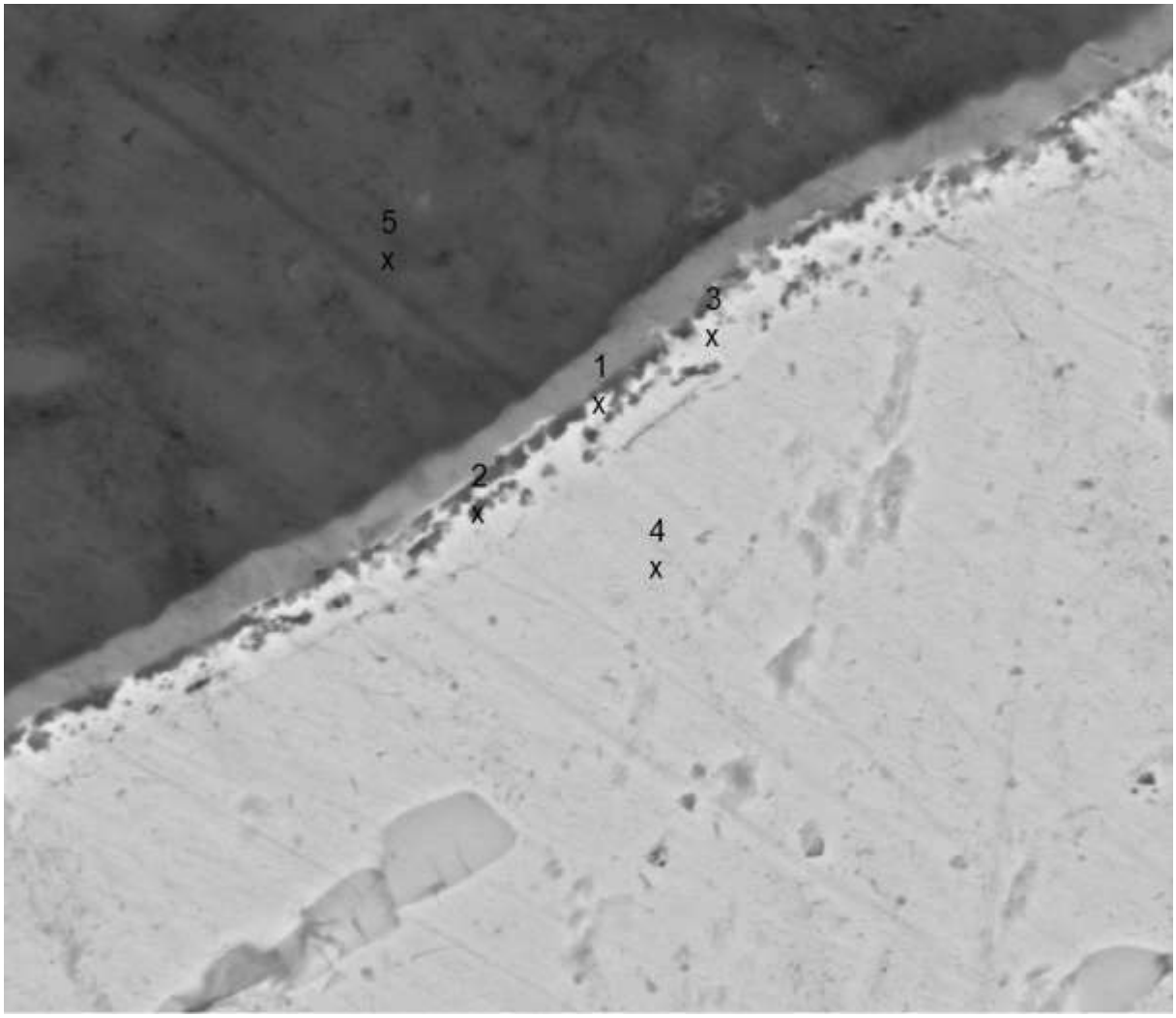

Figure 12 Miniplate co-rolled at 650ºC and compressive stress between 4372 and 29152 MPa. In the SEM image the regions where and EDAX analysis was made are indicated. The results are shown in *figure 13*.

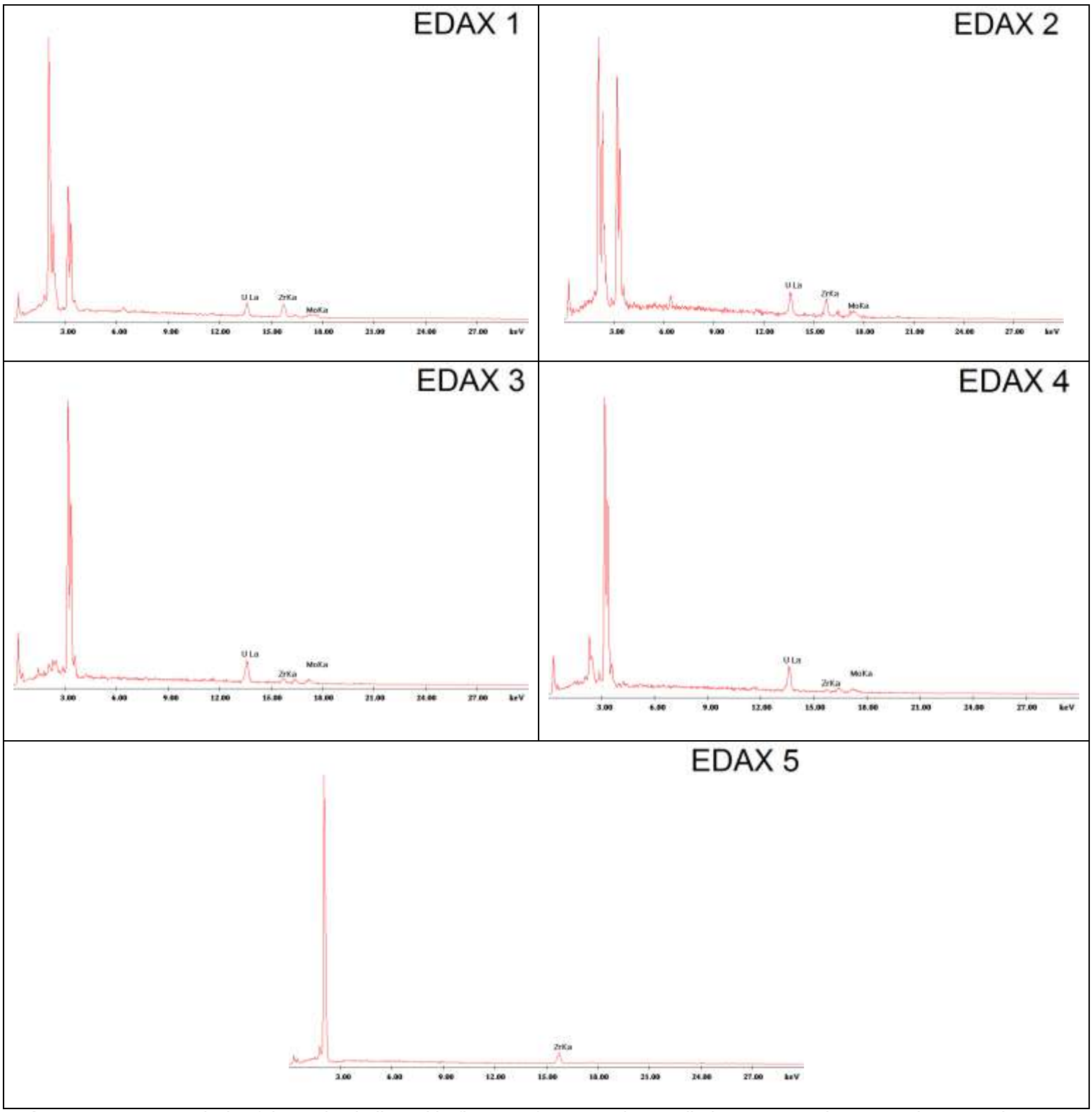

Figure 13: EDAX analysis of the region indicated in *figure 12* for a sample co-rolled at 650ºC and compressive stress between 4372 and 29152 MPa.

Discussion and Conclusions

An increase in the temperature treatment clearly helps the interdiffusion to occur. At the highest temperature, regions rich in Molybdenum are more likely to appear. As well as this, temperature has a strong influence on the interlayer: the higher the temperature is, the thicker the interlayer becomes. The exposure time also benefits the inter-diffusion (see *figure 2*).

Another relevant parameter is the compressive stress; the presence of this force is essential to define the interlayer. In addition to temperature, the compressive stress benefits significantly the accumulation of Molybdenum in the interlayer.

References

[1] CNEA Developments in U-Mo-Zry-4 Miniplates and Plates Fabrication Process, M. López, B. Picchetti, A. Gonzalez, H. Taboada – RRFM 2013 – Saint Petersburg - Russia

[2] Zircaloy cladding mechanical properties, K. Hannerz, G. Vesterlund – Nuclear Engineer and Design, Volume 33, Issue 2, September 1975, Pages 205–218

[3] ASM Alloy Phase Diagrams Center (1963 Ivanov O.S.)

[4] Metastable phases in the uranium molybdenum system and their origin - K. Tangri†, G.I. Williams, Journal of Nuclear Materials Volume 4, Issue 2, July 1961, Pages 226–233

[5] M. Griffiths, Philosophical Magazine A 63 nº 5 (1991) 835-847

INSTALLATION OF A NEUTRON RADIOGRAPHY FACILITY AT THE EDUCATIONAL REACTOR, AGN-201K

MYUNG HYUN KIM*, JONG-MIN CHOI
Department of Nuclear Engineering, Kyung Hee University
1732 Deogyeong-daero, Giheung-gu,Yongin-si, Gyeonggi-do, 446-701, Korea

ABSTRACT

The AGN-201K reactor has been used for students training after refurbishment at 2007. The second refurbishment was done from 2010 to 2011 with enhancement in accuracy and reliability of both safety systems and detector systems. Additionally a small neutron radiography facility(NRF) was designed and installed at the thermal column area. The flux level at this area with graphite is about 1.0×108#/㎠-sec. With a collimator in the center of graphite thermal column, we may have a high quality neutron beams even though target hole size is limited. A preliminary study was done with MCNP simulation with various collimator design options.

The minimum thermal neutron flux of object needed in neutron radiography is known to be about 1.0×105#/㎠-sec. Based on the relation with neutron flux and L/D ratio, the thermal neutron flux was calculated as about 1.0×108#/㎠-sec at the entrance of collimator. Collimator ratio of AGN-201K reactor was limited by column size and low flux level. In order to prevent interference of thermal neutron from graphite around the beam tube, B4C lining layer was designed with a thickness of 5cm. A sapphire lens was installed as a fast neutron filter. Upper surface of thermal column was covered with a neutron shielding layer made of B4C in order to protect image plate from backscattering neutrons and gammas.

Performance evaluation of collimator was done with three parameters; neutron beam uniformity (NBU), thermal neutron content (TNC) and neutron beam linearity (NBL). Neutron beam uniformity of NRF should be less than 10%. Both TNC and NBL are aimed to be high without limit. Calculated NBU was 10%, NBL was 78% and TNC was 38.8%.

The digital image radiography was done using the neutron sensitive Image Plate (IP-ND). These image plates were read by the FLA-7000 IP image scanner. The image plate was mounted on the image cassette as a darkroom. The sample wasd placed between collimator exit and the image cassette, irradiated during reactor operation. By changing the thickness and properties of the sample, operation time (irradiation time) and power (intensity), many trial shots were done for the search of optimal condition for each image. Quality of image was not good enough for non-destructive test. However, we could differentiate clearly inner parts of many metallic devices.

1. Introduction

Neutron radiography facilities(NRF) are being widely used in research reactors in more than twenty countries. In Korea, it was installed at HANARO reactor built in Korea Atomic Energy Research Institute for both academic research and industrial services.[1] NRF is composed of neutron source, collimator and image system. As a thermal neutron source, nuclear reactors are used because of reliable supply of high flux neutrons. Collimator is the key element of NRF, and high quality neutron beam can be obtained from the adjusted collimator design. Most common collimator design type is a divergence type and it is installed at the beam port line in a horizontal direction layout. Collimators are consist of beam filter, liner, collimator divergence angle and filling gas. Size and material choice is different for each reactor in order to adapt to the operational condition. It is known that collimator ratio (L/D)

defined as a ratio of beam line length to an entrance diameter is closely related with quality of radiographic image. The minimum requirement of L/D is known to be 50.[2],[3] In case of NRF in the National Institute of Standards and Technology(NIST), maximum power is 22 MW_{th} and L/D ratio is 560. Thermal neutron flux at collimator outlet is 1.8E+07 #/cm^2-sec.[4] In case of HANARO reactor, maximum power is 30MW_{th} and L/D ratio is 260. Thermal neutron flux at collimator outlet is 1.0E+07 #/cm^2-sec .
Neutron flux level of AGN-201K at Kyung Hee University is far less than fluxes at most of research reactors.[4] Thermal flux level at the core center is 4.5E+8#/cm^2-sec. Furthermore, collimator and imaging system should be lined to the coaxial direction at the top of the core. Available space above the core at this stage is limited and L/D ratio of collimator for AGN-201K reactor cannot be more than 50 at this research. Simulation and design were done for these constraints at AGN-201K.
There are three method in imaging systems; film method, CCD camera method and image scanner method. NRF at HANARO reactor is utilizing a CCD camera method along with film method, also tomography has been installed for 3-D images by using CCD camera.[5] In the AGN-201K reactor, both CCD camera method and film method are not appropriate because they need a strong beam flux. Radiographic image from image plate can be adjusted by computer system when we use image scanner where picture can be obtained under low-flux level shot. However, image plates cannot provide image scanner system with high quality high resolution image.
In this paper, collimator design study with MCNP code is explained with results of experimental images. A parametric study for a design optimization was done with parameters such as thermal neutron flux level, thermal neutron content(TNC), neutron beam linearity(NBL), neutron beam uniformity(NBU).

2. Neutron Radiography for AGN-201K

2.1 AGN-201K

The core material of AGN-201K reactor is a homogeneous mixture of polyethylene and uranium dioxide; the uranium is 19.5±0.5% enriched in Uranium 235. Control is affected by the insertion and withdrawal of rods containing essentially the same material as the core. Three rods are the same size; two of these serve as safety rods, and the third is a coarse control rod. The fourth rod, which is smaller, provides fine control. Also, AGN-201K reactor is very safe reactor because of the limited excess reactivity and the strong negative temperature feedback coefficient. The reactor core tank is sealed with the aluminum of 2mm thickness to keep the fission gas and its diameter is 32.2cm, height is 76cm. There is the Glory hole inside the reactor core tank with the horizontal direction and reactor core is surrounded by the reflector of the high-density graphite with 20cm thickness. The gamma shield surrounding the reflector is the lead of 10cm thickness. The reactor tank is comprised of core tank, reflector, lead shielding, control rod, Glory-Hole, Access Ports; diameter of the reactor tank is 86cm, height is 148cm. There is the movable thermal column on the top of the reactor tank and reactor tank is surrounded by the light waters (about 1,000 gallon) of 55cm thickness except bottom part.[6]
Available space for a collimator which is the key elements of NRF are Glory-Hole and Access Port. Diameter of Glory-Hole and Access Port are 1 inch and 4 inch respectively, those are used for neutron activation analysis(NAA) experiments. The other space can be obtained when a large thermal column at the above of core is removed. Figure 1 shows AGN-201K reactor modeled for MCNP simulation. A thermal column is placed at the middle-top of AGN-201K reactor and filled with high density graphite. The flux level at this area with graphite is about 1.0×E+8 #/cm^2-sec. With a collimator in the center of graphite thermal column, we may have a high quality neutron beams. A preliminary study was done and showed very flat beam intensities along the exit line of collimator. [7]

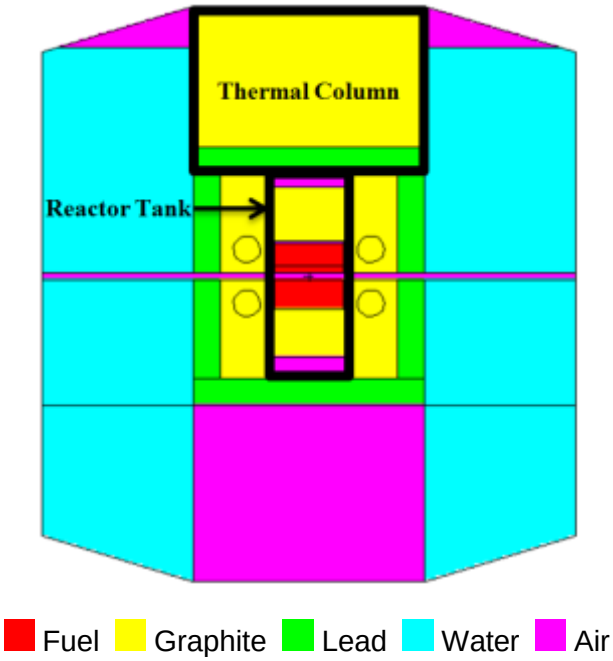

Fig. 1. AGN-201K Model for MCNP

2.2. The Design Constraints of NRF

The collimator nose of NRF is generally installed at the edge of reactor containment because NRF uses thermal neutron. However, thermal neutron flux of AGN-201K reactor core is very low, about 4.5E+8 #/cm^2-sec at the core center. Therefore, collimator nose should be located as close as possible to the reactor core and it is possible at this reactor. However, cadmium ratio at the core periphery is significantly low, about 3. For this reason, shield of fast-neutron should be considered when collimator was designed. In the PULSTAR reactor of North Carolina State University(NCSU), 6 inch thick sapphire filter was used for filtering of fast neutrons to enhance thermal neutron content(TNC).[8] Aperture is one of the main components of collimator, it absorbs neutron except passed neutron into collimator. Liner absorbs the scattered neutron beam among the neutron beam come into the collimator. For this reason, aperture and liner use the strong neutron absorbing material; Gd, Cd, B4C and etc. However, if the volume of this strong neutron absorption material is increased, AGN-201K cannot be attained to the criticality because of very low excess reactivity.

3. MCNP Simulation for the Design of Collimator

3.1 Modeling and Simulation with MCNP

For the design of collimator, K-code option was used in order to simulate a realistic neutron travelling to the target from the core. AGN-201K reactor is small and very sensitive to the surrounding environment. Furthermore, the AGN-201K reactor can operate at the narrow operational temperature band, 16°C ~ 25°C because of the small excess reactivity and strong negative temperature feedback effect. Temperature of all materials was assumed to 20°C considering the nominal operational condition.

Calculation and simulation were done with MCNP code with geometry splitting method for a variance reduction technique. [9]

3.2 Evaluation of Thermal Neutron Beam Performance

Collimator was designed and installed virtually in the AGN-201K reactor and the performance of the neutron beam in the collimator outlet was evaluated by computer simulation. Thermal neutron flux(TNF), thermal neutron content (TNC), neutron beam linearity (NBL) and neutron beam uniformity (NBU) at the collimator outlet were evaluated. Minimum thermal neutron flux at the collimator outlet is required more than 1.0E+06 #/cm^2-sec. However, in the case of the

AGN-201K collimator, flux level is not high enough. In order to have the equivalent neutron fluence(#/cm^2), beam time should be increased. Most of collimator at the high flux reactor has a beam shutter to reduce a beam time. However, AGN-201K should be designed to take a picture during more than an hour. In case of PULSTAR nuclear reactor at the North Carolina State University (NCSU), radiographic image was made for 10 seconds in the thermal neutron flux of 1.6E+06. Based on this data, the beam time of the AGN-201K reactor for picture should be calculated. [8]

TNC indicates the ratio which the thermal neutron occupies in the neutron beam. Because NRF uses the thermal neutron, TNC and Cd ratio are important index for neutron beam performance. In the case of PULSTAR, TNC is 99%. The Cd Ratio of the ETRR-2 reactor is 10. Most of NRFs did not use the neutron beam linearity (NBL) as the index of the neutron beam performance. However, NBL surely has to be evaluated because L/D Ratio of the AGN-201K nuclear reactor must be small. The neutron beam uniformity (NBU) can confirm the neutron flux distribution at the object. The uniform neutron beam can obtain the effectually contrasted image. NBU is calculated as the error of the neutron flux at the collimator outlet. NBU of HANARO reactor is 7%, ETRR-2 is 4.5%. [10]

For an evaluation of NBL, one small SURFACE was modeled in the collimator outlet. The ratio of the neutron passing through with the normal direction was calculated at this SURFACE.

For an evaluation of NBU, one CELL is modeled as 45cm by 45cm and 0.1cm thickness at the collimator outlet. This CELL is divided into 45x45 meshes by using the Mesh Tally in order to evaluate uniform flux distribution.

TNC is the ratio which the thermal neutron occupies in the neutron beam. The maximum energy limit of thermal neutron in NRF is 0.1eV ~100keV. In this calculation, the energy of the thermal neutron was assumed less than 1eV. Also, the thickness of the sapphire filter as shielding of fast neutron was determined with simulation study for the best thermal neutron flux and TNC.

4. Collimator Design for AGN-201K

4.1 Parametric Study

For the estimation of the best collimator, a new parameter of neutron beam linearity(NBL) was defined for this study. NBL is the ratio of neutrons passing the final cone of angle 5° at the exit. For the short collimator in AGN-201K, it is very easy parameters to estimate the collimation effect. The large value of NBL is representing the high quality of beam straightness. Table 1 shows the results of thermal neutron flux(TNF) and NBL at the collimator outlet for the various thickness of collimator liner. As the thickness becomes larger, the flux in the collimator outlet is decreased slightly but NBL is increased larger. Liner is purposed to increase the NBL by absorbing the scattered neutron beam among the neutron beam come into the collimator.[11] However, liner of AGN-201K collimator gave additional effect, thermal neutrons generated from outside graphite are blocked. Therefore, NBL can be increased as the increase of liner thickness. However, the thick liner which is a strong neutron absorber gave a parasitic effect in criticality. The liner thickness was determined as 5cm considering the TNF, NBL and reactor criticality.

Thickness of Liner	Thermal Neutron Flux (#/cm^2-sec)	Neutron Beam Linearity (NBL)
1cm	8.16E+03	78.03%
2cm	8.09E+03	84.32%
4cm	7.82E+03	85.47%
5cm	7.13E+03	86.84%

Tab 1: The variation of TNF and NBL with thickness change of Liner

Because of spatial limitation above the core, collimator length was chosen to be 50cm. By changing the diameter of entrance, the collimator ratio (L/D) was tested. Table 2 shows the sensitivity of TNF and NBU to the L/D change. Low value of NBU represents low deviation of thermal flux levels at each pixel. Therefore the lowest NBU means that flux level is perfectly uniform. As collimator ratio decreased, diameter of entrance is increased for the fixed length and TNF is increased but NBU is increased to the low quality profile. By choosing smaller collimator entrance, NBU became small for the flat neutron flux distribution, but reactor operation time should be increased because of low neutron flux. The diameter of entrance was designed as 4cm and collimator ratio (L/D) was chosen to be 12.5 considering the operating reactor time and level of TNF.

Collimator Ratio(L/D)	Thermal Neutron Flux (#/cm^2-s)	Neutron Beam Uniformity (NBU)
50	1.65E+03	2.5%
25	7.71E+03	5.4%
17.7	1.90E+04	8.2%
12.5	3.29E+04	9.6%

Tab 2: Sensitivity of TNF and NBU to the L/D ratio

Table 3 shows the sensitivity of TNF and NBL to the shape of collimator, the collimator divergence angle. The smaller angle decreased, the better in linearity, i.e. the higher NBL. The sensitivity of TNF is small to the angle. Concerning the beam exit area, collimator divergence angle was designed as 5°.

Divergence Angle	Thermal Neutron Flux (#/cm^2-s)	Neutron Beam Linearity (NBL)
3°	8.06E+03	75.04%
5°	7.98E+03	69.40%
7°	7.71E+03	66.78%

Tab 3: Sensitivity of TNF and NBL to the Collimator Divergence Angle

4.2 AGN-201K Collimator Design

Figure 2 shows two collimator model which is finally decided. The dimensions of two collimators are same, but collimator (B) is 30cm above the collimator (A).

Collimator-A Collimator-B

① Graphite ② Lead ③ Sapphire Filter ④ Aperture
⑤ Liner ⑥ Filling Gas ⑦ Neutron shielding material

Fig. 2. Collimator Design for AGN-201K

The sapphire filter, 4cm in diameter and 10cm thickness, is located at the collimator entrance to shield fast neutrons. The collimator diameter of entrance is 4cm and the outlet diameter is 8cm. The collimator length is 50cm and L/D Ratio is 12.5 and collimator divergence angle is 5°. In particular, to prevent interference of thermal neutron from graphite around the beam tube, B_4C lining layer was designed with a thickness of 5cm and the Filling Gas designed with an air. Upper surface of thermal column was covered with a neutron shielding layer made of B_4C in order to protect image plate from backscattering neutrons and gammas. Also, two collimator models do not perturb much in reactor criticality; with collimator-A k-effective becomes 1.00082 and with collimator-B 1.00147.
Table 4 shows the performance of AGN-201K collimator. NBU of NRF should be less than 10%. Both TNC and NBL should be as high as possible. Each thermal neutron flux at the collimator outlet were evaluated by 3.10E+04 #/cm^2-s, 8.53E+03 #/cm^2-s. The collimator-A model has to operate reactor for 2 hours and the collimator-B model has to operate reactor for 8 hours in order to satisfy the Thermal Neutron Flux at the collimator outlet. NBUs of the two collimators model are same with 10%.

	Collimator-A	Collimator-B
Thermal Neutron Flux (#/cm^2-s)	3.10E+04	8.53E+03
Thermal Neutron Content (TNC)	38.8%	74.5%
Neutron Beam Uniformity (NBU)	10%	10%
Neutron Beam Linearity (NBL)	79%	83%

Tab 4: Comparison of Neutron Beam Performance of Two Collimator Design

4.3 Design Modification Study

The MCNP simulation was performed in order to obtain the radiographic image of the high quality by changing the collimator design. Finally, the chosen collimator ratio (L/D) is significantly low as 12.5 because of the low flux. Performance of neutron beam was evaluated for higher L/D ratio of 50. Also, the divergence type collimator was changed to the parallel type collimator. Parallel type collimator was simulated in order to enhance the NBL because collimator length cannot be longer. [11]
In the collimator-A model, the diameter of collimator entrance was reduced to 1cm and the neutron beam performance was evaluated as L/D ratio of 50. The NBL is increased slightly, TNF is decreased by 3 times. There is no high benefits from this modification.
The type of collimator shape was changed from divergent cone type to the parallel hole type. For this design, entrance diameter and collimator length are 4cm and 50cm, resulting in small collimator ratio of 12.5. With this collimator, NBL is increased from 79% to 93%, but there is no significant change in TNF and TNC.

5. Test Experiments in a AGN-201K NRF

Experimental shots were taken with many experimental conditions, reactor operation time (irradiation time) and reactor power (beam intensity). With neutron sensitive image plates, image was easily made with computer programs. The following figures are results of test shots with exposure time of 2 hours under power level of 4 watt through collimator-A.

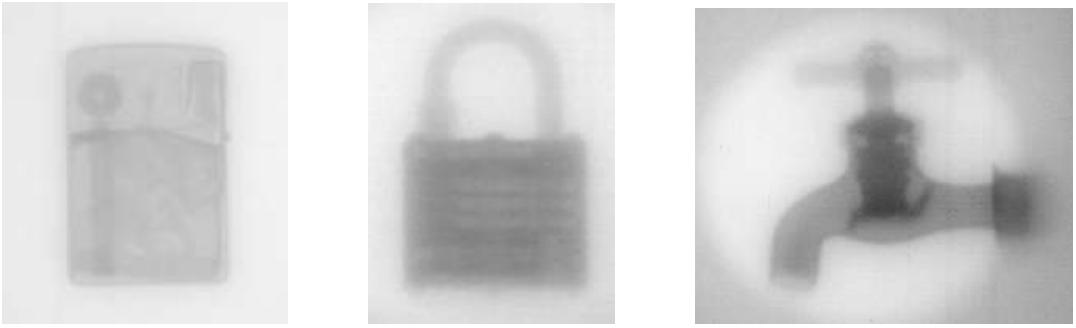

(A) Lighter (B) Lock Pad (C) Faucet

Fig. 3. Neutron Radiography Image at AGN-201K

NRF was designed and installed in AGN-201K research reactor which has been used only for educational purpose. Some radiographic images of metallic object were successfully obtained. Although most of NRF were installed only at high-power research reactors having reasonably high neutron fluxes, the feasibility of NRF installation in AGN-201K was shown in this paper. The resolution of image is highly dependent on experience as well as collimator design. More intensive test experiments should be followed during the research for the better image under the highly limited condition of AGN-201K.

REFERENCES

[1] P. Von Der Hardt and H. Rottger, Neutron Radiography Handbook, D. Reidel Publishing Company, Dordrecht, Holland, pp.2-20, 1979.

[2] J.C. Domanus, Collimator For Thermal Neutron Radiography An Overview, Riso National Laboratory, Roskilde, Denmark, pp.15-51, 1990.

[3] J. C. Domanus, Practical Neutron Radiography, Riso National Laboratory, Roskilde, Denmark, pp.96-127, 1990.

[4] Myung Hyun Kim, "Utilization of AGN-201K for Education and Research in Korea," Research Reactor Fuel Management (RRFM)-2011, Rome, Italy, March 20-24, 2011.

[5] Development of the Neutron Radiography Facility and its Installation in HANARO, KAERI/TR-1981, Daejeon, Korea, 2001.

[6] Aerojet General Nucleonics, “Educational Experiments Utilizing The AGN-201 Nuclear Reactor," AGN REPORT No.16, AGN, January, 1957.

[7] J. Choi and M.H.Kim, "Neutron Beam Evaluation for NRF in AGN-201K Reactor Using MCNP Simulation," Transactions of the KNS Spring Meeting, Korea, May 27-28, 2010.

[8] Kaushal Kishor Mishra, “Development of a Thermal Neutron Imaging Facility at the N.C. State University PULSTAR reactor”, NCSU report, 2005.

[9] J.S. Hendricks, et. al. "MCNPX user's manual, Version 2.6.0", Los Alamos National Laboratory, April 2008.

[10] M. A. Abou Mandour “Characterization and Application of the Thermal Neutron Radiography Beam in the Egyptian Second Experimental and Training Research Reactor (ETRR-2)” Hindawi Publishing Corporation Science and Technology of Nuclear Installations Volume 2007, Article ID 24180

[11] Mac Gillivray G.M., “Neutron Radiography Collimator Design”, Nray Service Inc. RR#1 Petawawa, Ontario, Canada.

ARSENIC DETERMINATION IN COAL AND ASH SAMPLES BY NEUTRON ACTIVATION ANALYSIS

A.N. ESEN
Istanbul Bilgi University, Faculty of Engineering,
TR-34060, Eyup, Istanbul, Turkey

E. ORUCOGLU
Istanbul Technical University, Faculty of Mines,
TR-34469, Maslak, Istanbul, Turkey

S. HACIYAKUPOGLU, S. ERENTURK
Istanbul Technical University, Energy Institute,
TR-34469, Maslak, Istanbul, Turkey

ABSTRACT

Arsenic is one of the trace elements in coal that have toxic effects which can cause environmental pollution and human health problems. Therefore it is of great importance to determine arsenic accurately and precisely. Production, processing and combustion of fossil fuels can lead to arsenic dispersion through environment; additionally in thermal power plants, the ashes spread on dumping areas. Arsenic enriched in ashes during combustion and arsenic accumulation can increase in aquatic systems due to the leakage from ashes by rainfall. Since the solubility, mobility and toxicity of arsenic depend on its oxidation state, studies of arsenic speciation are essential to understand the characteristics of arsenic species in the environment. Many of these species are results of natural processes, such as mineral weathering or biological activity, yet the number of possible anthropogenic sources is increasing, primarily from mining and agriculture. Neutron activation analysis method is an important and useful tool for arsenic determination in environmental samples such as coal.

Coal cleaning is a process by which impurities such as sulphur, ash, and rock are removed from coal to upgrade its value. The majority of coal cleaning processes uses upward currents or pulses of a fluid such as water to fluidize a bed of crushed coal and impurities. The lighter coal particles rise and are removed from the top of the bed. The heavier impurities are removed from the bottom. This study aimed to determine the arsenic leakage from coals and ashes exposed to a coal cleaning process. Coal and coal ash samples taken from local areas in the south eastern site of Turkey were grounded and exposed to water for one month period. Then the samples were cleaned in a wet process and dried. The concentration of ^{76}As in samples before and after the cleaning procedure was determined by instrumental neutron activation analysis. For this reason pure and water cleaned coal samples were irradiated in central irradiation tube of TRIGA MARK II Research Reactor of Istanbul Technical University and measured for their activities by using high resolution gamma spectroscopy system and GAMMA-VISION-32 software. The result of study has shown that the applied cleaning process cause to a slight decrease in arsenic content in pure coal and coal ash samples.

1. Introduction

Arsenic contamination of the environment has occurred in many parts of the world and is considered as a global issue. Industrial activities release large quantities of arsenic into the environment, which can be dispersed widely and plays an important role in the global contamination of soils, waters, and air that effect human health [1]. Coal and its combustion by products (fly and bottom ashes) may contain arsenic, therefore power plants that burn arsenic rich coals and disposal sites for wastes from these plants are one of the principal sources of arsenic contamination. There are many studies investigating arsenic concentration in coal and coal combustion products in the literature [2-4].

The world average arsenic content is 9.0 and 7.4 ppm for the bituminous coals and lignites, respectively. These contents are higher in ash samples: 50 ppm and 49 ppm, respectively [5]. Physical coal cleaning procedures should be successful in removing substantial proportions of this element [6]. Arsenic content of many coals can be effectively reduced by conventional physical coal cleaning procedures up to 70% [7,8]. Coal cleaning process is often required to remove excessive impurities in order to increase the heat content and to reduce potential air pollutants for efficient and environmentally safe utilization of coal [9]. Physical coal cleaning techniques based on density separation are widely used. Coal particles are added to a liquid medium and then subjected to gravity or centrifugal sources to separate the impurities. When lighter coal particles rise and removed from the top, the heavier impurities are removed from bottom. Coal cleaned in the wet processes then dried for the following coal preparation processes.

The purpose of this study is to investigate the arsenic leakage from coal and ash samples. For this reason samples taken from local areas in the south eastern region of Turkey were exposed to cleaning process in laboratory conditions. The concentration of ^{76}As in samples before and after the cleaning procedure was determined by instrumental neutron activation analysis. Samples were irradiated in ITU TRIGA MARK II Research Reactor of Istanbul Technical University and measured by high resolution gamma spectroscopy system.

2. Material Method

2.1Sample collection and cleaning experiments

A total of 12 coal samples were collected from a main coal mine located in south east of Turkey. The 2 bottom ash samples and 1 fly ash sample were obtained from a coal-fired power plant in this region.

Raw coal samples were crushed and grinded with a mill. Then bidistilled water was added to coal and ash samples providing the solid/liquid ratio 2%. After one month waiting time, all prepared suspensions were filtered and air dried.

2.2 Dry mass determination

Dry mass determination was done on separate samples and not on those taken for As analysis, because deviation from proposed drying methods was observed to lead to differences of up to 5% in dry mass correction factors and the heterogeneity of sample moisture as well as hygroscopic behaviour during weighing play an important role in the uncertainty estimation [10]. A gravimetric method was applied for the determination of the dry matter content of the samples [11]. Samples were dried to constant mass in an oven and the difference in mass prior to and after drying process was used to determine the dry matter content. At first, mass of the each empty sample container was determined. Then suitable amount of each moist sample was weighed into a container. The containers includes moist samples were placed in the drying oven and dried to constant mass at 105°C for 24 hours. Then, containers were removed from the oven and put in the desiccator to reduce absorption of moisture from the atmosphere during cooling to room temperature. After cooling in the desiccator, container includes oven-dried sample was weighed. Dry matter content, f_{dm}, of each sample was expressed as a percentage of mass using the equation (1)

$$f_{dm} = \frac{m_{ds} - m_c}{m_{ws} - m_c} x100 \qquad (1)$$

where m_c is the mass of the empty container, m_{ds} is the total mass of the container and dried sample and m_{ws} is the total mass of the container and moist sample.

2.3 Preparation and irradiation of samples

Standard Reference Material NIST 1633b, coal fly ash, was used as comparator standard based on its matrix and known quantity [12]. Furthermore, Standard Reference Material NIST 2702, inorganics in marine sediment, was used to check the accuracy of the method [13]. Samples and standard reference materials were packed in aluminium foils filled with approximately 250 mg. Thermal neutron flux of the reactor was measured by using Au monitors. The Au monitors were prepared using a stock solution prepared from $AuCl_4H{\cdot}3H_20$ compound (99.5 % purity, Merck). 30 µL aliquots were deposited on to chromatographic paper disks from this stock solution with a gravimetrically calibrated micropipette. After evaporation, these disks were covered with polyethylene bags and sealed. The irradiation was performed in central irradiation tube of ITU TRIGA MARK II Research Reactor at 250 kW. A total of 30 samples (3 Au monitors, 22 coal samples, 4 fly ash samples, 2 bottom ash samples and 2 reference materials) were stacked together and fixed in the irradiation tube in sandwich form and irradiated for 6 h (Figure 1).

Fig 1: Position of samples in the irradiation tube

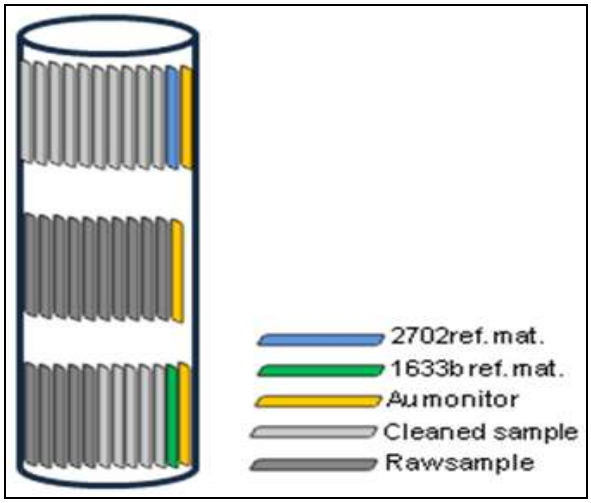

2.4 Gamma spectroscopy

The determination of arsenic and gold was based on its activation by thermal neutron capture. Their activation products, ^{76}As and ^{198}Au, decay with half-life of 26.32 h (a gamma-ray at 559.101 keV with an intensity of 45%) and 2.695 d (a gamma-ray at 411.804 keV with an intensity of 96%), respectively [14].

Gamma-ray spectra of samples, monitors and reference materials were measured by using HPGe detector (ORTEC GMX n-type) with a relative efficiency of 14.4 % and a resolution of 2.0 keV at 1332.5 keV photons of ^{60}Co. The detector was connected to a digital signal processing analyser (ORTEC DSPEC jr. 2.0) operating through Gamma Vision-32 spectroscopy software. Decay time for samples and reference materials were approximately 4 days and 6 days, respectively. Counting times of either 300 s or 600 s were used to obtain good statistics of the spectrum counts depending on the activities of samples. Measurements were performed at such distance that the dead times were in the range of 4.87-15.58%. Arsenic amount of samples were calculated from comparison of net peak areas at 559.101 keV in the measured spectra of sample and comparator standard using the equation (2)

$$m_s = m_c \cdot \frac{\left(\frac{C}{t_m \cdot e^{-\lambda t_d} \cdot (1 - e^{-\lambda t_m})}\right)_s}{\left(\frac{C}{t_m \cdot e^{-\lambda t_d} \cdot (1 - e^{-\lambda t_m})}\right)_c} \quad (2)$$

in which m is the mass of the interested element in g, C is the net counts in the interested γ-ray peak, t_m is the duration of the measurement in s, t_d is the decay time to start of count in s, λ is the decay constant in s^{-1}; where s and c denotes sample and comparator, respectively. The accuracy of the results was statistically evaluated using z-score test for comparison between experimental result and certified value of reference materials. The deviation from certified value was evaluated using z-score test according to the equation (3)

$$z = \frac{\left|x_{exp} - x_{cer}\right|}{\sqrt{u_{exp}^2 + u_{cer}^2}} \quad (3)$$

where x_{exp} and x_{cer} are the experimental and certified value; u_{exp} and u_{cer} are the experimental and certified uncertainty, respectively. The result is accepted if $z \leq 2$, questionable if $2<z<3$ and not accepted if $z \geq 3$ [15].

3. Results and Discussion

Results obtained according to correction of the gamma spectrometric measurements for dry mass, decay and measurement times were given in Table 1. Arsenic concentrations are found to be 4-149 mg/kg in raw samples and 3-126 mg/kg in cleaned samples that indicate arsenic concentration is higher than the world average value for raw coal and ash samples.

Raw samples			Cleaned samples		
Sample ID	**Dry mass factor**	**As concentration (mg/kg, ±1σ)**	**Sample ID**	**Dry mass factor**	**As Concentration (mg/kg,±1σ)**
RC-1	0.89	30.00±0.66	CC-1	0.91	27.36±0.58
RC-2	0.95	4.31±0.27	CC-2	0.97	3.64±0.24
RC-3	0.88	58.46±1.62	CC-3	0.89	26.73±0.58
RC-4	0.90	71.31±1.79	CC-4	0.94	60.81±2.08
RC-5	0.88	39.93±1.33	CC-5	0.96	31.95±1.15
RC-6	0.95	11.57±0.77	CC-6	0.92	9.13±0.32
RC-7	0.91	73.64±1.86	CC-7	0.90	66.53±1.75
RC-8	0.88	45.59±1.45	CC-8	0.90	20.65±0.50
RC-9	0.88	41.91±1.31	CC-9	0.92	16.67±0.45
RC-10	0,90	63.64±1.64	CC-10	0.92	31.78±0.66
RC-11	0.91	111.11±2.28	CC-11	0.93	98.07±2.11
RC-12	0.90	149.11±3.21	CC-12	0.99	126.00±2.43
RBA-1	0.91	59.13±1.99	CBA-1	1.00	49.22±1.91
RBA-2	0.97	49.37±1.41	CBA-2	0.98	40.67±1.32
RFA-1	0.91	127.85±2.59	CFA-1	0.94	118.44±2.35

Tab 1: Results of raw (RC) and cleaned coal (CC), raw fly (RFA) and bottom (RBA) ash samples

The comparator method was validated by certified reference materials and good agreement was found between experimental results and certified values. As can be seen in Table 2, no statistically significant discrepancy is detected by this test, as in two cases |z| <2.

Reference material	Experimental result (mg/kg, ±2σ)	Certified value (mg/kg, ±2σ)	z-score
NIST 1633b	131.2±8.5	136.2±2.6	1.17
NIST SRM 2702	47.4±2.6	45.3±1.8	1.33

Tab 2: z-score values for comparison between experimental result and certified value

Our study indicates that concentration of arsenic is reduced in all samples as a result of cleaning process. The degree of reduction varies between samples in the range of 7-60% as shown in Figure 2. On average, arsenic concentration is reduced 25% compared to raw samples. It can be seen that cleaning process is more efficient for coal samples compared to ash samples that can be explained with their different chemical properties. The average cleaning efficiency value for coal samples is 28% and ash samples 13%.

Fig 2: Cleaning efficiency of samples

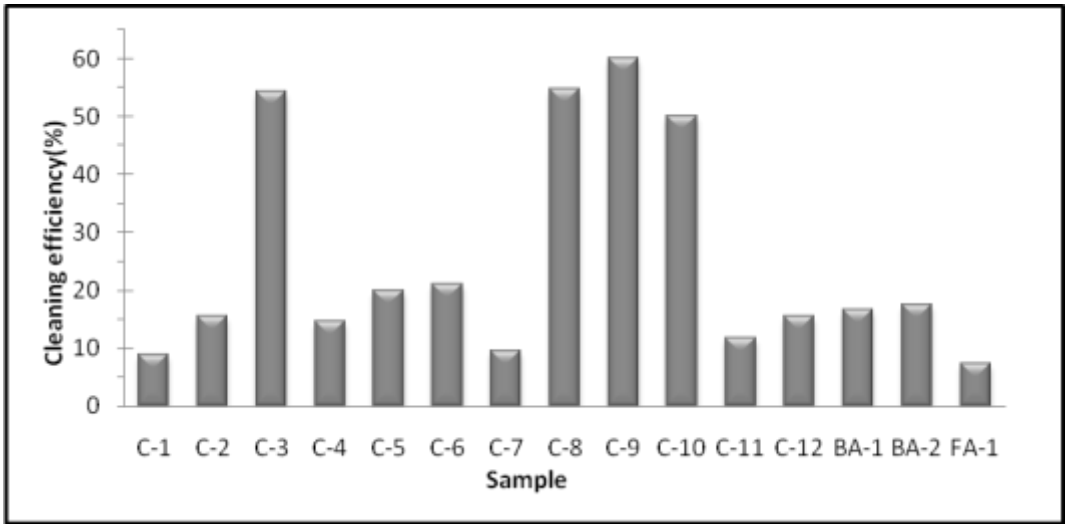

Related researches for different coal types and experimental conditions are also in progress; as conclude it can be said that:

- Suitable INAA method was adopted to determine arsenic amount in coal and ash samples.
- Arsenic amounts are varying in different coal and ash samples.
- Arsenic determination with comparator method was validated by certified reference materials.
- By applying some precautions to coals and ashes, arsenic amounts can be reduced.

Acknowledgements

Authors are grateful to ITU TRIGA MARK II reactor staff for their support during irradiations.

4. References

1. Pacyna, J.M., Pacyna, E., 2002, “An assessment of global and regional emissions of trace metals to the atmosphere from anthropogenic sources worldwide”, Environmental Review, 9, pp. 269–298.
2. Goodarzi, F., 2006, “Assessment of elemental content of milled coal, combustion residues, and stack emitted materials: Possible environmental effects for a Canadian pulverized coal-fired power plant”, International Journal of Coal Geology, 65, pp.17-25.
3. Eskenazy, G.M., 2009, “Trace elements geochemistry of the Dobrudza coal basin, Bulgaria”, International Journal of Coal Geology, 78, pp. 192-200.
4. Diehl, S.F., Goldhaber, M.B., Koenig, A.E., Lowers, L.F., Ruppert, L.F., 2012, “Distribution of arsenic, selenium, and other trace elements in high pyrite Appalachian coals: Evidence for multiple episodes of pyrite formation”, International Journal of Coal Geology, 94, pp. 238-249.
5. Yudovich, Y.E., Ketris, M.P., 2005, “Arsenic in coal: a review”, International Journal of Coal Geology, 61, pp.141-196.
6. Mastalerz, M., Drobniak, A, 2007, “Arsenic, cadmium, lead, and zinc in the Danville and Springfield coal members (Pennsylvanian) from Indiana”, International Journal of Coal Geology, 71, pp.37-53.
7. Finkelman, R.B., 1994, “Modes of occurrence of potentially hazardous elements in coal: levels of confidence”, Fuel Processing Technology, 39, pp. 21-34.
8. Akers, D.J., Raleigh Jr., C.E., Lebowitz, H.E., Ekechukwu, K.,Aluko, M.E., Arnold, B.J., Palmer, C.A., Kolker, A., Finkelman,R.B., 1997, “HAPs-Rxk: Precombustion Removal of Hazardous Air Pollutant Precursors” , DOE Report No. DEAI22- 97245, pp. 1-6.
9. EPA/68-D2-0159, 2005, “EMİSSİON Factor Documentation for AP-42 Section 11.10 Coal Cleaning”.
10. Zeiller, E., Benetka, E., Koller, M., Schorn, R., 2007, “Dry mass determination: what role does it play in combined measurement uncertainty? A case study using IAEA 392 and IAEA 413 algae reference materials”, Accreditation and Quality Assurance, 12, pp. 295-302.
11. ASTM, 1999, “Standard Test Method for Laboratory Determination of Water (Moisture) Content of Soil and Rock by Mass”, D 2216-98.
12. NIST, 2004, “Certificate of Analysis Standard Reference Material 1633b Constituent Elements in Coal Fly Ash”, National Institute of Standards &Technology.
13. NIST, 2012, “Certificate of Analysis Standard Reference Material 2702 Inorganics in Marine Sediment”, National Institute of Standards &Technology.
14. Firestone R.B., 1998, “Table of Isotopes [electronic resource]”, Coral M. Baglin, editor; S.Y. Frank Chu, CD-ROM editor, 8th ed., update New York, Wiley.
15. Miller, J.N., Miller, J.C., 2005, “Statistics and Chemometrics for Analytical Chemistry, 5th ed.”, Pearson Prentice Hall.

U-7MO ALLOY MICROSTRUCTURE EVOLUTION DURING IRRADIATION

B. MILLER, D. KEISER, JR., J. GAN, J. JUE, A. ROBINSON, P. MEDVEDEV, M. MEYER, AND D. WACHS

Nuclear Fuels and Materials Division, Idaho National Laboratory
P. O. Box 1625, Idaho Falls, Idaho 83403 USA

ABSTRACT

During irradiation, U-7Mo forms two distinct irradiated microstructures with the transition between the two starting to occur around a fission density of $5x10^{21}$ fiss/cm^3. At a low burnup, the U-7Mo fuel was shown to remain in a γ-(U,Mo) phase. The low burnup defect microstructure is dominated by an ordered bubble superlattice. Intergranular fission gas bubbles populate the U-Mo grain boundaries. The high burnup U-7Mo defect microstructure is dominated by randomly distributed homogenous fission gas bubbles. The bubble superlattice begins to collapse above fission densities of $5x10^{21}$ fiss/cm^3. The fuel grain sizes become sub-micron in diameter with both amorphous fuel and crystalline fuel present. Solid fission product precipitates consisting of Sr, Y, Nd, and Ba can be found inside the fission gas bubbles.

1. Introduction

The Reduced Enrichment for Research and Test Reactors program (RERTR) is developing low-enriched uranium (LEU) fuel to reduce the demand of highly-enriched uranium (HEU) fuels currently used in research and test rectors throughout the world [1]. The current fuel under development is a U-xMo fuel with x=7-12 wt%. To help qualify the U-Mo fuel, it is critical to understand changes in the fuel microstructure due to irradiation. The U-Mo fuel has two specific fuel designs [2]. These being a dispersion fuel design and a monolithic fuel design. Dispersion fuels are composed of U-7Mo fuel kernels embedded in an aluminum or aluminum-silicon alloy matrix. Coatings may be applied to the U-Mo fuel particles to improve the irradiation performance of the fuel by eliminating fuel/matrix interactions. The monolithic fuel design consists of a U-10Mo fuel foil with a Zr diffusion barrier that is embedded in the Al alloy cladding.

To fully understand fuel performance under irradiation, microstructural characterization of the unirradiated and irradiated fuel is necessary. Various microstructural studies of unirradiated and irradiated characterization of dispersion fuels have been performed [3-6]. In these analyses, the microstructures of all of the key regions in the fuel were analyzed and key observations were reported. For dispersion fuel with uncoated U-7Mo particles, general observations show that the U-7Mo fuel interacts with the surrounding matrix forming an interaction layer between the fuel and matrix. Various scanning electron microscopy (SEM) work has been performed on U-Mo fuels [5]. It was demonstrated that in irradiated dispersion fuels, the U-Mo fuel has a cellular structure due to rapid solidification during atomization. The low burnup microstructure still shows the cellular type structure during irradiation. Fission gas bubbles decorate the cell boundaries in the fuel. Additionally, molybdenum content along the cell boundaries is lower compared to the bulk of the cell boundaries. Rest et al. [7] reported seeing the same fission gas

bubble microstructure with bubbles decorating the cell boundaries of the fuel. Rest also showed that at high burnups, the fuel undergoes "recrystallization" and fission gas bubbles are uniformly distributed throughout the fuel.

Transmission electron microscopy (TEM) results show that the dispersion U-Mo remains in the γ-(U, Mo) phase up to a fission density of $3.4x10^{21}$ fiss/cm^3 [6,8] and $4.5\ x10^{21}$ fiss/cm^3 [9]. The defect microstructure was dominated by intergranular bubbles and intragranular bubbles. The intragranular bubbles form an ordered bubble superlattice in the bulk of the fuel grains. The bubble superlattice has a face centered cubic (FCC) structure coherent to the U-7Mo body centered cubic (BCC) structure with typical bubble sizes of 2-4 nm and a superlattice constant of 11-12 nm.

Recent work at the Idaho National Laboratory has utilized both scanning and transmission electron microscopy (SEM and TEM) to continue the characterization of the microstructure of irradiated dispersion fuel samples exposed to various fission densities. Common observations from the SEM and TEM analysis of the U-Mo fuel will be provided. Focus will be given to the microstructure of the irradiated U-7Mo fuel particles in dispersion fuels, and the interaction layers will be ignored. Fuel performance metrics of interest include gamma phase stability, defect characterization focusing on fission gas behavior, fuel grain sizes with increasing dose, and solid fission product behavior.

2. Experimental

The dispersion fuel plates were irradiated at the Advanced Test Reactor as part of the RERTR-6 and RERTR-7 experiments. During irradiation, the plates were oriented edge on facing the core. This led to a significant fission rate variation across the plates. This provided a variation in fission densities across individual plates. As a result, by taking samples at different locations af a fuel plate, samples could be produced that were exposed to different fission densities. Samples were produced at the Hot Fuels Examination Facility (HFEF) at the Idaho National Laboratory in the form of 1-mm diameter by 1.4 mm long fuel punchings. The sectioned samples were shipped to the Electron Microscopy Laboratory for sample preparation and analysis in the scanning electron microscope (SEM) and transmission electron microscope (TEM).

After the samples were mounted in epoxy and polished through a 1 um diamond paste finish, SEM was performed using a JEOL 7000F equipped with energy dispersive spectrometry (EDS) and wavelength dispersive spectroscopy. TEM samples were created using two different methods. A conventional jet-polish method was used and can be followed in [10]. A FEI Quanta 3D Focused Ion Beam (FIB) was used to create TEM samples and fuel cross-sections of key locations. TEM was performed using a JEOL 2010 200 keV equipped with EDS. Table 1 provides irradiation parameters of five fuel samples that have had SEM and TEM microstructure analysis performed. Plate R2R040 had two punchings analyzed from the plate and the two punchings are differentiated based on their location at the high burnup or low burnup end of the fuel plate.

Table 1: Irradiation parameters of five SEM and TEM samples

Fuel Composition	U-7Mo	U-7Mo	U-7Mo	U-7Mo	U-7Mo
Matrix	Al-2Si	Al-2Si	Al-2Si	Al-5Si	Pure Al
Fuel Plate ID	R2R010	R2R040 (Low)	R2R040 (High)	R3R050	R0R010
U^{235} % Enrichment	19%	58%	58%	58%	58%
Local Fission Density (10^{21} fiss/cm^3)	4.5	3.3	6.3	5.2	5.6
Time Average Fission Rate (10^{14} fiss/cm^3-sec)	3.8	4.3	8.1	6.6	7.2
Temperature (˚C)	109	90	120	130	125

3. Results

Figure 1 shows an optical image of a cross section produced for an irradiated fuel plate (R2R078, not listed in Table 1), a U-7Mo dispersion fuel plate with Al-2Si matrix irradiated in the RERTR-9A experiment. Included in the figure are close up images of locations in the plate exposed to fission densities above and below ~5x10^{21} fissions/cm^3. Notice the difference in the fission gas bubble microstructures at various burnups. At fission densities lower than ~5x10^{21} fiss/cm^3 (low burnup microstructure), the fission gas bubbles appear to be primarily confined to the grain boundaries of the fuel and on the outside of the fuel kernels. Above ~5x10^{21} fissions/cm^3 (high burnup microstructure), fission gas bubbles visible by optical microscopy are randomly distributed throughout the fuel kernel. Note that the 5x10^{21} fissions/cm^3 fission density appears to be a rough estimate of when the fuel is changing from the low burnup microstructure to the high burnup microstructure. As it will be shown later, low burnup microstructure features are still present above 5x10^{21} fissions/cm^3.

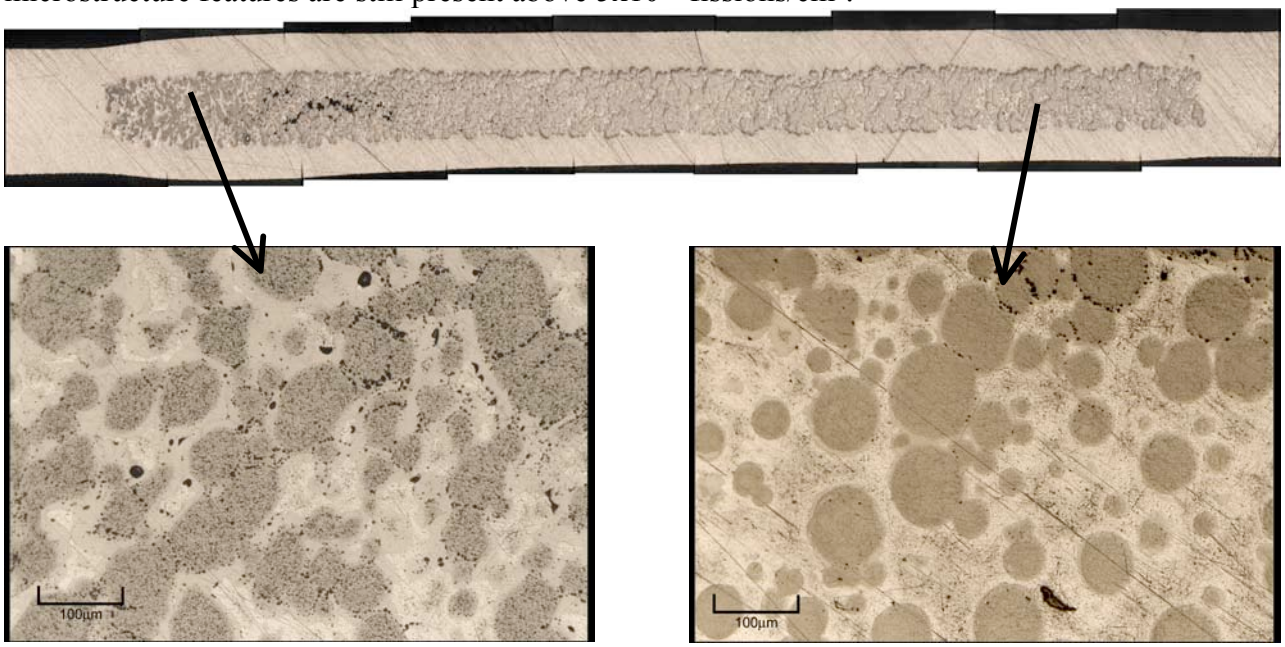

High Burnup Microstructure Low Burnup Microstructure

Figure 1: Optical microscopy images of plate R2R078 showing a full fuel cross-section and the high and low burnup microstructures in the plate. (Note the lack of spherical features for the fuel kernels in the high burnup microstructure, which may be due to the development of signficant fuel-matrix interaction).

3.1 Low Burnup Microstructure

As seen in Table 1, SEM and TEM analysis was performed on 2 individual samples with fission densities < $5.0x10^{21}$ fiss/cm^3. General observations of the sample microstructures will be provided, including stability of the U-Mo BCC structure and grain size development at various burnups. Defect analysis in SEM and TEM analysis show that fission gas bubbles form in two regions; along grain/cell boundaries and inside the bulk of the fuel grains as nano-sized bubbles. The grain/cell boundary bubbles will be referred to as intergranular bubbles and the bulk nano-sized bubbles as intragranular bubbles.

3.1.1 Stability of U-Mo

Pre-irradiation characterization of U-Mo dispersion fuel shows that typical fuel cells are under 5 μm in size in the starting powders and limited growth occurs during rolling with AA6061 cladding [3,11]. Using fracture surfaces seen in the SEM prepared samples, FIB'd cross-sections, and FIB'd TEM samples, grain/cell sizes of the fuel can be characterized. An example of a fracture surface's fuel grain microstructure from sample R2R040 is presented in Figure 2. Intergranular fission gas bubbles on the grain/cell boundaries offer a good mechanism to outline the fuel grain's shape and size (around 5 μm).

One key observation is the growth of the grain boundary/intergranular bubble regions of the fuel grain (see Fig. 2). This appears as the regions between the fuel grains where a high density of fission gas bubbles is present. With increasing burnup, this layer grows in thickness which in turn consumes more of the bulk of the fuel grains and thus decreases the size of the fuel grains.

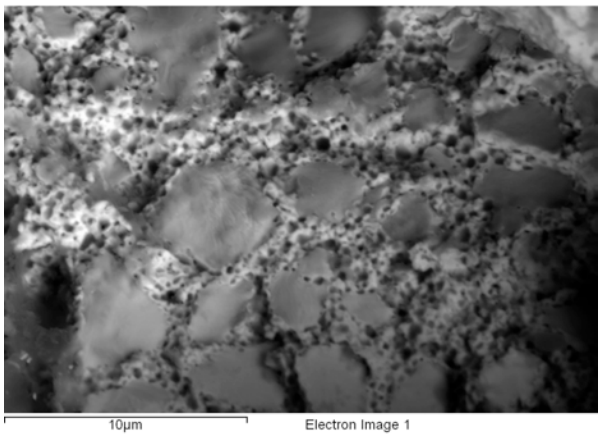

Figure 2: SEM images of a fracture surface R2R040 (Low) showing high density intergranular bubbles along cell boundaries.

Electron diffraction patterns were obtained in TEM analysis to better understand the stability of the gamma phase of U-Mo during irradiation. The diffraction patterns indicate that the U-Mo is remaining in a BCC structure through $5.0x10^{21}$ fiss/cm^3 and has a lattice parameter in good agreement to the expected U-7wt%Mo value. In an as-fabrticated fuel plate, BCC phase U-7wt%Mo fuel particles had a measured lattice parameter value of 3.417 Å [3] (see Fig. 3).

Figure 3: TEM micrographs from irradiated fuel showing a selective area diffraction pattern, z=[110], where the anticipated BCC U-Mo crystalline structure is observed.

3.1.2 Fission Gas Behavior

The intragranular bubbles are of interest as they form an ordered bubble superlattice in the host U-Mo fuel. The bubble superlattice was first reported in [8]. The intragranular bubbles are coherent with the host U-Mo fuel. The bubble superlattice is in a FCC structure, while the host U-Mo fuel is in a BCC structure. Figure 4a shows the bubble superlattice at an orientation of z=[110] in U-Mo, where the bubble superlattice has long range ordering with ordering seen in the entire U-Mo grain. Figure 4b shows satellite spots from the bubble superlattice in the selective area diffraction pattern. The d-spacing of the spots correlate well with the measured spacing of the bubble lattice in the TEM bright-field images. Figure 5 shows the intragranular bubble distribution from sample R2R040 at a fission density of 3.3×10^{21} fiss/cm^3. This type of distribution was consistent with the other samples where the bubble superlattice sizes could be measured.

a) 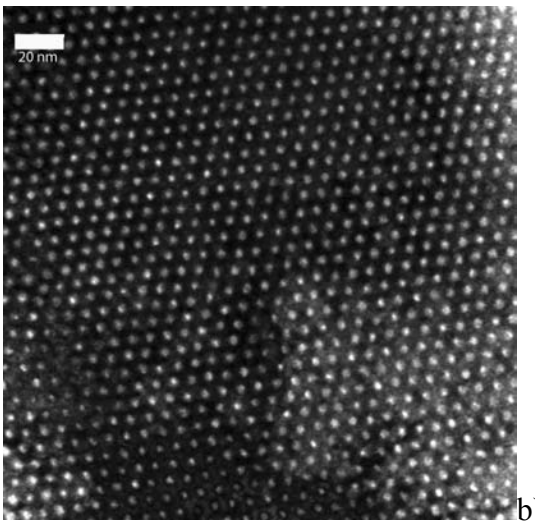

b) 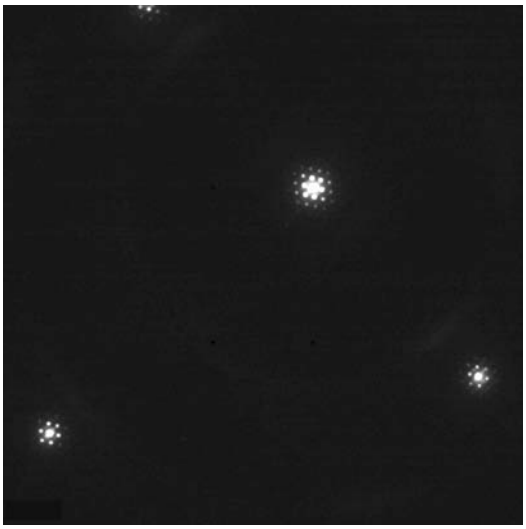

Figure 4: TEM micrographs showing a) the bubble superlattice in a z=[100] orientation and b) selective area diffraction pattern showing the satellite spots from the bubble superlattice.

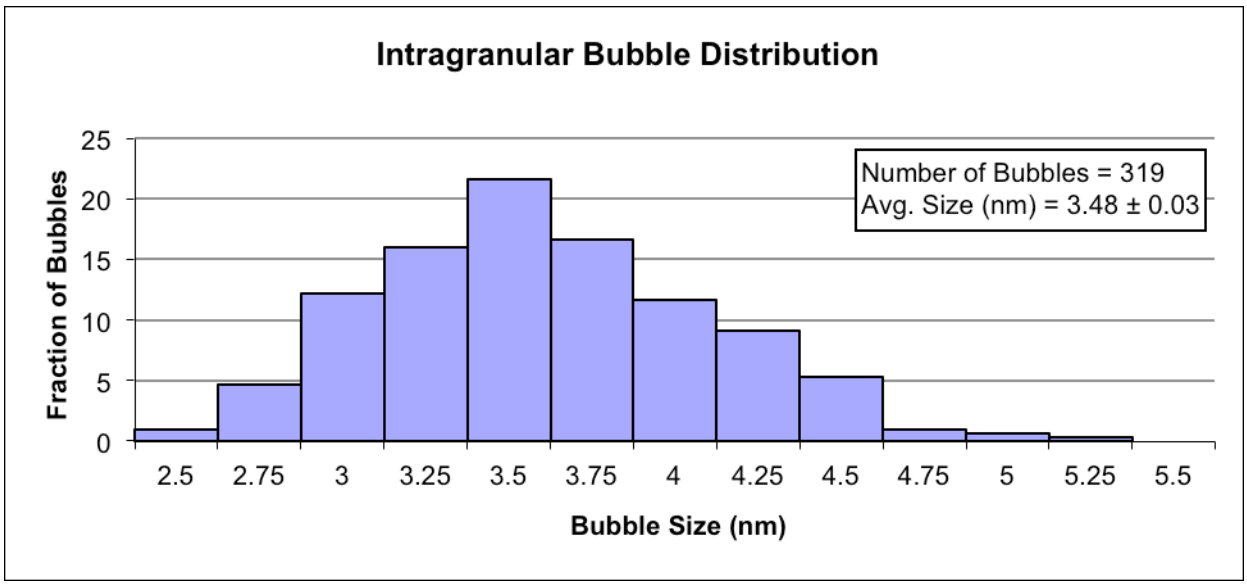

Figure 5: Intergranular bubble distribution in sample R2R040.

As seen in Figure 4a, the intragranular bubbles appear to be circular in shape but it is likely that they are faceted bubbles as the host material is crystalline. The bubbles appear circular due to stacking of other bubbles below the top bubble when in a specific zone orientation. This provides an illusion that they are circular due to overlap. Table 2 provides the average bubble size, the lattice spacing of the bubble superlattice at various fission densities, and the % swelling contribution of these bubbles. The swelling contribution of the bubbles was found by finding the volume of a fission gas bubble; multiply that by the number of bubbles in a FCC bubble lattice (four), and divide that by the volume of U-Mo present in one "bubble lattice". The superlattice lattice spacing has a significant effect on the % swelling of the fuel. The measured bubble sizes are likely larger than the real size due to the bubble stacking phenomenon. Also, note that bubble sizes were measured at a fission density of 5.16×10^{21} fiss/cm^3 indicating that the bubble size of 3.62 nm is likely the largest size bubble sustainable by the bubble superlattice.

Table 2: Intragranular bubble size, spacing, and swelling contributions.

Sample ID	Bubble Size (nm)	Spacing (nm)	Fission Density (fiss/cm^3)	Swelling (%)
R2R040 (RERTR7-Low)	3.12	12.1	3.3	3.9
R2R010 (RERTR6)	3.48	11.1	4.5	6.5
R3R050	3.62	12	5.2	5.8

As seen in Figure 4a, the bubble superlattice has long ranging ordering properties. TEM analysis was performed around grain boundaries and intergranular bubbles to better understand when the host U-Mo will not accommodate the bubble superlattice, i.e. the denuded bubble zone. Figure 5 shows the denuded zone adjacent to an intergranular bubble. It appears that the superlattice cannot be sustained when within 20-100 nm of an intergranular fission gas bubble. Along grain boundaries, it was unclear when the superlattice fails though it is anticipated to be less than the denuded value around intergranular fission gas bubbles. Additional work is needed to better understand true denuded regions.

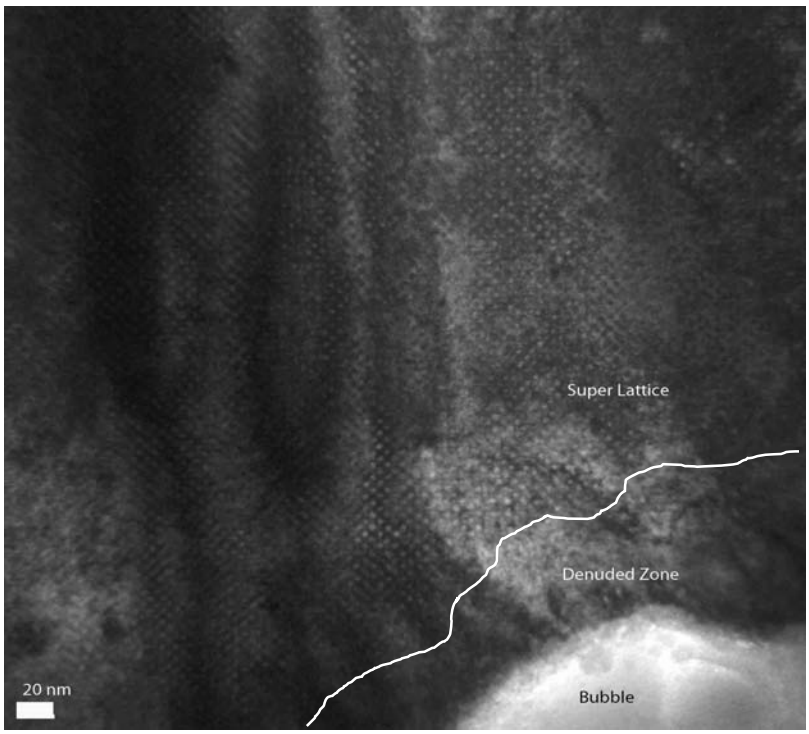

Figure 5: TEM micrograph showing a denuded bubble superlattice zone near an intergranular fission gas bubble

In addition to the intragranular bubbles in the bulk of the fuel grains, intergranular bubbles are present along the grain/cell boundaries of the fuel. SEM analysis of these bubbles is restricted to those along fracture surfaces in the fuel. The intergranular bubbles on the planer surface of the fuel sample are not the true size of the bubble, due to the smearing of polishing material into the bubbles. With the addition of the FIB, cross sections of the fuel can be obtained and the true bubble size distribution can be found. A FIB'd cross section an irradiated fuel plate can be seen in Figure 6. The intergranular bubbles are faceted in shape and to determine the average size of the bubbles, the longest and shortest distance of the bubble was obtained and the average of these two measurements were used to obtain an average diameter for the bubbles.

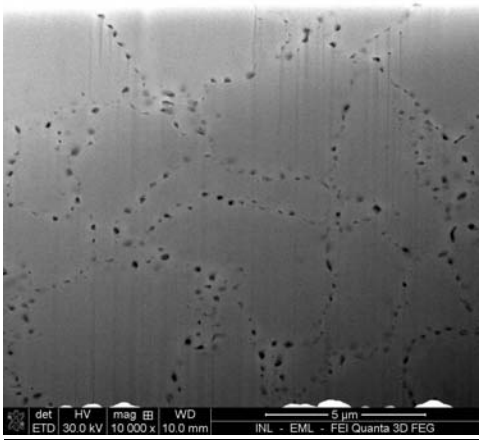

Figure 6: SEM micrograph of the microstructure for a sample taken from irradiated fuel using a FIB.

3.2 High Burnup Microstructure

In Table 1, it can be seen that three U-7Mo samples have been analyzed in the SEM and TEM above $5x10^{21}$ fiss/cm^3. Creating useful TEM samples of the high burnup microstructure was difficult to achieve. This is due to the microstructure of the fuel at these fission densities. Figure 7 shows the typical high burnup microstructure. The fuel microstructure is dominated by randomly distributed homogenous bubbles. The SEM image in Fig. 7a was taken from R3R050 along a fracture surface. Note that some fuel grain structure can be seen still indicating that transition to the high burnup structure is not complete. Fig. 7b shows the bubble distribution observed for a FIB sample taken from the R2R040 high flux sample.

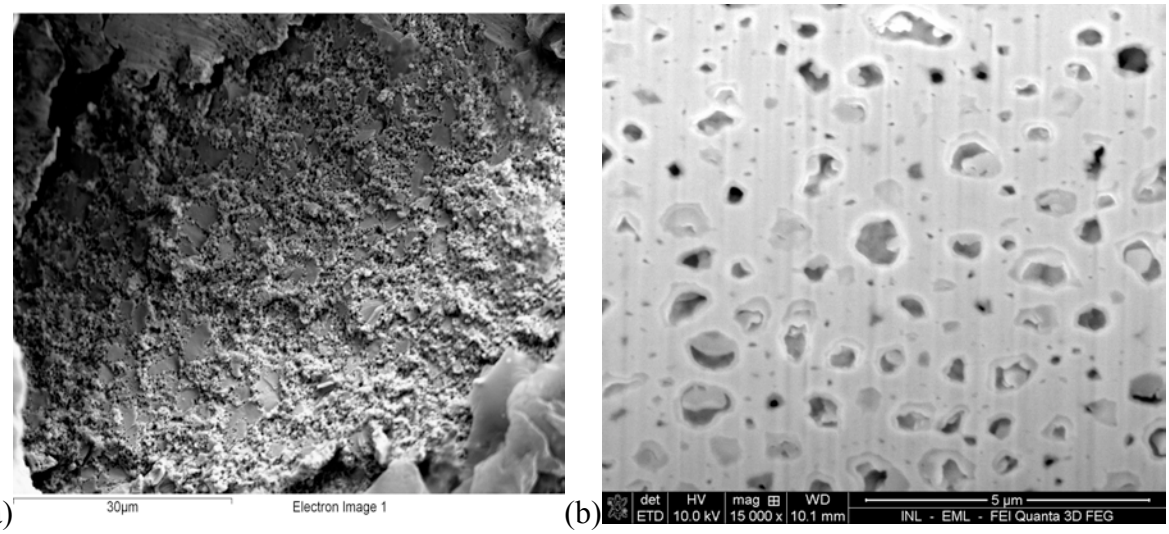

Figure 7: (a) Fracture surface of sample R3R050 showing a high density of intergranular fission gas bubbles and fuel grain sizes, and (b) SEM micrograph of R2R040 (high-flux) FIB sample, where solid fission products are present in the fission gas bubbbles.

3.2.1 Stability of U-Mo

TEM characterization of the structure of the U-Mo fuel above $5x10^{21}$ fiss/cm^3 shows that there is both crystalline and amorphous fuel present. The crystalline U-Mo fuel remains in a BCC structure as was seen below fission densities of $5x10^{21}$ fiss/cm^3. Another key observation is the size of the grains in the fuel. Most grains and amorphous regions are now sub-micron in size, with sizes ranging down to 100 nm. From Figure 8, some micron sized grains are still present and within the areas with high density intergranular bubbles, the fuel grains are nano-sized. Figure 8a shows a bright field image of an area where crystalline and amorphous fuel is present, 8b shows a selective area diffraction pattern of the crystalline fuel present in Figure 8a, 8c shows a ring pattern of the amorphous U-Mo fuel region in Figure 8a, and 8d shows a TEM image showing nano-sized grains in the fuel along with residual ordered superlattice bubbles. Another key observation in Figure 8d is that some crystalline fuel grains are very close in crystal orientation indicating that the recrystallization could have occurred with the larger micron fuel grains subdividing into smaller grains with very similar crystal orientation.

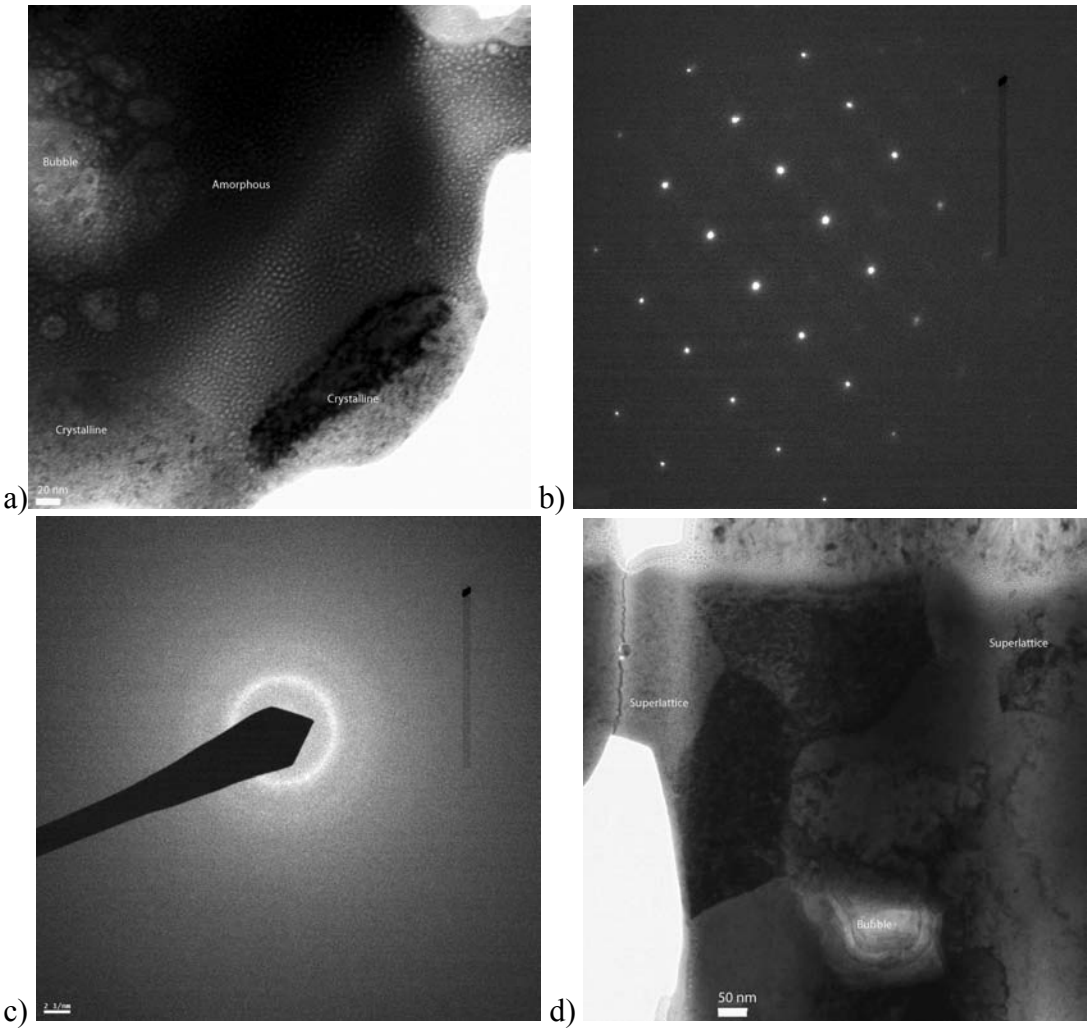

Figure 8: TEM micrographs showing a) crystalline and amorphous fuel grains, b) selective area diffraction of a crystalline fuel grain in a), c) selective area diffraction of the amorphous fuel grain in a), and d) residual bubble ordering in the fuel grains.

3.2.1 Fission Gas Behavior

As seen in Figure 7, the microstructure at high fission density is dominated by randomly distributed homogenous fission gas bubbles throughout the fuel grains. TEM analysis of the grains shows that in general the majority of the bubble superlattice has collapsed in the bulk of the fuel grains. Some areas show residual bubble superlattice and this can be seen Figure 8d. The remaining bubble superlattice is likely related to the micron sized grains still present in the high burnup fuel microstructure. Additionally in Figure 8d the neighboring crystalline grains are devoid of the fission gas bubbles, indicating that the fission gas that was stored in the bubble superlattice has been released and has likely formed these larger intergranular bubbles seen in Figure 7. In sample R2R040 high flux, a fuel area was found that appears to have just gone amorphous. In this area, fission gas bubbles appear to have just been in a bubble superlattice structure prior to amorphization, with some apparent ordering still being present in the amorphization structure. This can be seen in Figure 8a. Notice near the large bubble in the upper left of the micrograph that the small intragranular bubbles may be starting to interlink to form larger bubbles. Additionally in Figure 8a, crystalline fuel grains can be seen adjacent to the

amorphous fuel region. These crystalline regions are devoid of fission gas bubbles, indicating that the superlattice has collapsed in these grains and the fission gas has diffused/been released to other sinks.

3.3. Solid Fission Products

Solid fission products have been seen in the fuel in the form of metallic inclusions (see Fig 7b). These solid fission products were primarily found inside the intergranular bubbles. This is also shown in Figure 9. The circled areas indicate where solid fission products and fission gas bubbles are co-located. EDS analysis of the fission products show that significant concentrations of Sr, Y, Nd, and Ba are present in these precipitates. Common observations seen are that the Ba, Sr, and Y seem to precipitate together while the Nd forms its own clusters. It is unclear to see if there are solid fission products present in the fuel itself in solution. EDS measurements show small contributions of expected solution fission products (Cs, Nd, Y, Zr) in various areas but useful observations cannot be made. EDS measurements do show increased molybdenum concentrations, up to 3-5 wt%, in the fuel regions. This is to be expected with increasing burnup since the uranium concentration decreases and the molybdenum concentration increases as a result of nuclear fission.

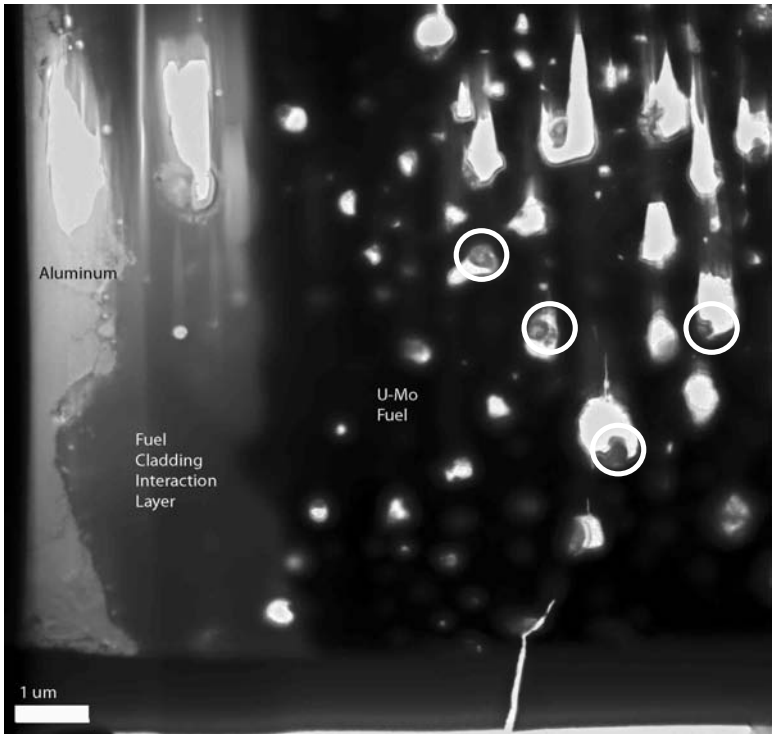

Figure 9: TEM micrograph showing solid fission products inside of fission gas bubbles

4. Discussion

In the low burnup microstructure, the bubble superlattice is the major feature present in the fuel. It is not clear how the bubble superlattice is initiated. Bubble superlattices have been seen in ion implantations [12,13]. In addition to bubble superlattices, void superlattices have been seen

[14,15]. Typical bubble superlattice have bubble sizes and spacings of 1.5-2.5 nm and 4-6.2 nm, respectively [13]. Void superlattices have void size and spacings of 4-78 and 20-75 nm, respectively . Void superlattices tend to form at irradiation temperatures $>0.25T_m$ [16] while bubble superlattices appear below $0.25T_m$ [13]. The melting temperature,Tm, of U-7wt%Mo is ~1416˚C, and the fuel's irradiation temperature is $0.26T_m$. Void superlattices tend to show significant long range ordering when compared to ion implantation bubble superlattices. These observations tend to support that the superlattice seen in U-Mo fuels is indeed a bubble superlattice though the bubble lattice shares similarities with void superlattices. To confirm the bubble superlattice, it would be beneficial to look at the bubble chemical composition in a field emission TEM.

It is unclear how the bubble superlattice forms in the U-Mo fuel. The samples analyzed in the TEM show that the bubble superlattice is completely formed at a fission density of $3.3x10^{21}$ fiss/cm^3. Therefore, the superlattice starts forming below a fission density of $3.3x10^{21}$ fiss/cm^3. To understand how the superlattice is formed, low dose irradiations are necessary. One proposed mechanism on how the bubble superlattice forms is dislocation loop punching [16-18]. In this process, an overpressurized bubble is seeking to reduce its pressure. It does this to increase its volume by dislocation loop punching. U-Mo atoms on the surface of the bubbles are "punched" into the U-Mo material. The punching is done in a favorable low energy crystalline direction. The removal of the surface atoms increases the volume of bubble, thus decreasing the pressure inside the bubble. The increase in volume also causes the "center" of the bubble to shift ½ a burgers vector in the direction of the dislocation loop. This is how the bubble moves around where it was nucleated.

The dislocation loops in the material will start to interact with neighboring bubbles. The neighboring bubble will start to see dislocation loops in many directions and will likely punch a dislocation in another direction that is more energetically favorable. Eventually, the bubbles will settle in a low energy location and form the ordered bubble superlattice that is seen in the low burnup microstructure.

When the bubble superlattice is formed, fission gas will continue to increase with increasing burnup. The bubble superlattice will accommodate the gas as was seen in Table 2 with the bubble sizes increasing with higher burnups. Ion implantations were shown to have increasing bubbles sizes with dose [12,13]. The ion implanted bubbles were shown to have a saturation size. Upon reaching the maximum bubble size, the superlattice collapses. It is unlikely that the maximum bubble size would be greater than 3.62 nm. This bubble size was seen at a fission density of $5.16x10^{21}$ fiss/cm^3, slightly above the anticipated transition from the low burnup microstructure to the high burnup microstructure.

Understanding how the U-Mo bubble superlattice collapses is a much more difficult question to address. There appears to be two possible mechanisms on how the bubble superlattice collapses in U-Mo fuel. As was seen in Figure 8c, the U-Mo host material has undergone amorphization. It appears that the fuel grain has just gone from a crystalline state to an amorphous state as the fission gas bubbles appear to have some ordering remaining and have bubble sizes consistent with the superlattice.

The other mechanism of how the bubble superlattice collapses could be related to grain subdivision process. In grain subdivision, a material incurs significant stress that causes the material to not retain its current grain size. The stress is relieved by the grain collapsing into smaller grains. The grains tend to have close orientations to their recrystallized neighbors from the original grain. This was seen in Figure 8d where fuel grains were seen to have very similar orientations. The grain subdivision process in U-Mo could be related to the stress incurred from the bubble superlattice. As there is an increase in fission gas inventory with increasing burnup, the superlattice bubbles will accommodate fission gas. This increase in bubble pressure and size leads to increased stress in the fuel. Eventually, the material will be forced to subdivide to reduce stress. Similar grain subdivision can be seen in the high burnup rim structure in the irradiated UO_2 fuel [19].

As was seen in the high burnup microstructure, the fuel grains are now sub micron with some seen around 100 nm. With the decreased grain size, there is an increase in the grain boundary density. With the denuded zone of the bubble superlattice being up to 100 nm, many fuel grains may potentially not sustain the bubble superlattice. It needs to be determined if the denuded zone width changes with the type of grain boundaries. For low angle grain boundaries (observed in the current samples), the denuded zone width can be significantly reduced due to the reduced sink strength. Additionally, when the host grain undergoes grain subdivision, the driving force is to reduce the stored stress in the grain. By subdividing, new defect-free grains are created thus reducing the internal stress of the host grain. When the grain subdivides, it should release the gas stored up in the bubble superlattice, allowing for the gas to diffuse to the grain boundaries and form intergranular bubble structure seen in the high burnup microstructure. The subdivided, submicron grains have clean grain boundaries and did not show any bubble decorated subgrain boundaries.

Solid fission products precipitates were seen to reside inside of the intergranular bubbles of the U-Mo fuel. This is consistent to observations seen in irradiated UO_2 fuel [20]. It has been shown that fission gas bubbles in UO_2 contain Mo, Pd, Tc, Ru, Rh, Ba, and Zr precipitates. The Ba and Zr were often found together and appear to form the barium zirconate structure. The Mo, Pd, Tc, Ru, and Rh tend to form metallic fission precipitates. These intergranular bubbles are sinks for the fission products to accumulate due to two diffusion mechanisms. The intergranular bubbles both reside on the grain boundaries, which leads to increased diffusion, and the bubbles have increased local temperature in/around the bubble, leading to increased diffusion to the bubble. The metallic inclusion in the intergranular bubbles of the U-Mo metallic fuel show that fission product behavior is very similar to that seen in UO_2 regardless of the significant difference in irradiation temperatures.

5. Conclusions

There are two distinct microstructures seen in irradiated U-Mo fuels. There is a low burnup and a high burnup microstructure with the transition between the two starting to occur around a fission density of 5×10^{21} fiss/cm^3. The low burnup microstructure is dominated by intergranular fission gas bubbles and an ordered bubble superlattice present inside the bulk of the grains. The bubble superlattice is FCC in crystalline structure compared to the host U-Mo BCC crystalline structure. Bubble sizes range from 2-3.6 nm in size with lattice spacings between 11-12 nm. Grain sizes were shown to be on the single micron scale. A denuded superlattice bubble zone was seen within 20-100 nm of intergranular fission gas bubbles.

The high burnup microstructure is dominated by randomly distributed homogenous intergranular bubbles. Fuel grain sizes were shown to be primarily sub-micron indicating that recrystallization has occurred though some areas still show micron sized grains. The U-Mo was shown to be both crystalline and amorphous in structure. Residual bubble superlattice was seen in various locations that were likely tied to the micron sized grains. Solid fission product precipitates were seen in the fuel in both the low and high burnup microstructures. Solid metallic precipitates were seen to reside inside the large gas bubbles.

Acknowledgments

This work was supported by the U.S. Department of Energy, Office of Nuclear Materials Threat Reduction (NA-212), National Nuclear Security Administration, under DOE-NE Idaho Operations Office Contract DE-AC07-05ID14517. Personnel in the Hot Fuel Examination Facility are recognized for their contributions in destructively examining fuel plates.

References

[1]. J. Snelgrove et al., Nucl. Engr. Design 178 (1997) 119-126.
[2] D. Wachs et al., Proc. of *GLOBAL 2007*, Boise, ID, September 9-13, 2007.
[3]. D. Keiser, Jr. et al., Mat. Char. 61 (2010) 1157-1166.
[4]. D. Keiser, Jr. et al., J. Nucl. Mater. 412 (2011) 90-99.
[5]. A. Leenaers. et al., J. Nucl. Mater. 335 (2004) 39-47.
[6]. W. Van Renterghem et al., 31st International Meeting on Reduced Enrichment for Research and Test Reactors, Beijing, China, 2009.
[7]. J. Rest et al., Proc. of the International Meeting on Research Reactor Fuel Management, Hamburg, Germany, 2008.
[8]. S. Van den Berghe et al., J. Nucl. Mater. 375 (2008) 340-346.
[9]. J. Gan et al., J. Nucl. Mater. 396 (2010) 234-239.
[10]. J. Gan et al., J. Nucl. Mater. 424 (2012) 43-50.
[11]. K. Kim et al., J. Nucl. Mater. 245 (1997) 179-184.
[12]. P. Johnson et al., J. Nucl. Mater. 218 (1995) 273-288.
[13]. P. Johnson et al., Nucl. Inst. Meth. Phys. Res. B 243 (2006) 325-334.
[14]. B. Loomis, J. Nucl. Mater. 68 (1977) 19-31.
[15]. J. Evans, J. Nucl. Mater. 119 (1983) 180-188.
[16]. V. Dubinko et al., Appl. Pysi. A. 58 (1994) 21-34.
[17]. W. Wolfer, Phil. Mag. A. 58(2) (1988) 285-297.
[18]. W. Wolfer, Phil. Mag. A. 59(1) (1989) 87-103.
[19]. T. Wiss et al., JOM 64(12) (2012) 1390-1395.
[20]. I.L.F Ray et al., J. Nucl. Mater. 188(1992) 90-95.

STRESS CRITERIA OF FUEL ASSEMBLY FOR STRUCTURAL INTEGRITY IN A RESEARCH REACTOR

J.S.YIM, H.J.KIM, J.Y.OH, Y.W.TAHK, B.H.LEE
Nuclear Fuel Design for Research Reactor, KAERI
zip305-353, 111 Daeduok Daero 989 Beon-gi, Yuseong-gu, Daejon, KOREA

ABSTRACT

In the design of fuel assemblies (FAs), maintaining the structural integrity is a major concern to achieve the intended functions of the FA and secure the safety of a reactor. Through the design and evaluation processes, FA integrity must be assured by analyses or tests or combining the two. In the evaluation of the structural integrity for most PWR FAs in Korea, the stress categories and strength theory presented in ASME Section III have been used as a general guide. Regarding the successful application of ASME on the structural integrity of PWR FAs in Korea, stress criteria of a FA for research reactors are set up. For the purpose of ensuring fuel integrity during the intended operational conditions such as normal operation conditions, anticipated operational occurrences (AOO) and avoiding a loss of coolable geometry of FAs during dynamic loads occurring as a consequence of the SSE horizontal events, the stress criteria are specified and the stress limits are presented in this study.

1.0 INTRODUCTION

As a general guide in the nuclear fuel design for research reactors (RRs), the NUREG 1537 [1] is used, which states that “Maintaining fuel integrity should be the most important design objective.” The design requirements for research reactors are also found in IAEA-NS-R-4 [2].

- The reactor core shall be designed so that fuel damage in the design base accidents would be kept within acceptable limits.
- The reactor core shall be designed so that the reactor can be shut down, cooled, and held as subcritical with an adequate margin for all operational states and for DBAs.

In compliance with references [1], [2], and [3], the design requirements of the FAs in RRs selected for operation conditions are as follows:

- The fuel system shall not be damaged during normal operation and AOO.
- The fuel system damage is never so severe as to prevent a control rod insertion when it is required.
- The number of fuel rod (or fuel plate) failures shall not be underestimated for postulated accidents.
- Coolability of the fuels shall always be maintained.

Nuclear fuel design comprises two categories. One is the fuel performance aspect which is related to fission and thermal behaviors. The other is the structural integrity aspect of the FAs. The most significant parameter in the fuel integrity under operational conditions would be temperature from the fission. If this parameter is not properly controlled within a certain limit, swelling, blistering, and severe oxidation on the cladding surface will occur, jeopardizing the integrity of the fuel. The fuel particles and meat behave quite differently from that of an FA structure, and thus the two categories are described and analyzed separately in the safety analysis report (SAR).
In the design of nuclear fuel, it is necessary to establish design criteria in advance to secure

the integrity of the fuel system. To maintain the fuel integrity throughout its operational lifetime in the core, the fuels should be operated under certain limits. For an evaluation of the structural integrity of FAs, the vibration characteristics, static and dynamic load effects, material property degradation, and chemical and neutronic effects should be considered. The structural integrity of FAs shall be justified through an analysis or test, or a combination of the two.

The stress categories and stress criteria of FAs in Korean Nuclear Power Plants (NPPs) have been established using ASME Sec. III [4] as a guide and their criteria have been applied successfully [5, 6, and 7]. However, since it has not been well defined for the stress categories and stress criteria for FAs in the RR, it is needed to establish the one that can be applied on the safety evaluation for the RR FAs. In a similar way as many FAs in Korean NPPs, the stress categories and stress criteria of the FAs for RRs are set, and the stress intensity values of the structural material used in the FAs are presented.

2.0 SAFETY CLASSIFICATION OF RESEARCH REACTOR FA

In the design of nuclear FAs, the guidelines presented in the NUREG 1537[1], IAEA NS-R-4[2], and NUREG 0800[3] are taken into consideration. Prior to the design of an SSC (Structure, System and Components) of a reactor, SSCs that are important to safety shall be first specified and then classified according to their function and significance for safety. Codes and standards applicable to SSCs shall be identified and their use shall be in accordance with their classification [2].

PWR FAs have been classified as safety class (SC) 3 according to the ANSI/ANS 51.1(1983) [8], which was re-affirmed in 1988 and withdrawn in 1998. If the FAs are classified as SC-3, design, manufacturing, installation, and tests shall be performed in compliance with the rules and methods prescribed in the ASME Section III ND, and a quality assurance (QA) program shall be performed in accordance with the ASME NQA-1. If FAs are considered as one of the reactor core components, it seems likely to be adequate in applying the ASME section III. However, a fuel design and evaluation should be accomplished and approached by two different aspects.

Since fission related phenomena such as swelling, blistering and material degradation, irradiation creep, relaxation, densification, and irradiation growth are unique and peculiar characteristics of nuclear fuels, applying the ASME section III that aims at pure mechanical strength to fuel performance is unreasonable. Moreover, if the ASME codes are applied to fuel fabrication, manufacturing needs an ASME certificate. Unlike the other reactor components that are manufactured by the ASME certificate holder, nuclear fuel had to be made and supplied by fuel manufacturers, who are obligatorily to be qualified by a nuclear regulatory body by reviewing voluminous documents supporting that the fuel maintains its integrity throughout its lifetime with various out-pile and in-file irradiation tests and PIEs.

Considering the conflicts between the design, manufacturing, and QA mentioned above, FAs have to be classified in safety classification as N/A (Not applicable) and shall be designed with its own design criteria, which are divided into two, one for fuel performance and the other for FA structure, respectively. Doing this not only enables the showing of fuel integrity relating to fuel performance and fuel structural integrity at the same time, but also satisfies the QA requirements in FA manufacturing.

As the fuel design proceeds, the validation and verification of the FA structural integrity shall be confirmed by analyses as well as tests, such as out-pile characteristics tests and in-pile irradiation tests.

2.1 STRESS CATEGORIES AND STRESS LIMITS

In the early time of FA design for PWR in Korea, ASME Section III was used as a general guide to establish the stress categories and stress criteria for the FA structural integrity

evaluation [5, 6, and 7]. Later, the ASME Section III was replaced by the Korean Electric Power Industry Code (KEPIC) [9], which includes similar contents of ASME.
In PWR FAs, stainless steel and zircaloy alloy are used as structural materials with their high performance on strength, anti-corrosion, and neutron economy. Since the PWR FAs are located in between the lower and upper core plates, they have been regarded as one of the core support structures. Thus, the ASME Section III NG, which describes the design rule of the core support structure, has been used as a guide for the structural design of FAs. Meanwhile, the FAs in RRs are usually operated in an open pool with low pressure and low temperature aiming at high neutron utilization. Thus, the material is mainly made of aluminum alloy to achieve relatively high structural strength, corrosion, and neutron economy. Unlike in the case of PWR FAs, the lack of systematic stress criteria and an evaluation method for the FA design in research reactors prompted here the stress criteria, and its limits are to be set based on those of the PWR FA design.
In ASME Section III, the maximum shear stress theory known to be Tresca Criterion for combined stresses is used to determine the stress intensities for the structural material of FAs. The maximum shear stress at a point is equal to one-half the difference between the algebraically largest and smallest of the three principal stresses at a point. The stress intensity is the equivalent intensity of the combined stress. It is defined as twice the maximum shear stress. This theory is generally more frequently used in the industrial field since it is simple to apply and more conservative than the maximum distortion energy theory, which is known as Von Mises failure criterion, and is applicable to the ductile material because the material failure is initiated by shear stress. Considering the ductility of the aluminum material in the FAs for RRs, the failure criteria applied on PWR FAs seem to be applicable on the RR FAs.
In the ASME Section III, the load conditions for the reactor components design are classified according to the plant operation conditions. Similarly, the design conditions for the RR FAs are determined based on the operation conditions according to its occurring frequencies during its lifetime.

1) Normal operation
2) Anticipated Operational Occurrences(AOO)
3) Accidents

In an evaluation of FA structural integrity under normal operation and AOO, no fuel failure is allowed. It is general practice that fuel behavior in accident cases other than Safe Shutdown Earthquake (SSE) and LOCA is dealt by an accident analysis group.
In this paper, plate-type FAs for a RR are selected as an example, and their stress criteria are presented using the ASME section III NG as a guide.
The design stress limits for normal and AOO conditions are set as the design criteria to prevent from structural failure due to stress. As for the design limit, the stress intensity limit shall not exceed the design stress intensity value, S_m, for primary membrane stress, 1.5 S_m, for primary membrane stress plus primary bending stress. The primary membrane stress, plus primary bending stress, plus secondary stress shall not exceed 3 times S_m. The average primary shear stress shall not exceed 0.6 S_m.
In the plate type fuels, the fuel plates (FPs) are inserted in the slots on the side plates to fix them by mechanical deformation, i.e., swaging. Due to the different thermal expansions under external constraints at both lateral edges of the FPs, lateral compressive thermal stress occurs on the FPs of a FA. If an FP is subjected to compressive stress high enough to cause critical buckling stress, the FP can buckle, which results in structural instability and deterioration of the cooling performance by partial narrowing of the coolant channels. To preclude the buckling of FPs, the maximum lateral compressive stress shall be limited to less than the critical buckling stress of the FPs. To preclude the buckling of FPs, the compressive stress shall not exceed the critical buckling stress of an FP.

The SSE is considered as an accident event in the FA design to secure a coolable geometry of FAs. To avoid the loss of coolable geometry of FAs during dynamic loads occurring as a consequence of the SSE horizontal events, the design criteria of stress are specified in the seismic analysis. The design criteria and design limit for stress during an SSE are summarized as the design criterion: A coolable geometry should be maintained during an SSE and thereafter. As for the design limit, the stress intensity limit shall be less than 2.4 S_m or 0.7 S_u for primary membrane stress and 3.6 S_m or 1.05 S_u for primary membrane stress plus primary bending stress. Here, S_u is the ultimate tensile strength.

2.3 STRESS INTENSITY VALUES FOR THE ALUMINUM MATERIAL

The design stress intensity value, S_m, which becomes the allowable limit, should have been defined for the FA mechanical design. This forms the basis for the stress limits not only in the normal and AOO conditions but also in the SSE.

The design stress intensity values at any temperature are given by the lowest of the following [4-7]:

- One-third of the specified minimum tensile strength or 2/3 of the specified minimum yield strength at room temperature.
- One-third of the tensile strength or 90 percent of the yield strength at temperature but not to exceed 2/3 of the specified minimum yield strength at room temperature.

The design limits under normal and AOO conditions and during SSE can be summarized as in Table 1. The material strength in an un-irradiated state is used for conservativeness, since the yield stress slightly increases as the burnup increases [10].

Table 1. Stress Limits during normal and AOO conditions and during SSE

State	Stress criteria	Value (MPa)
		Aluminum alloy 6061-T6
Normal and AOO conditions	$P_m < S_m$ $P_m + P_b < 1.5S_m$ $P_m + P_b + Q < 3S_m$ $\tau < 0.6S_m$	96.3 144.5 288.9 57.8
SSE	$P_m <$ Min ($2.4S_m$ or $0.7S_u$) $P_m + P_b <$ Min ($3.6S_m$ or $1.05S_u$)	203.0 304.5
Where, P_m, P_b, Q are primary membrane stress, primary bending stress and secondary stress, respectively, defined in ASME Sec. III. τ is shear stress.		

3.0 CONCLUSION

Stress criteria and its limits are suggested for the design of nuclear fuel assemblies for research reactors. Considering the ductility of the aluminum material of RR FAs, the ASME Sec. III is used as a general guide for the stress categorization and establishing the stress intensity values. The maximum shear stress theory, naming the Tresca criterion for combined stress is used to determine the stress intensities for the structural material (Al 6061-T6) of FAs. The material strength in an un-irradiated state is used for conservativeness, since the yield stress slightly increases as the burnup increases.

Acknowledgement

This work has been carried out under the KJRR Projects operated by the Korea Atomic Energy Research Institute.

4.0 REFERENCES

[1] NUREG-1537, Guidelines for preparing and reviewing applications for the licensing of non-power reactors, Format and contents
[2] IAEA NS-R-4, Safety of Research Reactors, Safety Requirements
[3] NUREG-0800, Standard Review Plan (SRP) for the review of safety analysis reports for nuclear power plants
[4] ASME Boiler and Pressure Vessel Code, Section III, 2004, The American Society of Mechanical Engineers.
[5] Final Safety Analysis Report (FSAR), Kori Unit 1, 2, 3 and 4, Korea Electric Power Cooperation
[6] Final Safety Analysis Report (FSAR), Uljin Unit 1, 2, 3 and 4, Korea Electric Power Cooperation
[7] Final Safety Analysis Report (FSAR), Youngkwang Unit 1, 2, 3 and 4, Korea Electric Power Cooperation
[8] Nuclear safety criteria for the design of stationary pressurized water reactor plants ANSI/ANS 51.1, 1983(R1988)
[9] Korea Electric Power Industry Code (KEPIC), MD, 2005, Korea Electric Association.
[10] J.S.Cheon, Y.S.Kim, ANL/RERTR/TM-12-6, Material Properties of Aluminum Alloys and Pure Zirconium for Use in high density fuel development for RRs

Construction and design of the new irradiation facility for 4” silicon ingots

M. Koleska, J. Ernest, M. Marek, K. Vonkova, J. Soltes
Reactor Services Section
Research Centre Rez, Husinec – Rez 130, 250 68 Rez – Czech Republic

ABSTRACT

Neutron transmutation doping is one of the most important methods for doping of silicon ingots. Many research reactors worldwide, including LVR-15, provide this service as one of their main activities. The demand for ingots’ sizes covers a range of diameters from 2” up to 8”. Limited space available in the LVR-15 reactor core enables doping up to 4” Si ingots only. To extend the irradiation capacities focused on neutron transmutation doping a new facility was installed in the reactor core. The optimization and design of the new irradiation facility will be described. Methodology of optimization and theoretically achievable parameters will be presented. The optimization was performed using two different approaches: with MCNPX Monte Carlo code and NODER 3D diffusion code.

Introduction

Neutron transmutation doping (NTD) is one of the most important methods used creating the n-type semiconductors by changing small amount of silicon into phosphorous atoms. After this process, the silicon ingots become suitable for various purposes ranging from miniature electronic diodes and microprocessors to larger photovoltaic panels. This wide range of applications requires a vast scale of ingots, in major range from 2 inch to 8 inch diameter. With the rapid growth of photovoltaic, the 6 and 8 inch ingots are the most in demand nowadays.

In order to be able to cover the higher demand on NTD silicon ingots, a new rotational irradiation channel dedicated for NTD was developed for the LVR-15 reactor. With respect to the construction and utilization of the reactor, the maximal dimension of silicon ingots irradiated in the new device was 4 inch in diameter.

Criteria used for the development

In the post-irradiation processing of the NTD silicon ingots, the final resistivity distribution of the ingot is evaluated. For such evaluation, three criteria are used for description of the radial homogeneity, axial homogeneity, and deviation from the target resistivity value (irradiation accuracy). These criteria are defined for measured resistivity values ρ according to [1] as following:

radial homogeneity $$RRG = 100 \times \frac{\rho_{\max} - \rho_{\min}}{\rho_{\min}} [\%]$$

axial homogeneity $$ARV = 100 \times \frac{\rho_{\max}^{plane} - \rho_{\min}^{plane}}{\rho_{\min}^{plane}} [\%]$$

irradiation accuracy $$IRRACC = 100 \times \frac{\rho^{average} - \rho_{target}}{\rho_{target}}$$

From the constructional point of view, the RRG is influenced by the rotation of the irradiation channel and the IRRACC is a function of irradiation time. Hence, the only criteria influenced by the construction of the irradiation channel, is the ARV. As the resistivity of the silicon ingot is proportional to the neutron fluence and the according neutron spectra (which can also affect the quality of NTD) that do not dramatically change across the ingot volume, the criteria can be transformed to

$$ARV = 100 \times \frac{\phi_{\max}^{plane} - \phi_{\min}^{plane}}{\phi_{\min}^{plane}} [\%] .$$

To ensure optimal irradiation performance, the ARV must be as low as technically achievable with respect to the fabrication limits for the facility and neutron fluence rate on the crystal. The theoretical criterion for the optimization limit was chosen to be ARV < 1%.

Nominal parameters and conceptual design

The optimization of the irradiation facility was performed for an anticipated core configuration loaded during the use of the facility and for nominal dimensions of the irradiated silicon ingots. The core layout was configured for full utilization of the reactor, including material testing rigs, 2 NTD facilities, and irradiation channels for 99Tc generators (Fig. 1). The core was modelled with equilibrium burn-up in the MCNPX Tier-2 inventory of fission products. The new irradiation facility was assumed to be located in the F,G-9,10 positions of the core.

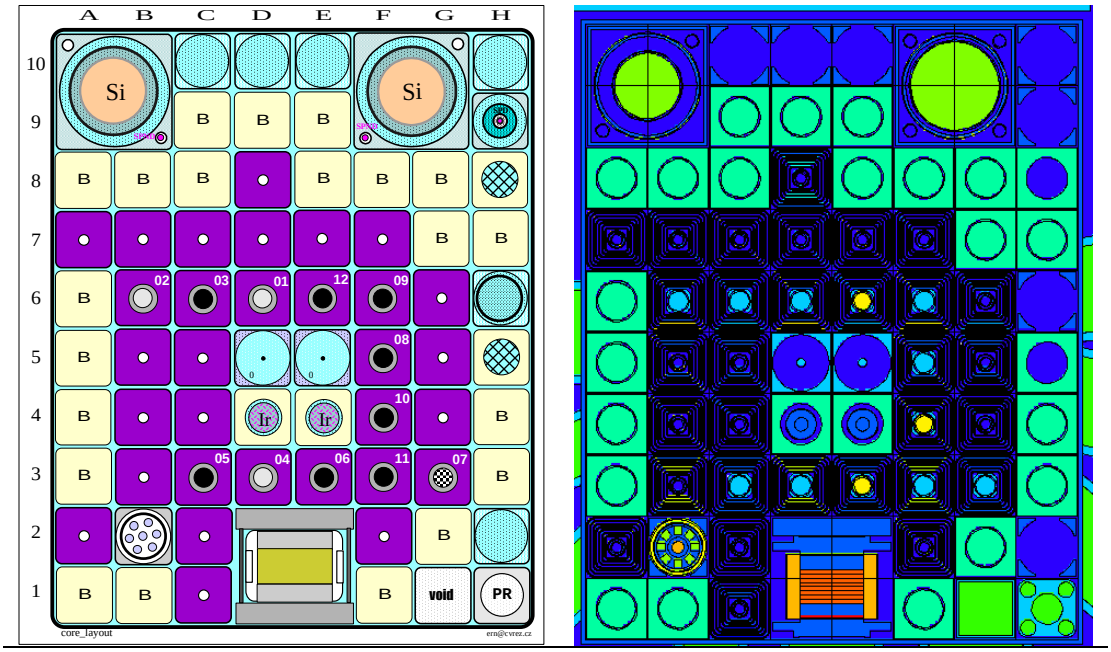

Fig. 1 Reference core layout (kartogram vs. MCNP model)

The silicon ingot was set to have nominal dimensions; 103 mm in diameter and a length of 310 mm. The irradiation capsule was designed to have two graphite blocks from both sides of the ingot, each 50 mm thick (Fig. 2).

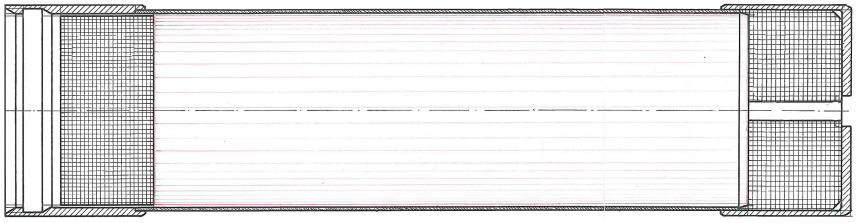

Fig. 2 Irradiation capsule

The irradiation facility consists from several components: the displacer, the irradiation channel and a measurement system.

The displacer, which is placed into the core, was designed and fabricated according to the existing NTD facility without any change. For the monitoring system, which is connected to the irradiation channel, a significant improvement was done for both, the old and the new facility. The measuring system was reequipped with 3 Rh self-powered neutron detectors (instead of 1), so that a more accurate axial distribution of neutrons can be determined.

The basic functional principle of the irradiation channel also remained the same as for the older facility; the whole irradiation channel can be rotated and axially positioned. The main improvement for the new channel was the redesign of the shielding part.

New design of the shielding part of the irradiation channel

The first task of the shielding re-design was the choice of a appropriate shielding material. As suitable material, two materials were chosen and tested – the nickel alloy Inconel and stainless steel 17246. As testing geometry, an old design of the shielding layer was chosen – 3 layers with total thickness of 1,5 mm. The calculation results are shown in the Fig. 3.

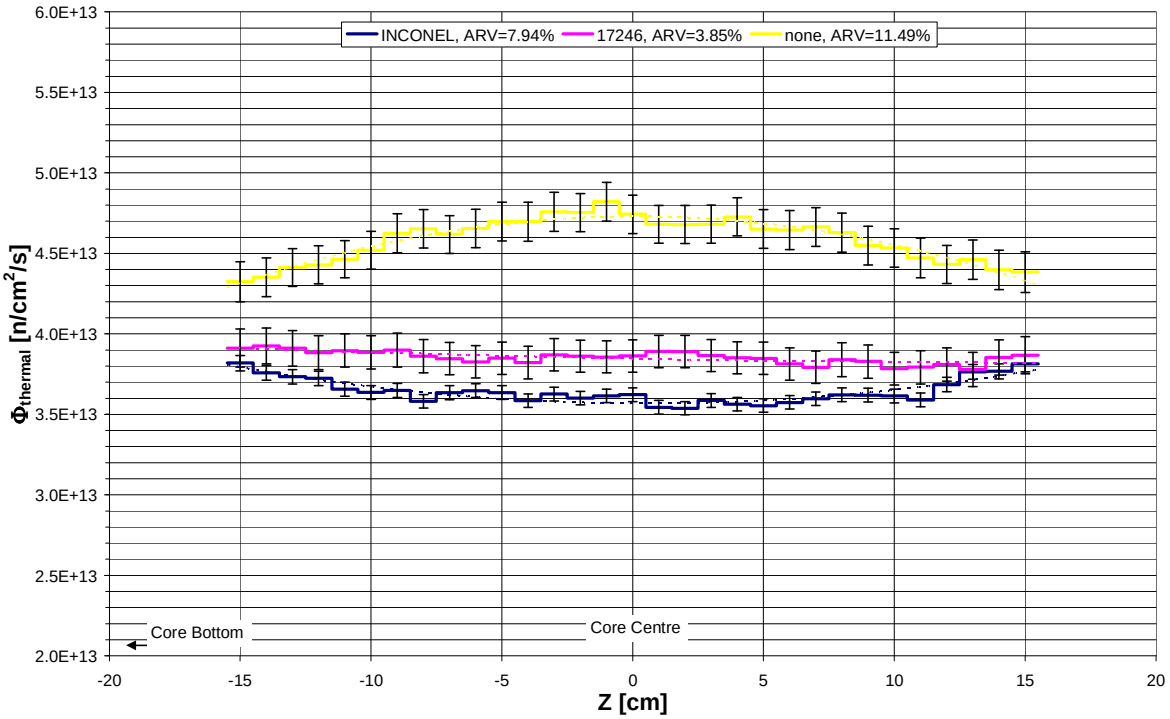

Fig. 3 MCNPX calculation of material shielding ability

According to the results, stainless steel was chosen as optimal material. The reason was that the shielding ability of Inconel is too high for the demanded purposes; optimal arrangement would need the shielding layer thickness lower than the fabrication limit of 0.5 mm.

The next step of the optimization was performed by the NODER code. By this code, an optimal configuration was arranged. For the first step, an optimal length of the lower layer of the shielding referred to as “Ls” was found. After that, a second layer with length “Lss” was designed. This two-layer design met the optimization limit for the nominal ingots dimensions. The optimization results are shown in Fig. 4 and Fig. 5

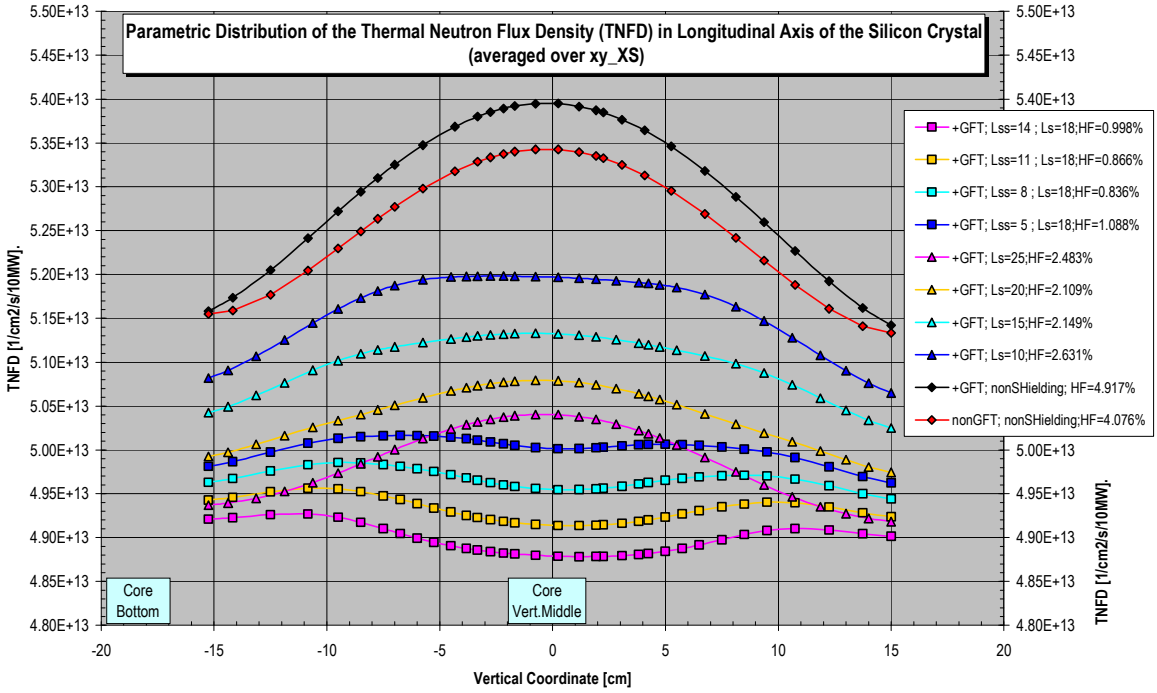

Fig. 4 Shielding layer thickness performance (NODER)

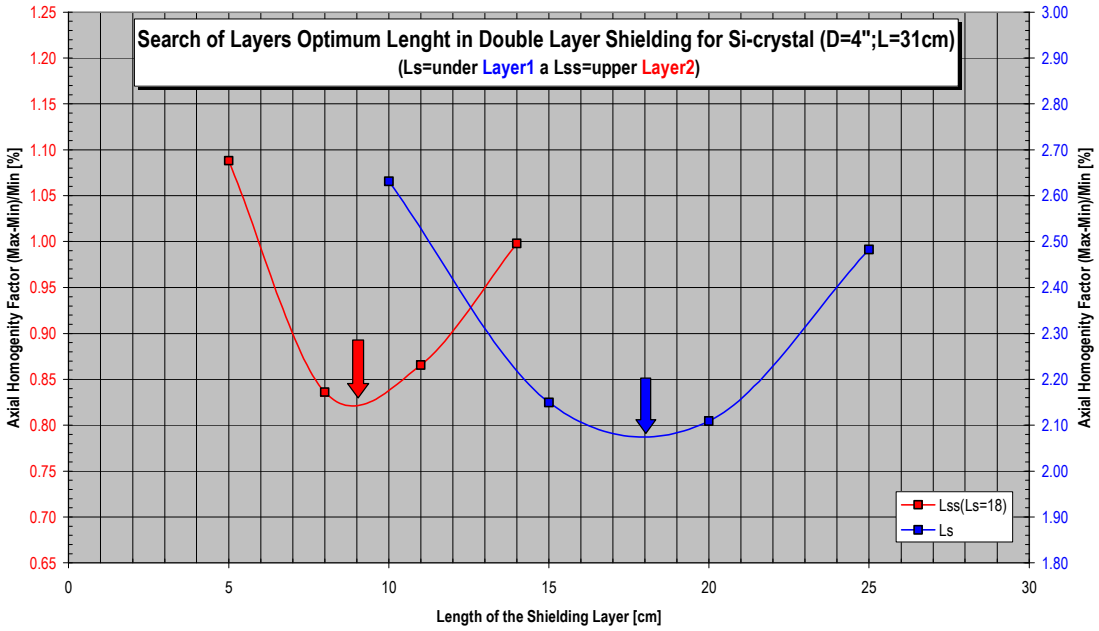

Fig. 5 Optimal shielding layer thickness (NODER)

After receiving optimal layer dimensions, one more variation was performed (Fig. 6). This dimensional variation revealed other optimal configurations with even better ARV values. The disadvantage of these new setups was a slight decrease of thermal neutron flux in the silicon ingot.

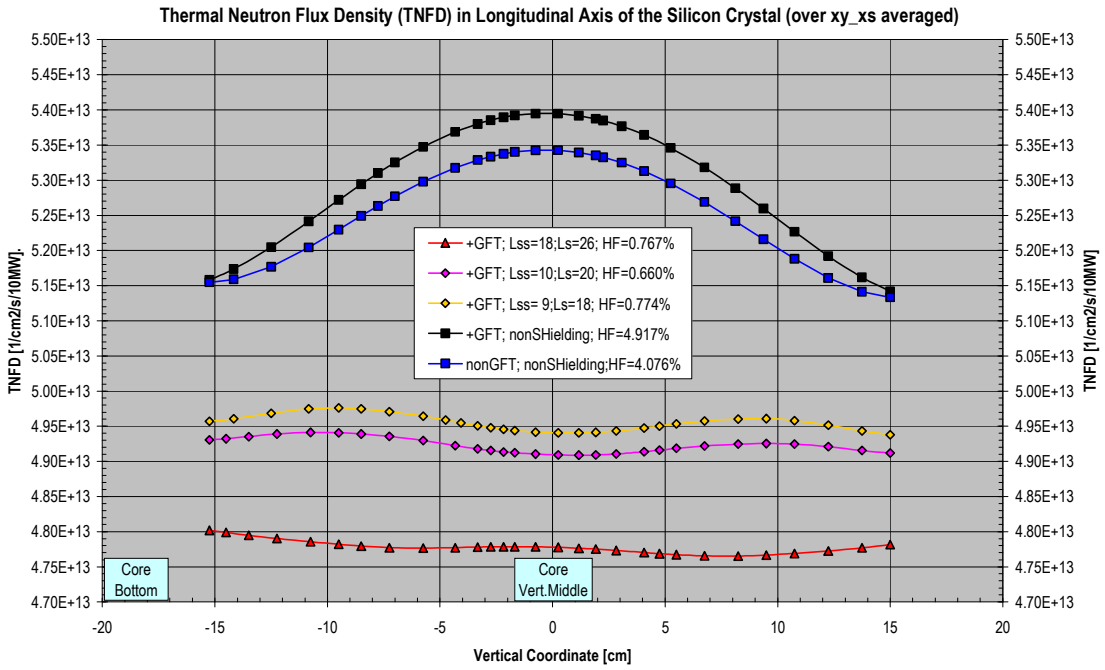

Fig. 6 Optimal shielding layer thickness variation(NODER)

Fig. 7 Irradiation channel with shielding layer

Irradiation parameters of the new irradiation device

For the new device (Fig. 7), few irradiation parameters were calculated. First of all, an influence of incorrect axial positioning of the irradiation channel was checked. The results (Fig. 8) show, that even 10 mm difference can cause a rapid increase in the irradiation inhomogeneity. Thermal neutron distribution along the non-standard (shorter and thinner) ingots was also calculated (Fig. 9). For shorter ingots, thickness of axial graphite reflector was varied. For thinned ingots, an influence of additional material placed in the radial direction was investigated.

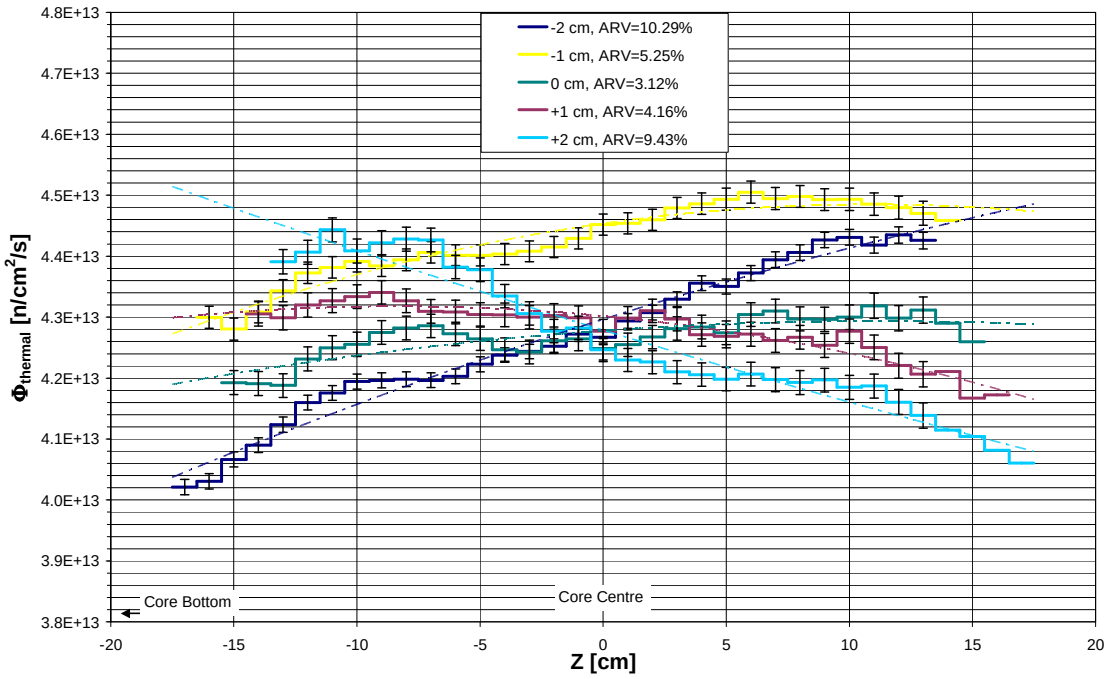

Fig. 8 Influence of axial positioning of the irradiation channel

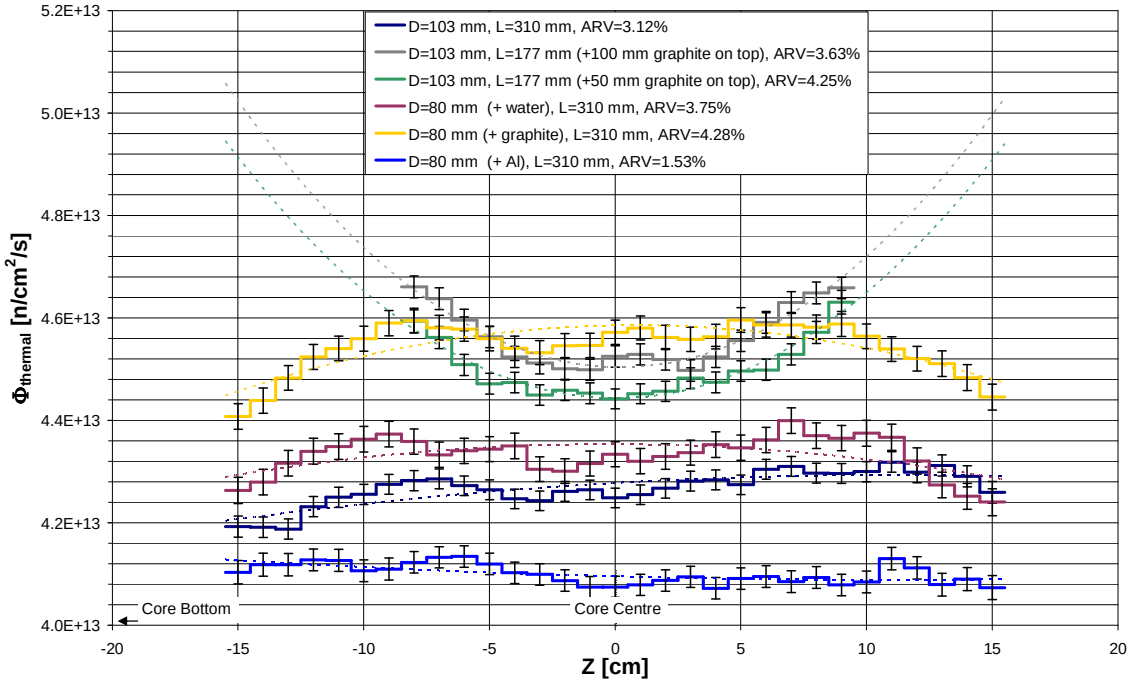

Fig. 9 Irradiation parameters for non-standard ingots

Conclusion

A new irradiation device for 4" silicon ingots was designed a fabricated. According to the presented calculations a new shielding layer was optimized for this device.

References

[1] Neutron transmutation doping of silicon at research reactors, *IAEA-TECDOC series*, ISSN 1011-4289, no. 1681, 2012.

Experimental and theoretical determination of neutron flux with 0.5NH1 helium chamber

M. Koleska, J. Rataj, A. Kolros, L. Sklenka
Department of Nuclear Reactors
Faculty of Nuclear Sciences and Physical Engineering, Czech Technical University in Prague
Brehova 7, 11519 Praha 1, Czech Republic

ABSTRACT

Measurement of the neutron flux with gas filled detectors is a basic technique used at zero power school-class reactors. Although these reactors are quite small, modeling of detector's influence to the neutron filed might be quite complicated. Therefore a simple "benchmarking" experiment with well known ^{241}Am-Be neutron source was performed. Experimental data were then used for development of MCNP model of the detector, which can be later used for calculation of reactor experiments. Several different approaches of modeling are discussed.

Measuring system

The increasing number of experiments performed on the school class reactor VR-1 raises demands for the measurement system used by these experiments. Within the last reconstruction of the reactor, several measurement tracks were prepared, so that the measuring equipment can be easily prepared to work. The heart of measuring lines is a PC controllable dosimetric device TEMA EMK 310. It can be connected (through the prepared measurement lines) to any of available gas filled and fission detectors.

For the experiment, the helium chamber Canberra 0.5NH1 was used. Its outer dimensions (10 mm diameter, 80,5 cm length) allow precise positioning of the active part of the detector in the neutron beam. Main parameters are in the Fig. 1. The basic properties were used to make the MCNP model of the detector.

Tab. 1 Characteristics of the detector 0.5NH1

Mechanical properties			**Operational characteristics**		
Length	80,5	mm	*Sensitivity*	0,5	$imp.s^{-1}/n.cm^{-2}.s^{-1}$
Diameter	10	mm	*Capacity*	3	pF
Wall material	Monel Ni-Cu (73-27)		*HV*	1600	V
Wall thickness	0,5	mm	*Plateau length*	100	V
Weigth	20,13	g	*Slope*	5	% na 100 V
Active part length	10	mm	*Noise*	0,3	μs
Gas	He3 + Kr		*Pulse rise*	0,6	μs
He pressure	8	bar	*Background*	30	$imp.h^{-1}$
Kr pressure	2	bar			

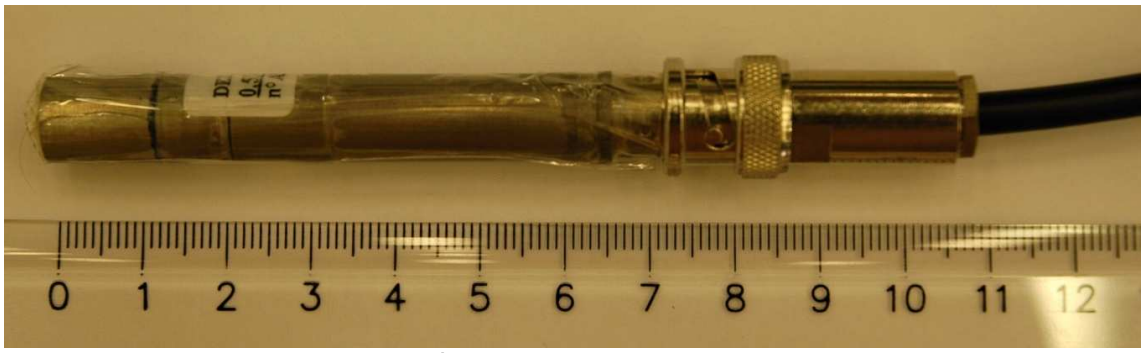

Fig. 1 Detector 0.5NH1

Adjustment of the measuring system

Basic characteristics of the detection system were estimated from the measurement with the C1 core. The measurement was performed with the detector in the B5 position and the reactor on power level 2.10^4 cps. The measured integral and differential characteristic of the detector were used for the adjustment the detector discrimination. The dead time of the system was determined by comparing the measurement (with reactor power level rising up to 2.10^6 cps) with the compensated ionization chamber CC54B with picoampermeter Keithley 6517A.

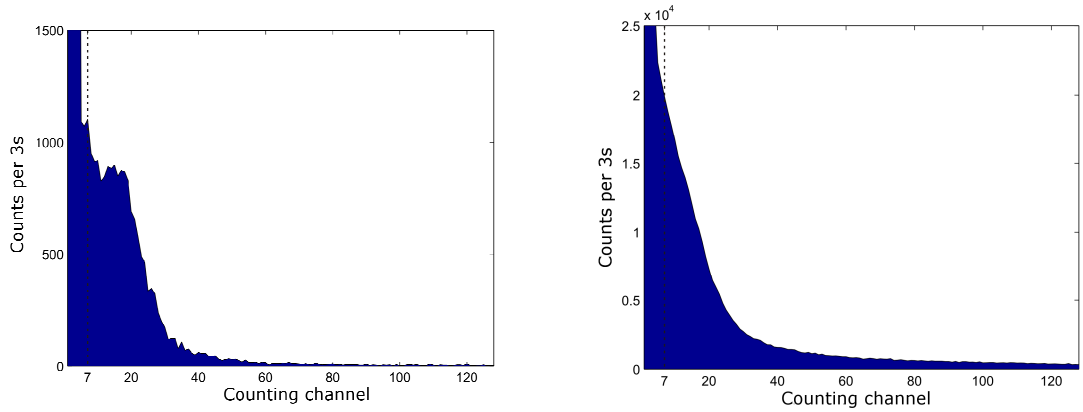

Fig. 2 Differential and integral characteristics of the 0.5NH1 detector

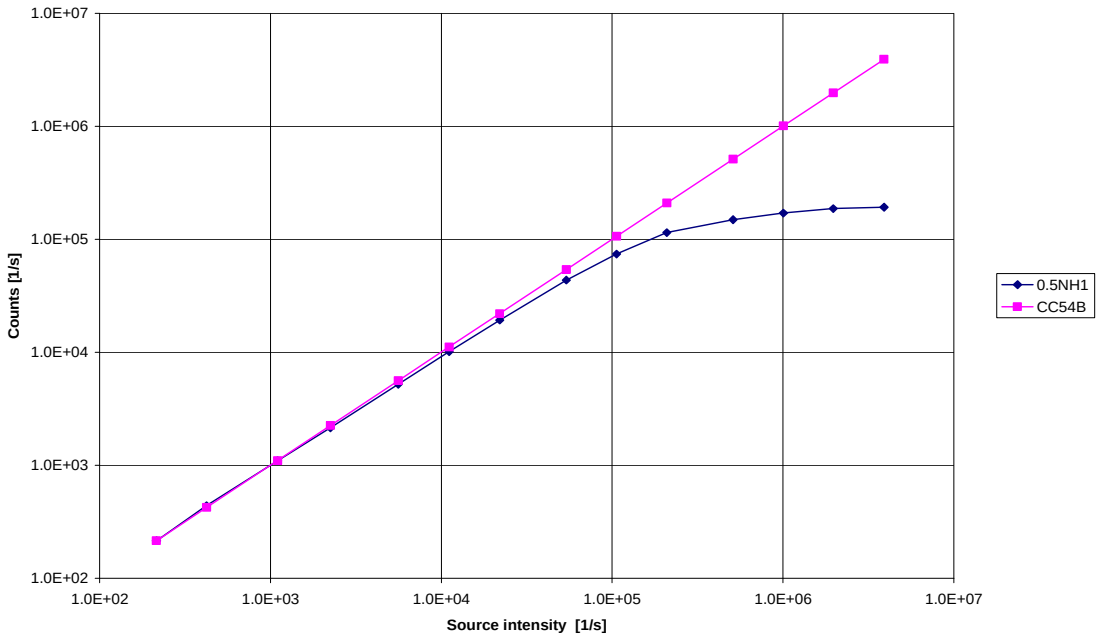

Fig. 3 Death time measurement

Experimental setup

The experimental data for verification of the MCNP model were measured in the reference setup using the neutron source. The purpose of the experiment was to verify the computation method in as simple geometry as possible. Such simplification avoids from uncertainties of the complex environment of the research reactor, so that the model accuracy and computational method can be evaluated.

The reference setup of neutron source and the detector was placed to the water tank (79 x 78,5 x 84,5 cm š x d x h) filled by the demineralized water. In the tank, an ^{241}Am - Be neutron source with the activity 185 GBq and emission rate 1,1.10^{7} n/s was used. The detector was placed to the dry channel (inner diameter 14 mm). This dry channel was mounted so that it could be relocated in the X-Y direction.

The measured data were compared to the MCNPX results for neutron flux distribution and reaction rate of the pure He^{3} gas filling and the mixture of He^{3} + Kr. The neutron spectra were calculated in WIMS 4 group neutron spectra interpretation, which is often used in reactor physics diffusion codes. The reaction rate of the detector gas filling was calculated for two volumes – the active part of the detector itself and for the whole inner space of the detector.

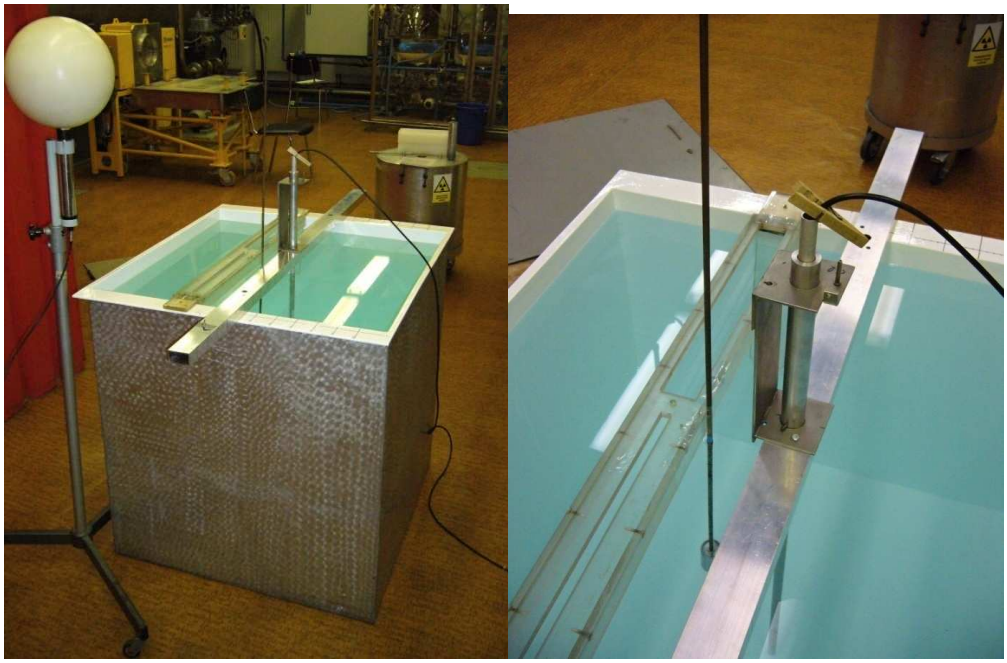

Fig. 4 Experimental setup

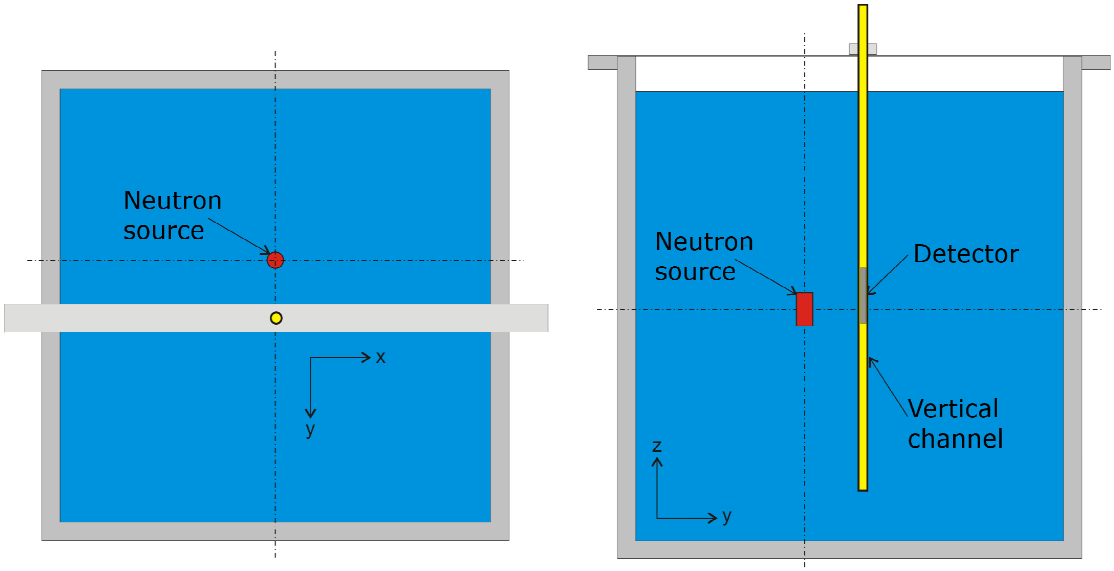

Fig. 5 Experimental setup

Results

Measured values are shown in the fig. Beginning with the distance of 19 cm from the source, the source can be estimated as a point source with the parabolic interpolation of the data. The X-Y distribution is in the fig.

Tab. 2 Measured data

Distance [cm]	Measured		$1/x^2$	
	$\bar{N}$ [imp./s]	$\bar{\varepsilon}$	$\bar{N}$ [imp./s]	C/E
4	15107	0,21%	6,15E+03	59,28%
9	7476	0,34%	4,00E+03	46,51%
14	2974	1,20%	2,32E+03	21,85%
19	1128	0,58%	1,13E+03	0,00%
24	410	0,79%	4,10E+02	0,01%
29	170	1,06%	1,70E+02	0,03%

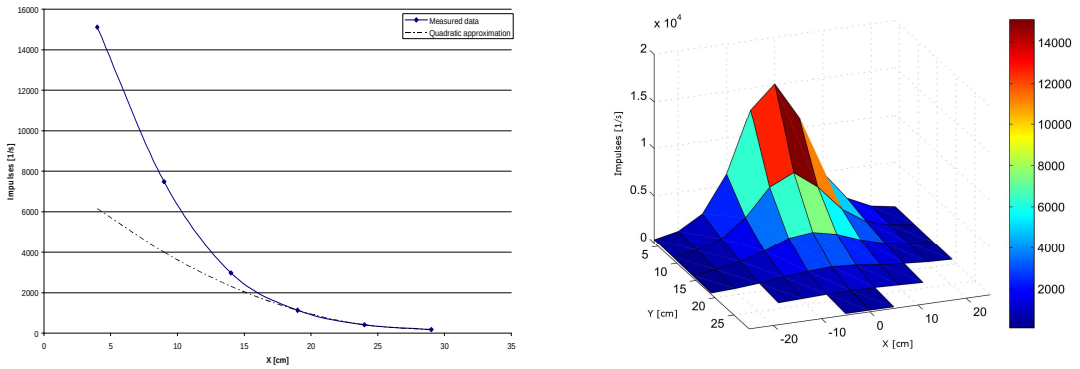

Fig. 6 Measured distribution

The comparison of measured data with WIMS energy groups shows, that the measured relative neutron distribution is corresponding to the thermal neutron group of the calculated spectra. Relative differences of the energy groups shows, that the detector has the biggest sensitivity for thermal neutrons (according to the He-3 cross section).

Calculated reaction rates show relatively good agreement with measured data. Practically no difference between He^3 and He^3 + Kr gas fill can be found due to the small amount of Kr in the mixture.

The comparison of the relative errors shows, that calculation of the neutron flux for thermal group only gives comparable result to the reaction rate calculation. For both types of data, a bigger discrepancy for the 4 cm position can be found. This discrepancy may be caused by the simplification of the neutron source, especially the source volume distribution. Another root of the discrepancy may be the mechanical interaction of the dry channel for the detector with the holder of the neutron source resulting in the fault in length measurement.

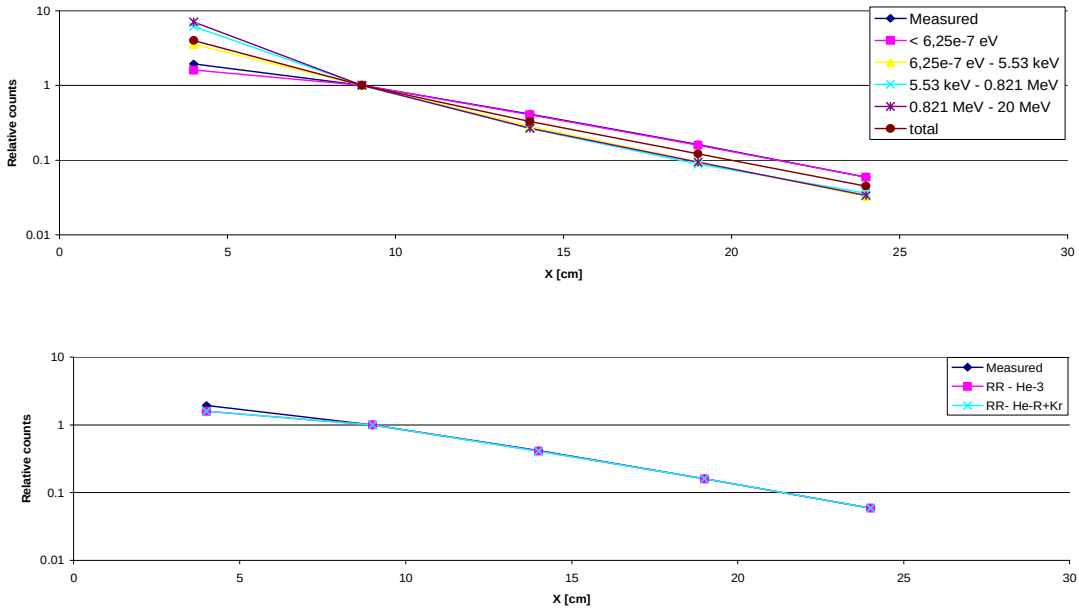

Fig. 7 Measured and calculated relative neutron distribution

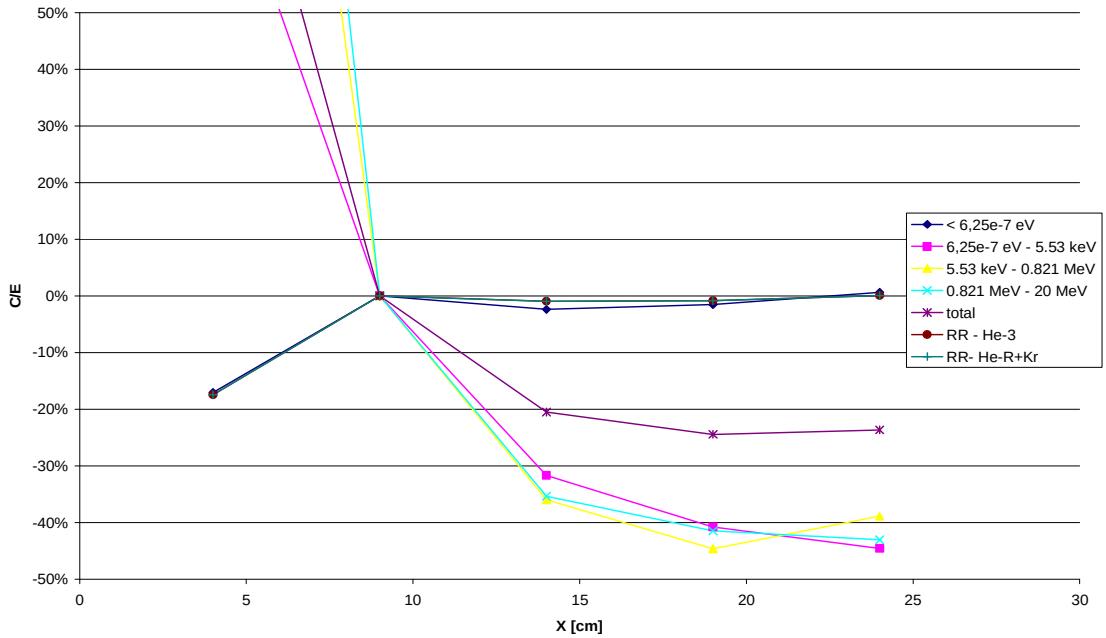

Fig. 8 Deviation of experimental from computational data

Conclusion

The experiment with the neutron source was performed to have experimental data for the verification of MCNP model of the detector. The measured response in such experiment could be affected by minimum uncertainties compared to research reactor. The comparison of the experiment with the calculation showed a good agreement, so that the detectors model and computational method can be used for the determination of neutron flux in complex geometries.

References

[1] Kolros, Antonín, et al. Reactor Physics Course at VR-1 Reactor. Praha : Department of Nuclear Reactors, CTU in Prague, 2008.

[2] D. B. Pelowitz, *MCNPX USER'S MANUAL* Version 2.7.0 - LA-CP-11-00438, Los Alamos National Laboratory, 2011.

TRIGA FUEL ELEMENT SIMULATION USING OPENFOAM

V.V.A. SILVA, A.A.C. SANTOS, P.S.B.L. DA SILVA, A.Z. MESQUITA
{vitors, aacs, psbls, amir}@cdtn.br
Serviço de Tecnologia de Reatores, CDTN/CNEN
Av. Antônio Carlos 6627, CEP 31270-901, Belo Horizonte, MG - Brazil

C.P.B. LIMA
claubia@nuclear.ufmg.br
Departamento de Engenharia Nuclear, UFMG
Av. Antônio Carlos 6627, CEP 31270-901, Belo Horizonte, MG - Brazil

ABSTRACT

Computational fluid dynamics (CFD) codes have been extensively used in engineering problems, with increasing use in nuclear engineering. One of these computer codes is OpenFOAM. It is freely distributed with source code and offers a great flexibility in simulating particular conditions like those found in many problems in nuclear reactor analysis. In order to simulate the IPR-R1 TRIGA Mark I reactor located at the Centro de Desenvolvimento da Tecnologia Nuclear, in Belo Horizonte, Brazil, it is important to accurately describe the fuel element thermal profile. Due to the particular cosinusoidal shape of TRIGA fuel power distribution, a specific boundary condition had to be implemented. Based in boundary conditions classes provided by OpenFOAM, a new class was developed taking in account not only the power profile of the TRIGA fuel but also implementing the heat transfer accurately. In this work the details of this implementation are presented with examples of use and results of a simple heat transfer case simulation.

1. Introduction

The TRIGA IPR-R1 Reactor is in operation since 1961 at the Centro de Desenvolvimento da Tecnologia Nuclear (CDTN). During this time, many data about its operation was collected. This valuable information provides a fundamental basis for any computer simulation, allowing the validation of the results obtained from computer codes. In order to simulate the TRIGA reactor operating under different conditions, the first step is to simulate it at a well experimentally investigated operating condition and compare the results with the experimental data collected at the same operation. However, many simulation aspects can make the results diverge from real data. To improve the accuracy of the simulation, it is obvious that the modelled reactor must behave as close as possible of its real counterpart.

The software used to perform the simulation is a free-distributed Computational Fluid Dynamics code called OpenFOAM [1]. OpenFOAM offers very flexible platform to perform fluid dynamics simulations. However, this flexibility does not come for free. To be able to change some very specific aspects of the simulation, the user must write its own code using the extensive set of classes provided by OpenFOAM [2].

That said, a key element in this case is the TRIGA fuel behavior. The cosinusoidal axial power distribution of TRIGA fuel is well known [3]. This work describes how this power

shape is achieved by means of the development of a new boundary condition class implementing the heat transfer from the TRIGA fuel to the coolant.

2. Development

The IPR-R1 TRIGA Reactor is filled with 63 fuel elements, 59 of them of aluminum cladding and 4 of stainless steel cladding. In the Figure 1 [3] there is a description of different characteristics of aluminum fuel. The stainless steel fuel is slightly different in size and with some changes in geometry, for example the spacer. However, at this point of the work, only the aluminum fuel is being modeled. Moreover, the main difference from both fuels, the thermal properties of the cladding, is not yet being modeled. This conjugate heat transfer simulation in envisaged in the future works.

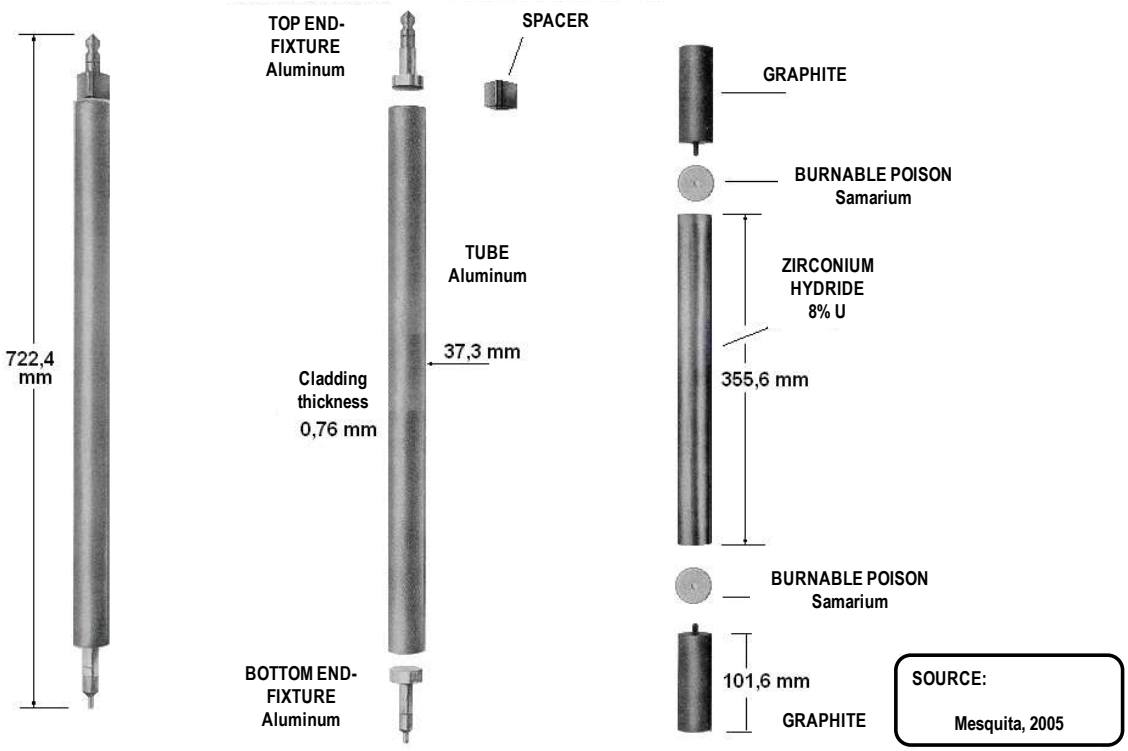

Figure 1 – Caracteristics os IPR-R1 aluminum fuel.

The focus in this work is to be able define a heat flux as similar as possible to the fuel. Its power distribution along the length of the fuel can be described as a cosinusoidal (or sinusoidal) function as shown in Figure 2.

The superior graph shown in Fig. 2 shows the power distribution along the active fuel surface L_0 and the ℓ on both extremities shows the extrapolation of flux which covers part of the non-active portion of graphite of the fuel. The second bar below the graph shows the real fuel rod and how should the power distribution match to it.

In the present case, an extreme simplification was done: the distribution is applied towards the fuel length and this distribution is then truncated to zero under both ℓ portions. It means that both areas in the boundaries have zero flux.

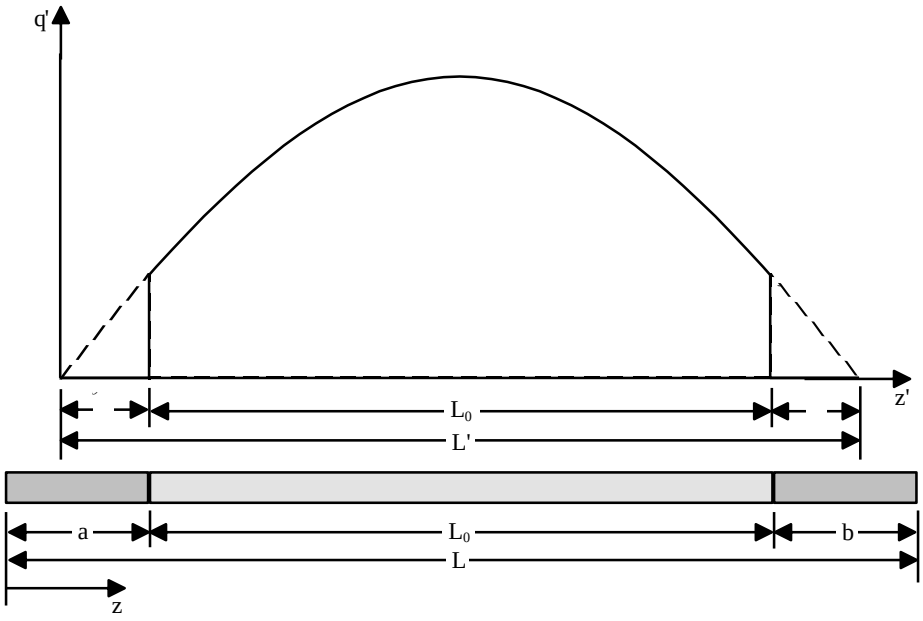

Figure 2 – Sinusoidal power distribution along the fuel element.

This coarse simplification introduces an error between the nominal power and the power really being applied. Analysis of this difference is performed in next sessions.

2.1 Implementation

The implementation is based in an already existent OpenFOAM's class: `turbulentHeatFluxTemperatureFvPatchScalarField`. This class implements a fixed heat boundary condition to specify temperature gradient. The input heat source can be either specified in terms of an absolute power [`W`] or as a flux [$\mathtt{W/m^2}$]. The key element in the new `TRIGAHeatFluxTemperature` boundary condition is the sinusoidal shape along the fuel and, in order to change this power shape, three main changes were made in the reference OpenFOAM class:

1) In the `TRIGAfvPatchField` constructor which takes a finite volume patch, a dimensioned field and a dictionary parameters. By taking all face centers in the fuel patch, the longest dimension (x, y or z) is taking after calculated the differences between the minimum and maximum points in Cartesian coordinates. Then, a new scalar field is created with the same size of the fuel patch. For all faces belonging to this patch the new correspondent face value is calculated and attributed to the face by means of the function:

$$face = q\_ \frac{\pi}{2} \sin\left(\frac{face_i - \min x}{x} \pi \right) \quad (1)$$

were, *face* is the scalar value at the face, $q\_$ is the constant gradient value given by the user, $face_i$ is the position of the face in the axis, $\min x$ the minimum coordinate value of the axis and x the axis size.

In the boundaries, the values are set to zero if the face position is approximately 7.74% of the total axis size. This is due to not having a heat flux gradient at the inactive parts of the fuel. Remembering this is not completely accurate since there are is a small heat flux gradient of entering the non-active part of the fuel (Figure 2).

In order to be able to attribute to the class gradient the values previously calculated and stored in a scalar field, a dynamic cast must be performed. The source code to perform this action is shown below:

```
scalarField& oPatch = dynamic_cast<scalarField&>(*this);
oPatch = (*patchField);
q_ = oPatch;
```

2) The second change is in the `TRIGAfvPatchField::updateCoeffs()` method. The specific water density (*rhow*) is read in the transport dictionary and added to the term in the denominator which calculates the surface gradient.

3) The values of specific water density (*rhow*) and specific heat capacity for the water (*Cp0*) were added to the RASProperties file in the simulation directory. These variables give the water properties necessary to the turbulence model and the boundary condition to calculate the heat flux.

2.2 Testing

Ideally, after modeling and/or simulating a problem it must be *verified* and *validated.* Validation consists in confirming if the values obtained are representative of the real world. Verification is to confirm if the model and numerical solution work according the proposed [5]. That said, the first step to test the boundary condition, is to simulate a simple case and verify the results. OpenFOAM setup for boundary conditions consists in defining them in files corresponding to each variable of the solver. Here are presented the boundary conditions for the temperature using the `TRIGAHeatFluxTemperature` boundary condition. In the file `T` in the simulation directory `0`, this boundary condition is applied to patches representing the fuel wall, or, in other words, the wall where the heat flux will be defined.

```
boundaryField
{
  fuel_c4
    {
        type TRIGAheatFluxTemperature;
        heatSource power;
        q uniform 1000.0;
        alphaEff kappaEff;
        Cp Cp0;
        value uniform 300;
    }
  ...
```

The first line shows that this is the set of boundary fields to be defined. The `fuel_c4` is the name of the patch and after it the patch details. The type is the boundary condition to be used, than the source characteristics, the power field in [`W`], the name of turbulent thermal diffusivity field, the specific heat capacity variable and the default value for the temperature field. Details on how to use this boundary condition are in comments in the source code.

The basic test to guarantee the correct behavior of the `TRIGAHeatFluxTemperature` is verifying the energy and mass balancing in a simulation. This test was performed in a geometry modeling a sub-channel of the TRIGA IPR-R1 reactor showed in Figure 3.

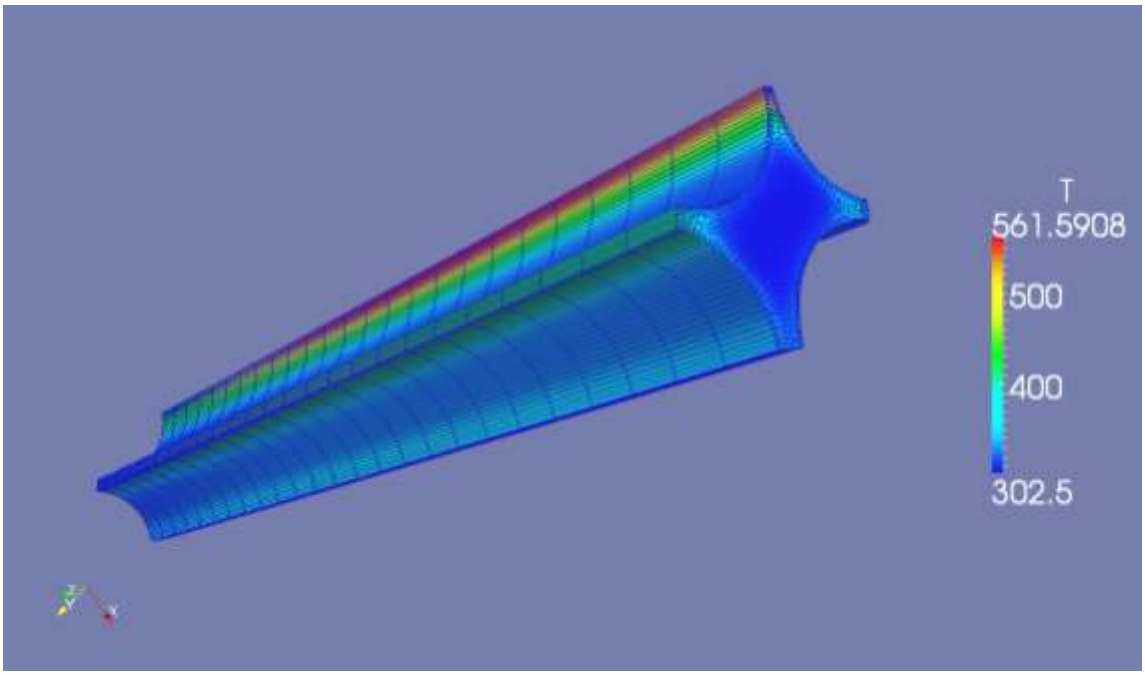

Figure 3 – Modelled subchannel of TRIGA IPR-R1 reactor.

The variation of the mass flow averaged value of temperature of the water flow entering and leaving the subchannel was used to verify if the energy added to the system. In order to be able to apply it, the system must have reached the steady-state. In short, the system must respect the conservation of energy [6]. This is verified by means of the equation:

$$T_{outlet} = \frac{q}{vA\rho Cp} - T_{inlet} \tag{2}$$

Were the temperature at the outlet [T_{outlet}] must be equal to the heat transferred [q] over fluid velocity [v] times flow area [A], times fluid density [ρ] times fluid specific heat [Cp] minus the temperature at the inlet [T_{inlet}].

The results for the simulation shown in Figure 3 are presented in Table 1.

Table 1 – Results for the energy conservation of the modelled system.

Theoretical values	
Ro	997,2
Cp	4178
Velocity	0,09
T inlet	302,5
Power	4000
theoretical DT	18,968

Simulated data	
Mean T outlet	320,597
A	0,0005624
DT	18,097
m	0,05
final m	0,05
Q	3816,31

Difference	
ΔQ%	4,59
ΔT%	4,59

The difference from theoretical calculations to the simulation for the heat transferred is about 4.59%. This loss is due to the oversimplification in the power profile implementation for the fuel extremities.

3. Results

The new boundary condition was tested using the `buoyantBoussinesqPimpleFoam` solver. This is a transient solver for buoyant, turbulent flow of incompressible fluids. The mesh represents the core of IPR-R1 TRIGA reactor, with differences among graphite rods, control rods, fuel and neutron source. The scheme of reactor core is presented in Figure 4.

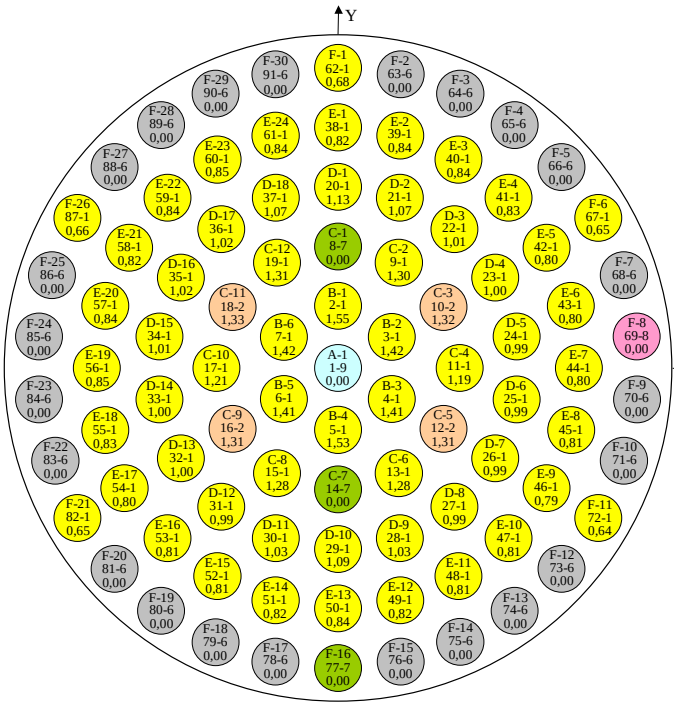

Figure 4 – Element distribution of TRIGA IPR-R1 reactor.

The values in each rod shown in Figure 4 are, in top-bottom order: annulus-position identification, core number-type of fuel (1 aluminum – 2 stainless steel) and the radial power factor. The radial power factor was obtained from former calculations [2] and is not considered in the test simulations.

In order to verify the natural convection, the inlet velocity for water in the core was set initially to zero and 250kW of power was defined for the whole core.

It is important to remark that there is no simulation of conjugate heat transfer. Due to this fact, a surface heat flux was defined at the fuel elements, neglecting heat conduction effects. This allows the temperature to reach values which are not the same as the real reactor. Moreover, due to the characteristics of the solver, there is no water boiling. The solver is limited to one phase.

The left side of Figure 5 shows the set of fuel rods and the power profile due to the heat flux provided by the `TRIGAHeatFluxTemperature` and in the right side, an upper view from the mesh used in the core simulation. The thin fluid connections separating fuel rods can be seen in yellow and green, showing the highest fluid temperatures in these areas.

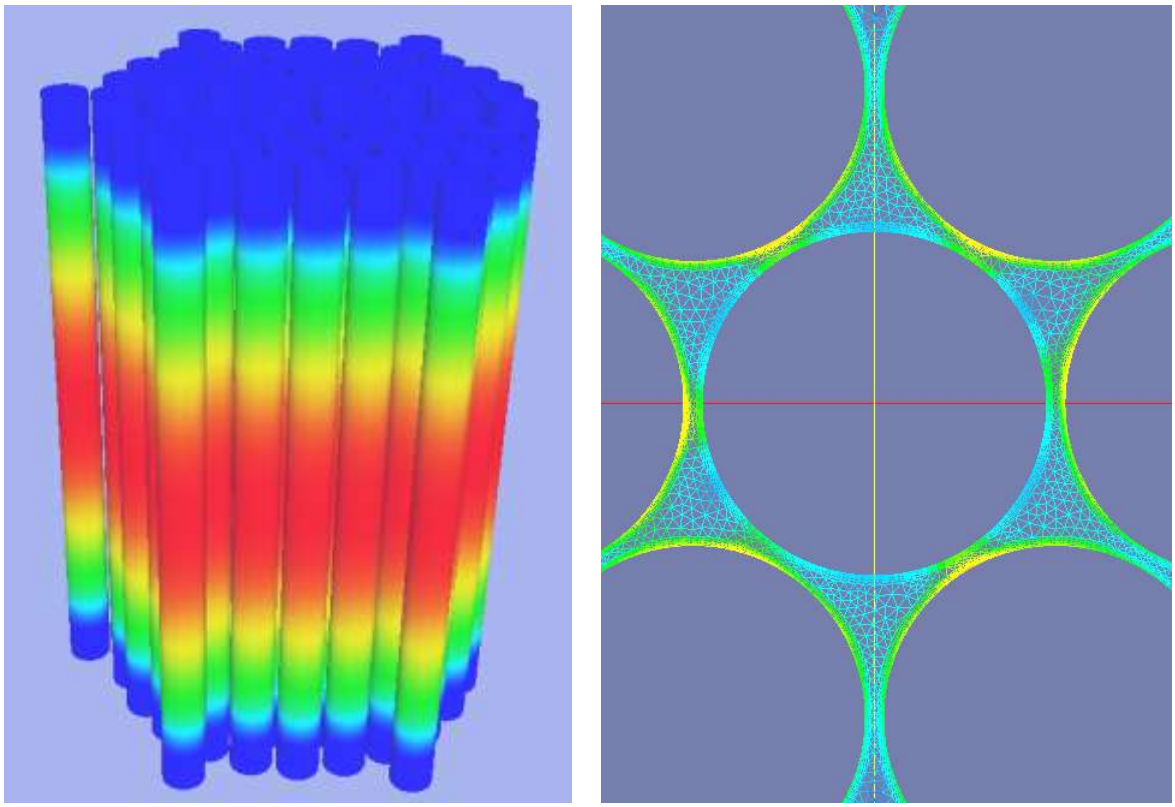

Figure 5 – Simulation power profile (Left side) and top view of the used mesh (right side). The colors show, from blue to red, the the incresing flux from fuel extremities to center.

A screenshot from the full core simulation is show in Figure 6. In this image, the simulation is still is course and the steady-state was not yet reached. The temperatures are in Kelvin.

For all simulations, the mass-energy balance was applied to assure the calculations are mathematically correct.

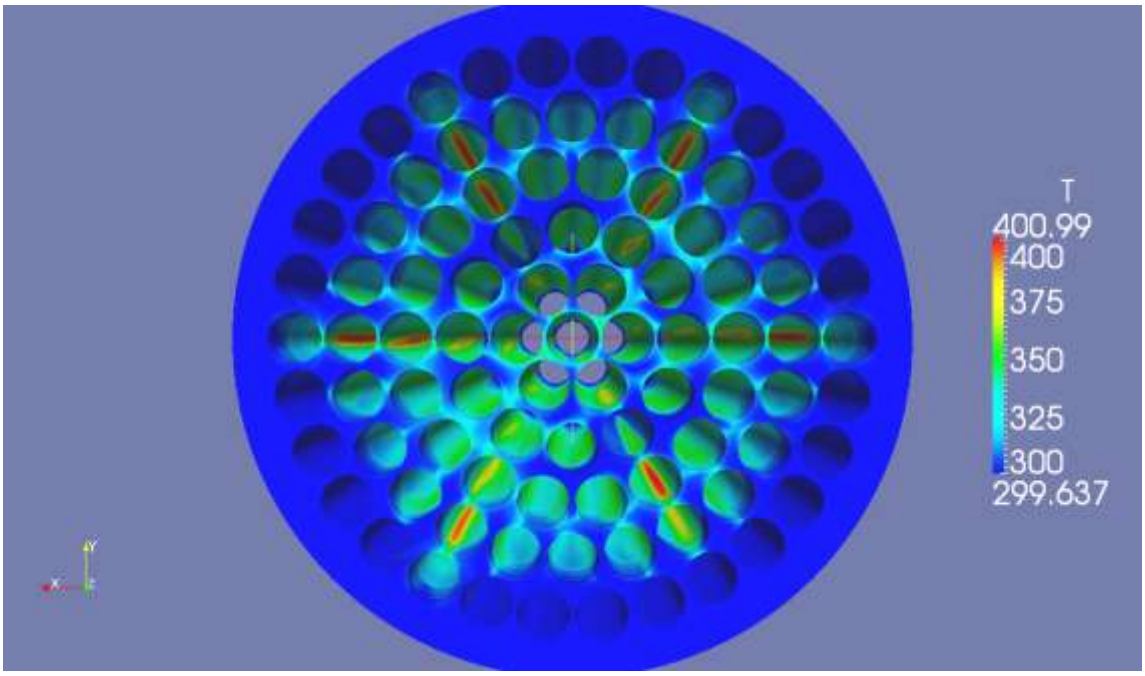

Figure 6 – Temperature distribution of water flowing through TRIGA IPR-R1 core.

4. Conclusion

The new `TRIGAHeatFluxTemperature` boundary condition is fully functional and provides a heat flux in sinusoidal shape like the TRIGA fuel with only 4.6% error to the nominal power. Simulations in a sub-channel configuration and the full core were carried. However, since there is no conjugate heat transfer implementation and sub-cooled boiling, the water in the simulated core can reach much higher temperatures than in the IPR-R1 TRIGA.

5. Future work

A simulation with a different solver (namely chtMultiRegion) is envisaged in order to fully simulate the TRIGA IPR-R1 core and sub-channels. The simulation will consider the material compositions in the fuel: cladding (Al 1100-F), fuel ($U\text{-}ZrH_{1,0}$) and graphite. The results of this simulation will be compared to the experimental data collected during reactor's operation in different powers.

This implementation is also a first approach to boundary conditions implementation in OpenFOAM. A next step is to implement more detailed heat flux considering a simplified neutronics modeling of the fuel.

6. Aknowledgments

The authors would like to thank AIEA for the grant to attend the Conference and the Department of Nuclear Engineering and Engineering School of UFMG for paying RRFM 2013 conference registration fees.

7. References

[1] JASAK, H., JEMCOV, A. and TUKOVIC, Z. **OpenFOAM: A C++ Library for Complex Physics Simulations** International Workshop on Coupled Methods in Numerical Dynamics, 2007.

[2] **OpenFOAM C++ Documentation.** *openfoam.org***.** n.p. 2013. Mars 21, 2013.

[3] VELOSO, M. A. **Avaliação Termo-Hidráulica do reator TRIGA IPR-R1 a 250kW.** CDTN/CNEN, Belo Horizonte, 2005 (NI-EC3-05/05).

[4] MESQUITA, A. Z. **Investigação experimental da distribuição de temperaturas no reator nuclear de pesquisa TRIGA IPR-R1**. Tese de doutorado apresentada à Faculdade de Engenharia Química da Universidade Estadual de Campinas", Campinas, SP, 2005.

[5] JANOSY, J. S. **Simulation and Simulators for Nuclear Power Generation**, Nuclear Power - System Simulations and Operation, Dr. Pavel Tsvetkov (Ed.), ISBN: 978-953-307-506-8, InTech, DOI: 10.5772/18219. 2011. Available from: http://www.intechopen.com/books/nuclear-power-system-simulations-and-operation/simulation-and-simulators-for-nuclear-power-generation

[6] WARK, K. Jr. and RICHARDS, D. E. **Thermodynamics**. Sixth Edition. WCB/McGraw-Hill, 1999.

BENCHMARK CRITICALITY EXPERIMENTS FOR URANIUM-WATER HETEROGENEOUS CONFIGURATIONS WITH UZrCN LOW ENRICHED NUCLEAR FUEL

S. SIKORIN, S. MANDZIK, S. POLAZAU, T. HRYHAROVICH,
Y.DAMARAD, Y. PALAHINA
The Joint Institute for Power and Nuclear Research – Sosny of the National Academy of Sciences of Belarus, 99 Acad. Krasin str., Minsk 220109, Belarus

ABSTRACT

The Joint Institute for Power and Nuclear Research – Sosny of the National Academy of Sciences of Belarus performed criticality experimental investigation for uranium-water heterogeneous configurations with $U_{0,9}Zr_{0,1}C_xN_{1-x}$ low-enriched uranium (LEU) nuclear fuel for including in the international handbook of evaluation criticality safety benchmark experiments. LEU fresh fuel was design and produced for critical facility "Giacint" under RRRFR Program of research reactors nuclear fuel conversion. LEU fuel consists of uranium-zirconium carbon nitride $U_{0,9}Zr_{0,1}C_xN_{1-x}$ tablets with 19.75% enrichment by U-235. Density of a fuel composition is not less than 12 g/cm^3, porosity less than 12%, density of uranium more than 10.5 g/cm^3, and the diameter of a tablet 10.7 mm. The total length of the fuel rod is 620 mm, the length of the uranium fuel part of rod is 500 mm, and the diameter of the fuel rod is 12 mm. The cladding material of fuel rods is stainless steel or niobium. The authors developed of detailed analytical models for calculation of the experimental criticality configuration using the MCNP and MCU computer codes. In this paper, the analytical model details, the experimental results and comparison of analytical and experimental investigation are presented.

1. Introduction

Experiments with uranium-water critical assemblies with fuel rods containing uranium-zirconium carbon nitride $U_{0,9}Zr_{0,1}C_xN_{1-x}$ with 19.75% enrichment by U-235 were performed through the research program [1,2] of the Joint Institute for Power and Nuclear Research – Sosny of the National Academy of Sciences of Belarus (JIPNR – Sosny, NAS of Belarus) at the critical facility "Giacint". The critical assembly was a homogeneous hexagonal grid of fuel rods, 32 mm pitch, with a water moderator and a reflector.

2. Description of the experimental configuration
2.1 Location of the critical assembly

The critical assembly is located in the room of the critical facility "Giacint" (Fig. 1). It represents an open-tank critical assembly and comprises a core, a side reflector, upper and lower end reflectors and actuating elements (AEs) of the control and protection system (CPS).

The critical assembly tank is installed on a support frame in the middle of the room in the form of a parallelepiped, 7.4x7.4x8.5 m, at -0.9 m elevation. The room's lower elevation is -3.00 m, and its ceiling is at +5.50 m elevation. A slab from 4-mm metal sheets was arranged at 0.00 m and +3.00 m elevations. The room's concrete walls have different thicknesses, 1.5, 1.0, 1.2 and 1.0 m, the floor is from 0.2 m thick concrete, and the ceiling is from 0,5 m reinforced concrete.

2.2 The critical assembly tank and related elements

The critical assembly with water moderator is located directly in the tank, which represents a welded stainless-steel structure 2020 mm high and the inner diameter of 1810 mm. The tank has a 6-mm thick cylindrical lip and a 17-mm thick flat bottom. On top, the tank has a 17-mm flange to fix aluminium hoods of neutron detectors.

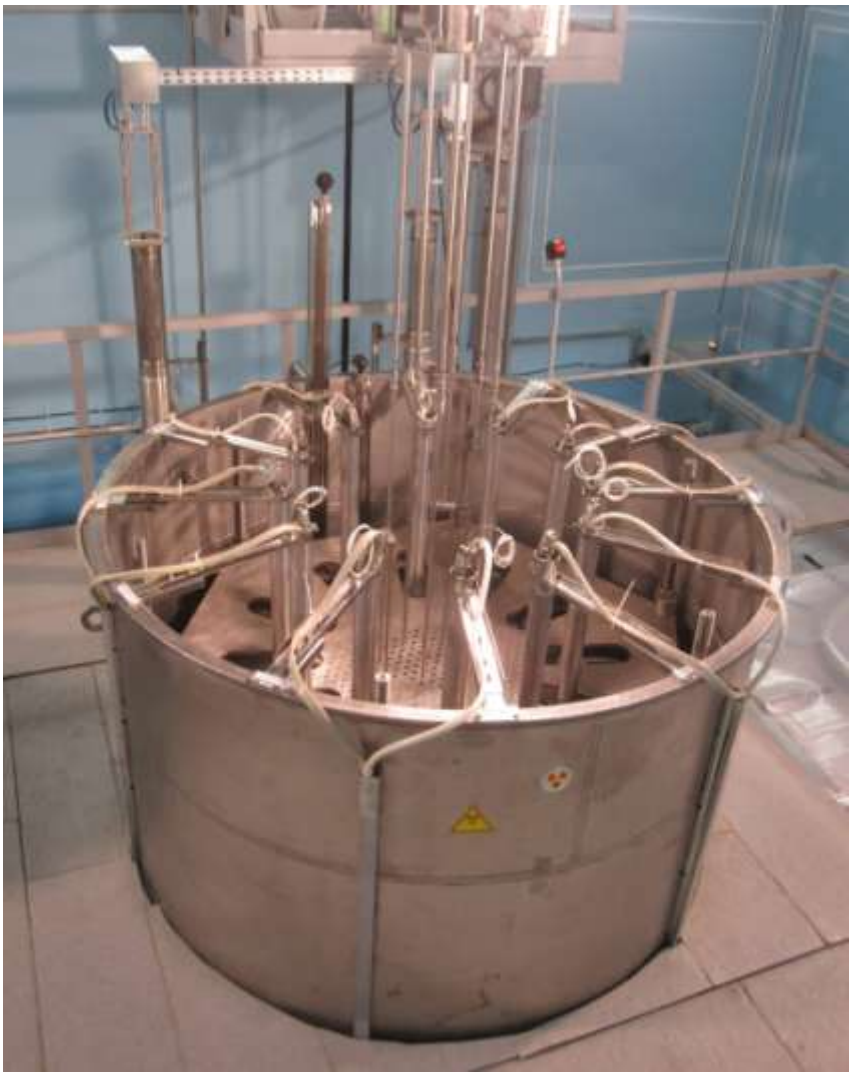

Fig 1. General view of the critical assembly

The core of the critical assembly consists from of fuel rods fixed inside hexagonal spacer grids from aluminium alloy and installed on a hexagonal stainless-steel supporting plate. A hexagonal upper stainless-steel plate is installed above the fuel rods.

The spacer grids, the upper and the support plates are put onto six 38-mm steel pins connected to the tank bottom by threaded joints. The distances between the plates are set by steel tubes that are also put onto pins. Nuts ate screwed onto the pins to fix the entire structure inside the tank rigidly.

The side water reflector houses neutron detector hoods, arranged around the core; the hoods are attached to the critical assembly tank flange by holding devices.

The spacer grids are arranged on the upper and lower edges of the core. The support plate is located ~800 mm from the tank bottom.

2.3 The plates and spacer grids

The stainless-steel supporting plate is a hexagon with the 880 mm side and 16 mm thickness and holes for CPS AEs. The lower and upper spacer grids from aluminium alloy are hexagons with the 880 mm side and the 10 mm thickness with 12.4 dia. holes, arranged on the hexagonal grid with the 32 mm pitch. The upper plate from stainless-steel is a hexagon with the 880 mm side and 16 mm thickness with 13 dia. holes, arranged on the hexagonal grid with the 32 mm pitch.

2.4 The control and protection system's actuating elements

The CPS AE structure allowed making experiments only with "clean" grids of fuel rods, i.e., the core includes only fuel rods and moderator. The CPS includes two emergency protection (EP) AEs, two manual regulation (MR) AEs, and two compensating (CO) AEs.

The EP1, EP2 and CO1 actuating elements are in the core and represent singular composite rod elements comprising two parts: the lower part with the fuel rod and the upper part with the absorbing element (AbsE). The MR1, MR2 and CO2 actuating elements are located in the side reflector and represent a cluster from two composite rod elements, comprising, in turn, two parts: the lower part which is 10-mm dia. rod from Plexiglas, and the upper part, containing the AbsE. The structure of all CPS AEs is such that when they are lifted (withdrawn), the core becomes homogeneous and the side reflector also becomes practically homogeneous.

The AbsE is cylindrical stainless-steel cladding with the 12 mm diameter and the 1 mm thick wall with the upper and lower 60-mm long shanks, also made from stainless steel, filled with boron carbide, ~1,3 g/cm^3, to the 500 mm height. The total AbsE length is 620 mm.

2.5 Neutron detectors

The CPS neutron detectors are located inside tight aluminium cups with the 1230 mm length and the 60x3 mm diameter, in a special Plexiglas hood with the 600 mm length and the 100 mm diameter. The cups are fixed to the tank's upper flange. The neutron detectors and their fixing elements are located at a distance of more than 250 mm from the core edge, having no impact of its critical dimensions. The CPS includes three neutron counters CHM-18 and six ionization chambers KHK-56. Similarly, three ionization chambers KHK17-1 are arranged around the core for experiments.

2.6 Reflectors

The upper end reflector of critical assemblies comprises the upper fuel rod shanks, the upper spacer grid, the upper plate and the water reflector. The lower end reflector of critical assemblies comprises the lower fuel rod shanks, the lower spacer grid, the support plate and the water reflector ~800 mm thick. The side water reflector has the length over 250 mm. Thus, the side and lower water reflectors can be considered to be physically infinite.

2.7 Fuel rods

The fuel rod comprises a fuel core, a cladding and end parts (Fig. 2). The fuel rod cladding is from stainless steel with the 12 mm outer diameter and the 0.6 mm thickness. The fuel core comprises tablets of the 10.7 mm diameter and ~14 mm height, made from uranium-zirconium carbon nitride $U_{0,9}Zr_{0,1}C_xN_{1-x}$ (carbonitride fuel has been synthesized in the second

half of 80s the last century [3]). The core density is 12.0 g/cm^3, the porosity is not more than 12%, the uranium capacity is ~10,5 gU/cm^3, and the enrichment by U-235 is 19.75%. The gaps between the fuel core tablets and the fuel rod cladding have gaseous He under ~0.11 MPs. The total core height is 500 mm. The total fuel rod length is 620 mm. The fuel rod is tightly sealed. The sealing is ensured by welding the upper and lower plugs to the cladding. The fuel rods were developed and fabricated by the FSUE "SRI SIA "LUCH" of the State Atomic Energy Corporation ROSATOM by the technical order form the JIPNR – Sosny of the NAS of Belarus [4].

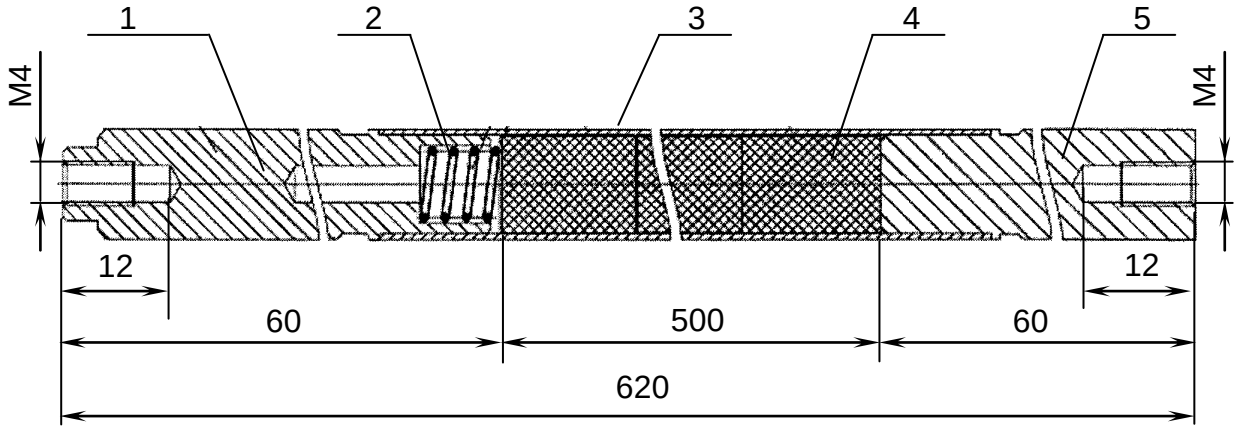

Fig 2. The fuel rod:
1 – lower shank; 2 – spring; 3 – clad; 4 – fuel core;
5 – upper shank

3. Results of experimental and calculation research

Two critical assemblies with the 32 mm pitch of the fuel rod hexagonal grid were studied. Their characteristics (with CPS AEs withdrawn) are given in Table 1. The loading charts are given in Figs. 3 and 4, and the calculation model of the critical assemblies is Fig. 5. The calculated effective neutron multiplication factor for these critical assemblies, obtained by MCNP-4A [5], MCNP-4C [6] and MCU-RFFI [7], are given in Table 2.

The critical assembly number	The number of fuel rods, pcs.	Reactivity margin, β_{eff}	Moderator level*, mm	Moderator temperature, °C
1	66	0	531.8	16.5
1	66	0.14	750.0**	16.5
2	67	0	497.1	15.7
2	67	0.58	750.0**	15.7

* The moderator level was counted from the core's lower edge.
** See Fig. 5.

Tab 1. The experimental characteristics of the critical assemblies

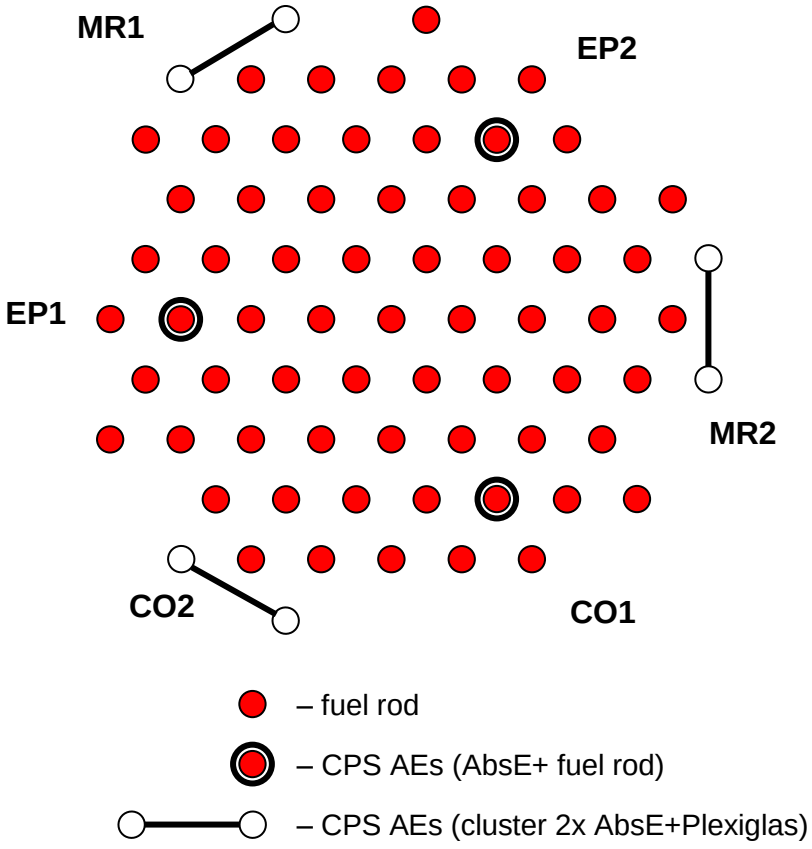

Fig 3. Loading chart of critical assembly 1

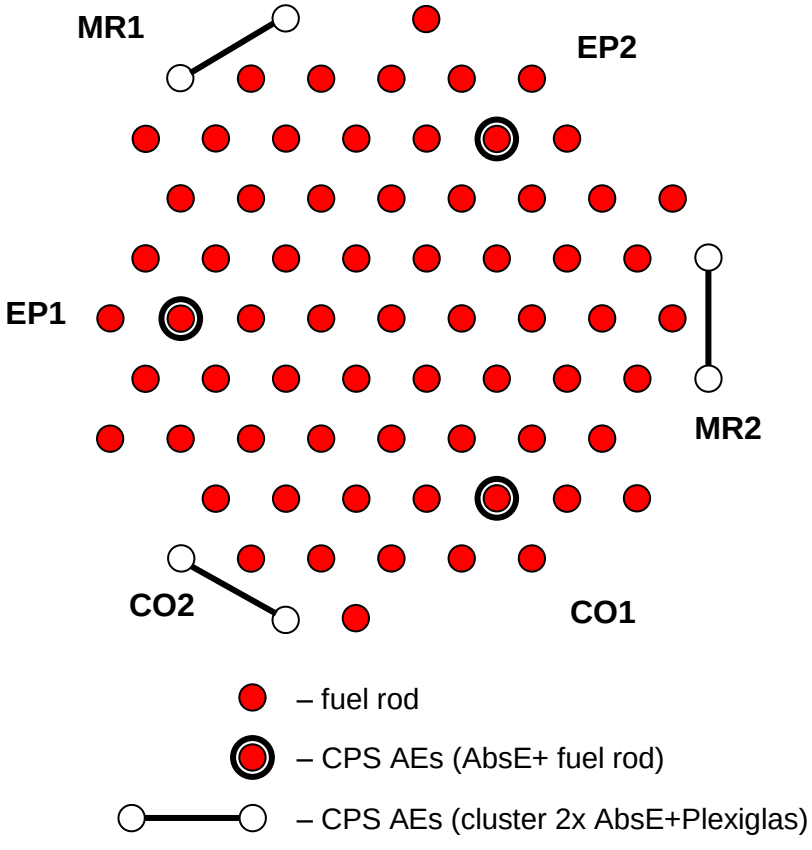

Fig 4. Loading chart of critical assembly 2

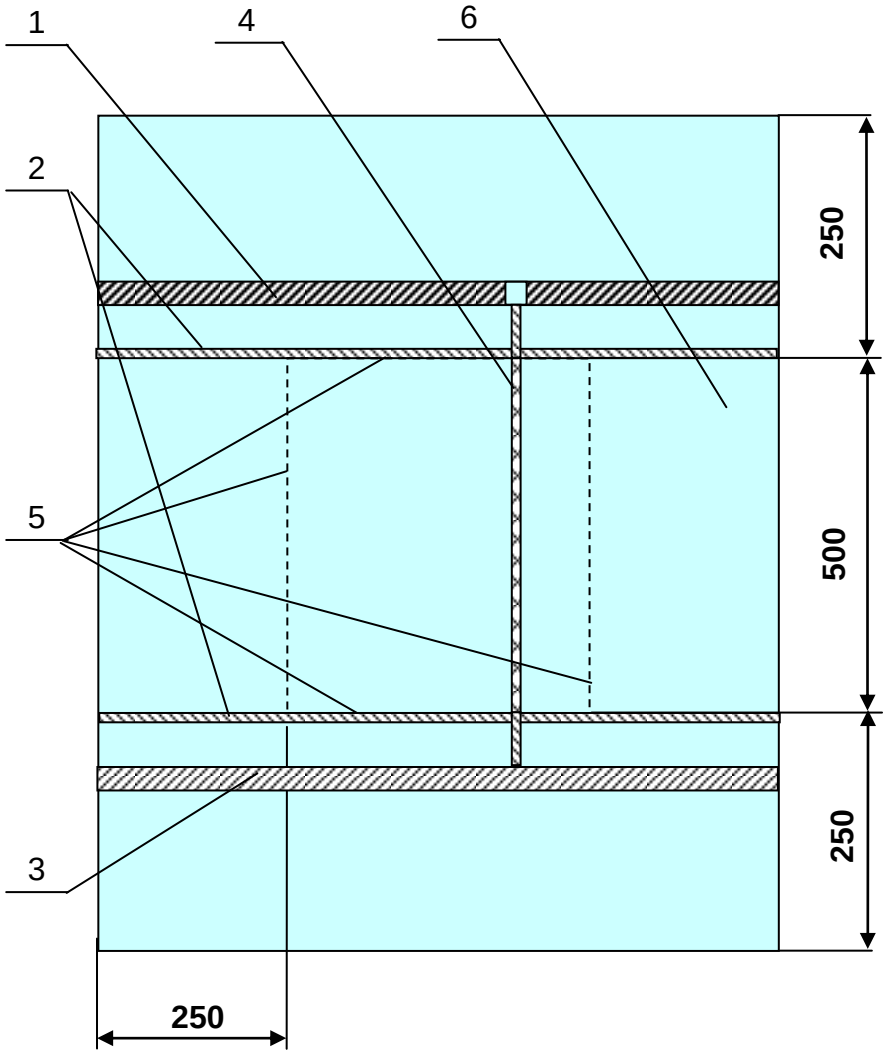

Fig 5. Calculated model of the critical assembly
(for versions with physically infinite upper end water reflector):
1 – upper plate; 2 – spacer grids; 3 – support plate; 4 – fuel elements; 5 – core boundaries;
6 – distilled water

The critical assembly number	The number of fuel rods, pcs.	Moderator level*, mm	Calculation program (library of constants)			
			MCNP-4A (ENDL-85, ENDF/B-V)	MCNP-4C (ENDF/B-V)	MCNP-4C (ENDF/B-VI)	MCU-RFFI
1	66	531,8	1,0019(4)	0,9993(4)	0,9966(4)	—
1	66	750,0	1,0032(4)	1,0009(4)	0,9980(4)	—
2	67	497,1	1,0028(4)	1,0004(4)	0,9976(4)	0,9991(7)
2	67	750,0	1,0059(4)	1,0041(4)	1,0015(4)	1,0050(9)

Note. β_{eff}=0.0082 calculated by MCU-RFFI.

Tab 2. Calculated effective neutron multiplication factor K_{eff} of critical assemblies

4. Conclusions

The experimental results obtained for uranium-water critical assemblies with fuel rods containing uranium-zirconium carbonitride with 19.75 % enrichment by U-235, arranged with the 32 mm pitch in homogeneous hexagonal grids, can be used as benchmarks criticality data.

Experiments on uranium-water critical assemblies with other pitches of the said fuel rods in homogeneous hexagonal grids are conducted now.

5. References

1. Sikorin S., Mandzik S. Utilization of LEU Nuclear Fuel on Critical Facility “GIACINT” / Regional Workshop on Russian Research Reactor Fuel Return Program - Lessons Learned, Jackson, Wyoming, USA, 7-10 June 2011. – Vienna: IAEA, 2011. – CD.
2. Sikorin S., Mandzik S., Polazau S., Hryharovich T. The Program of Experiments at the Critical Assembly "Giacint" using LEU Nuclear Fuel on the basis of UZrCN / 34th International Meeting on Reduced Enrichment for Research and Test Reactors (RERTR-2012), Warsaw, Poland, 14-17 October 2012. Book of Abstracts: Warsaw, 2012.
3. Dyakov E., Blank V. Uranium Carbonitride Compounds – Fuel for Promising Compact Nuclear Reactors / Proceeding of Space Nuclear Conference 2007, Boston, Massachusetts, 24-28 June 2007.
4. Alekseev S., Dyakov E., Hryharovich T., Kuvshinov V., Sikorin S., Tukhvatulin Sh., Past and New Nuclear Fuels for Gas Cooled Small Size Reactors of Mobile Nuclear Power Plants/ Technical Meeting on Fuel and Fuel Cycle Options for Small and Medium Size Reactors, IAEA, Vienna, Austria, 12-14 October 2011. – CD.
5. MCNP — 4A General Monte Carlo N-Particle Transport Code, Version 4A / Ed. J.F.Briesmeister. – Los Alamos, 1993. — 701 p. — (Report / LNL; LA-12625-M).
6. MCNP^{TM}-A General Monte Carlo N-Particle Transport Code, Version 4C / Ed. J.F. Briesmeister. Los Alamos, 2000. (Report / LNL; LA-13709-M).
7. Application and User Manual for MCU-RFFI on Monte-Carlo Calculation of Physical Neutron Characteristics of Nuclear Reactors / E.A. Gomin, et al., Moscow, 1994. 63 p. (Preprint / IAE-5837/5).

CONCEPT OF THE RESEARCH REACTOR FOR THE REPUBLIC OF BELARUS

S.N. SIKORIN, V.I. KUVSHINOV, V.T. KAZAZYAN, T.K. HRYHAROVICH
The Joint Institute for Power and Nuclear Research – Sosny of the National Academy of Sciences of Belarus, 99 Acad. Krasin str., Minsk 220109, Belarus

A.A. MIKHALEVICH, A.P. AKHRAMOVICH, V.P.KOLOS
The Institute of Power of the National Academy of Sciences of Belarus, 15/2 Akademicheskaya str., Minsk 220072, Belarus

ABSTRACT

In 1962, the research site of the Joint Institute for Power and Nuclear Research – Sosny of the National Academy of Sciences of Belarus was used to put into operation the research reactor IRT-2000, with 2 MW thermal power, which was later upgraded as IRT-M, bringing its thermal power to 5 MW. The IRT-M reactor was shut down in 1988, and decommissioned in the late 1990's. Currently, the Republic of Belarus started the building of an NPP with VVER-1200 reactors. The Republic of Belarus also plans to have its own research reactor for different usage. The National program of the development of the nuclear power sector in the Republic of Belarus specifies the technical requirements and justifies the need of construction of a new research reactor in the Republic of Belarus, in order to solve a broad range of scientific and applied problems in fundamental physics, radiation material science, production of medical and industrial isotopes, safety of reactors, reactor technologies, neutron activation analysis, medical and biological application, etc. This reactor can also be used for various educational programs. The previous investigations showed that the 10-20 MW pool-type research reactor with low-enriched nuclear fuel (less than 20% by uranium-235) and forced circulation of the research reactor water coolant is the most suitable version of the research reactor for the Republic of Belarus. This report shows the lines of use of, and the basic technical requirements to the new research reactor for the Republic of Belarus.

1. INTRODUCTION

A number of countries have recently demonstrated their interest in new research reactors to develop nuclear technologies of various usages. The Republic of Belarus also has such interest.

In 1962, the research reactor IRT-2000 (Fig. 1) was put into operation at the Joint Institute of Power and Nuclear Research–Sosny (JIPNR-Sosny) of the National Academy of Science of Belarus. This reactor was updated in 1976 and the thermal power increased to 5 MW (this version was called IRT-M). In 1988 the IRT-M reactor was shut down and then decommissioned in the late 1990's.

Fig 1. The research reactor IRT-M

The mentioned reactor was used for multiple researches, primarily in nuclear power generation. In particular, it was used to create a loop installation GPU-100P with the nitrine coolant (N_2O_4+NO), which was used to study both encapsulated samples of structural materials and fuel compositions and the design of fuel elements and fuel assemblies, as well as the impact of temperature, pressure, neutron and gamma radiation on the nitrine coolant physical and chemical properties, etc. (the entire range of problems related to the development of the mobile NPP “Pamir-630D”).

Besides, this research reactor was used to conduct scientific research in various domains (solid-body physics and semiconductors, geology, medicine, radiation chemistry, etc.); in particular, it was used to create a loop installation KYU-5 for studying radiation and chemical processes affected by fission fragments (generation of hydrazine from ammonia).

It was planned to substitute the decommissioned reactor IRT-M and to build in the Republic of Belarus a new research reactor; however, this plan was not implemented after the disintegration of the Soviet Union.

2. Lines of use and basic technical specifications of the research reactor

In 2012, the National Academy of Science of Belarus sent to the relevant stakeholder ministries and departments of the Republic of Belarus (the ministries of energy, industry, health, education, emergency, agriculture and food, and other ministries) a request about the expediency of building and the lines of use of a new research reactor in the country; this was done within the State Program “Scientific Support of Development of Nuclear Power in the Republic of Belarus for 2009-2010 and for the period up to 2020”.

The said ministries and departments showed their interest in the construction of a new research reactor in the Republic of Belarus to be used for solution of various scientific and applied problems in nuclear physics, energy, technology, medicine and education.

The basic lines of use of the new research reactor in the Republic of Belarus are as follows:

- material studies of different coolant in the reactor core cells and loop channels in conditions of intensive neutron and gamma radiation;
- testing of advanced fuel elements, absorbing elements and other core elements in steady-state and transitional operation modes for operated and innovative reactors;
- testing new types of equipment, various technological systems, devices and systems of control, monitoring and diagnosis of power reactors;
- studying radiation suitability of materials, components, devices and equipment used in technologies, in particular in reactor and outer space technologies;
- studying radiation modification of material structures to produce new physical and chemical properties and develop advanced technologies;
- applied problems (development of medical and industrial isotopes, nuclear silicon alloying, neutron activation analysis, use of horizontal beams inside the reactor vessel for neutron radiography and medicine, sterilization, preservation, extension of storage period and decontamination of foods and fodder, animal materials (wool, hide, fur, etc.) biological and pharmacological preparations (vaccines, sera, agars, vitamins, etc.), surgical suture and dressing materials, devices and tools that cannot be treated by temperature or chemicals, etc.);
- education and training of nuclear power specialists in cooperation with universities or other technical education institutions.

In choosing the design of a new research reactor, the following specific features of nuclear research reactors should be taken into consideration:

- high frequency of transitional operation modes (start-up, shutdown, variation of power in a broad range, dynamic experiments);

- frequency overloads in the core and constant movement of radiated items (for study, to storage pools, for long-term storage, for disposal, etc.);
- highly cyclic loads on the main equipment in the core and the first loop due to a high number of short campaigns;
- high density of the neutron flux in the research reactor cores, leading to a rapid reaching of the ultimate fluence on the core elements;
- the problem of non-proliferation of nuclear materials, requiring efficient systems for their account and physical protection;
- the use of experimental devices and associated operational features, etc.

Analysis of the national economic needs of the Republic of Belarus and advanced developments in research reactors across the world has been used to define the basic technical specifications of the research reactor planned for construction in the Republic of Belarus (Table 1).

No	Parameters	Values
1.	Reactor type	pool reactor
2.	Thermal power, MW	10-20
3.	Maximum thermal neutron flux (E <0.625 eV), $\times 10^{14}$ $cm^{-2} \cdot s^{-1}$: - in core - in beryllium reflector	 3-4 1.5-2
4.	Neutron flux at horizontal hole outlets, $\times 10^{10}$ $cm^{-2} \cdot s^{-1}$: - thermal neutrons (E <0.625 eV) - fast neutrons (E > 0.82 MeV)	 0.8-1.3 0.01-0.05
5.	Fuel composition	UO_2/Al, UMo/Al
6.	Fuel enrichment by U^{235}, %	less than 20
7.	Coolant	H_2O
8.	Reflector	Be, H_2O
9.	Number of horizontal experimental holes	not less than 4
10.	Number of vertical experimental holes	up to 25
11.	Reactivity temperature effect	negative
12.	Average fuel burn-up in withdrawn fuel assembly, %	not less than 50

Tab 1: The basic technical specifications of the research reactor planned for construction in the Republic of Belarus

The research reactor must be placed in a protective concrete building and include a steel tank representing the outer shell of the pool, a core, a beryllium reflector, the control and protection system (CPS) actuating, ionization chamber channels, an upper shielding plate, horizontal holes gates and experimental devices. The reactor's pool design makes it much easier for fuel assemblies and irradiated samples to be placed in and withdrawn from the core.

On the basis of a new research reactor can be created the centre of nuclear researches which will perform the tasks on the above-named directions taking into account requirement of concrete users, including within the limits of the international cooperation.

3. Planned use of the research reactor for development of the cores with micro fuel elements

For a long time, the JIPNR-Sosny has developed small-size nuclear reactors of different uses and locations, as well as high-flux research reactors with the core based on small-size ball fuel elements (micro fuel elements) [1-4]. The research on such reactors can be continued in cooperation with other countries using the new nuclear research reactor.

A qualitative step in increasing the power density in the nuclear reactor cores can be made only by using a new type of nuclear fuel. The IAEA-recommended reduction of uranium enrichment below 20% by ^{235}U for non-proliferation purposes makes reaching high neutron flux a problem.

An obvious solution of this problem may be an increase of the heat-release surface by using fine dispersed fuels (micro fuel elements) with direct cooling. It is needed to ensure a rational distribution of the coolant in the fuel layer in order to organize a proper heat removal with allowed pressure drops. However, it turned out that this problem is not a simple one, requiring a thorough investigation of the hydrodynamics and heat exchange in the filled micro fuel elements.

Today, the most promising and well-developed design is a radial fuel assembly (Fig. 2), combining the advantages of fine fuel and radial pumping of the coolant. Such fuel assembly can bring the energy intensity of the cores up to 10 MW/dm^3, thereby, ensuring the neutron flux density up to 10^{16} neutrons/(cm^2·s).

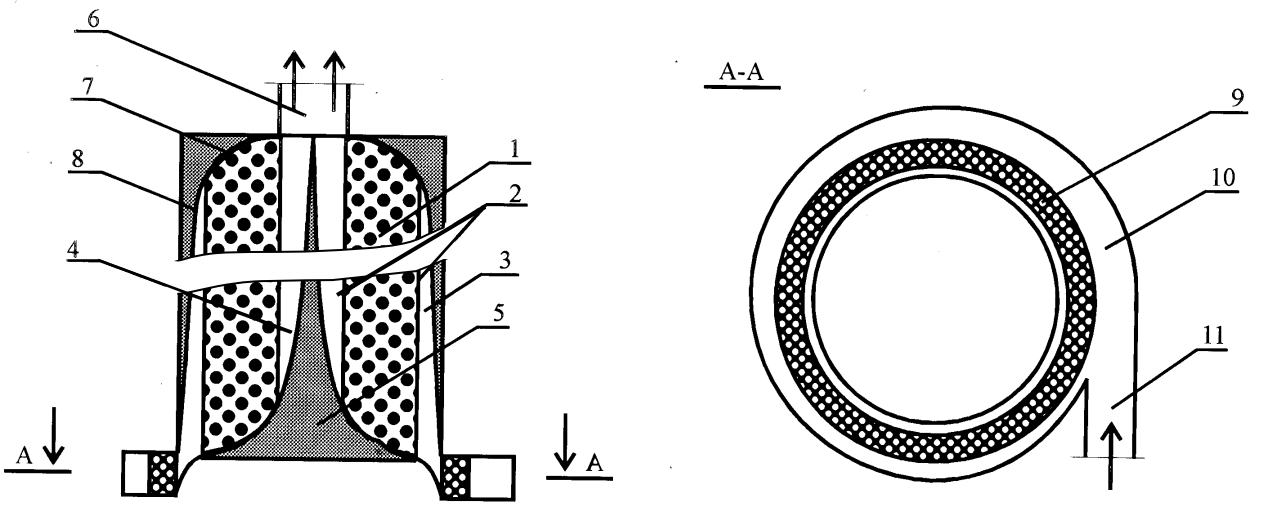

Fig 2: 1 – micro fuel elements layer; 2 – protecting grid layer; 3 – distribution channel; 4 - shaped offtake channel; 5 – displacement rod; 6 – output union; 7 – end wall; 8 – lip; 9 – porous ring partition; 10 – snail channel; 11– entrance to the snail channel

A comprehensive analysis of thermal hydrodynamics of such devices made it possible to identify their basic design features, thus allowing substantially higher energy intensity in the fuel layer. It turned out that reliable and stable operation of such reactors is possible only with specific relations of the structural fuel assembly elements and their shapes. Otherwise, we will observe a ball swirling in the drainage duct and an oscillating vortex in the distribution channel, and stalemate area at the ends of the fuel layer hindering the coolant distribution and deteriorating heat removal radically.

Correct conclusions were made due to the obtained dynamic match of the flux. The overwhelming majority of researchers build their calculations on the obvious conclusion, i.e., the pressure loss in the coolant in the fuel assembly includes the pressure loss in all elements of the hydraulic pathway. However, such approach is not good for calculating radial devices. Here, a more versatile concept is needed, based on dynamic match that reflects the flux of the coolant with the varying mass. This condition radically influenced the approach to the organization of heat removal in devices with radial coolant flow in the fuel layer. For a substantial increase of the energy intensity, it is required to achieve a similarity between the mass rate of filtration and energy release in the fuel assembly, ensured by special profiles of the channels. It allowed a degree of freedom that made it possible to state and solve

optimization problems. One of such problems was the problem of finding the dimensions and shapes of structural elements in radial fuel assembly, ensuring maximum possible energy intensity in the fuel layer. The solution of this problem helps finding the shapes of the channels and end walls of the fuel layer, facilitating intact flow of the coolant and preventing stalemate areas, the characteristics of artificial roughness made on the channel walls for tabulation of the flow in order to ensure similarity between the mass filtration rate and the linear energy release in a broad range of versions of the fuel element flow through the fuel assembly.

In a new research reactor planned to create a loop channel for experimental research of fuel rods with micro fuel elements.

4. Development of research reactors in the Russian Federation, meeting the needs of the Republic of Belarus

In conditions of the Republic of Belarus, the most suitable are the developments of the State Atomic Energy Corporation “Rosatom” (JSC “NIKIET”, JSC “VNIINM”, JSC “NZHK”, etc.) and NRC “Kurchatov Institute”, pool-type research reactors with water coolant of 10-20 MW thermal power and low-enriched (19.7% by ^{235}U) nuclear fuel [5].

These are pool-type reactors with forced water coolant circulation through the core. Demineralized water is used as coolant, moderator, end reflector, and radiation protection. Beryllium is used as side reflector.

Pool-type reactors have a long history of safe and efficient operation. Such reactors also allow high densities of thermal neutron flux sufficient for practically all types of research using thermal neutrons.

It is planned to use in the newly developed research reactors the currently mass-produced fuel based on low-enriched uranium (19.7% by ^{235}U): fuel assembly IRT-4M and VVR-KN [6-8]. Also, the currently developed new low-enriched high-density dispersed U-Mo fuel can be used [6,7].

Such type of the research reactor can be considered for development and construction in the Republic of Belarus.

5. Conclusions

Analysis of the modern state of research reactors in the world has demonstrated that any country planning the construction of a NPP or operating a NPP, as a rule, has a nuclear research reactor. Today, a number of states entire build or plan to build new research reactors. In the developing countries, research reactors are the first step in the national programme of nuclear power.

Based on the interests of national economy of the Republic of Belarus, the basic lines of use of the new research reactor have been identified and the basic requirements to such reactor have been developed.

The Russian Federation has developed technical proposals on advanced pool-type research reactors with water coolant and the 10-20 MW thermal power on the core, based on fuel assemblies with low-enriched nuclear fuel. Such type of the research reactor can be considered for the construction in the Republic of Belarus.

6. References

1. Ananich P.I., Kazazyan V.T., and Sikorin S.N. Prospects of using Reactors with Small-Diameter Ball Fuel Elements in Outer Space Nuclear Power Engines / 5th International

Conference “Nuclear Power in Outer Space”, Podolsk, Russia, 23-25 March 1999. – Proceedings, Part 1. – Podolsk, 1999. – P.131-141.

2. Ananich P.I., Akhramovich A.P., Kazazyan V.T., Kolos, V.P., Mikhalevich A.A., Sikorin S.N., Tetereva N.A. “Possibility of Creating Low-Power Reactors with the Core Using Ball Fuel Elements”, Atomic Energy, Vol. 97, Issue 3, 2004. – P.168 – 172.

3. Ananich P.I., Kazazyan V.T., Kuvshinov V.I., Sikorin S.N. Akhramovich A.P., Kolos, V.P., and Mikhalevich A.A. Concept of Research Reactors with Ball-Type Micro Fuel Elements **/** Reports of II International Conference “Nuclear Technologies of the 21st Centur”, Minsk, Republic of Belarus, 6-8 October 2010. – Minsk, 2010. – P. 151-158.

4. Sikorin S., Ananich P., Kazazyan V. Possibility of the Design of a High-Flux Pebble-Bed Research Reactor with Small Fuel Spheres / Research Reactors: Safe Management and Effective Utilization Proceedings of an International Conference, Rabat, Morocco, 14-18 November 2011. – Vienna: IAEA, 2012. – CD-ROM.

5. Osipovich S.V., Kuatbekov R.P., Lukichev V.A., Sokolov S.A., Tretiyakov I.T., Trushkin V.I. New Generation of Research Reactors Fuelled with LEU / Research Reactors: Safe Management and Effective Utilization Proceedings of the International Conference, Rabat, Morocco, 14-18 November 2011. – Vienna: IAEA, 2012. – CD-ROM.

6. Lavrenyuk P.I., Krylov D.V., Cherepnin Yu.S., Lukichev V.A., Vatulin A., Dobricova I. Reduction of Fuel Enrichment in Research Reactors: Progress and Prospects / Russian–American Symposium on Conversion of Research Reactors from Highly Enriched Uranium Fuel to Low-Enriched Uranium Fuel, Moscow, Russian, 8-10 June 2011.

7. Kuatbekov R.P., Cherepnin Y.U., Lukichev V.A., Vatulin A., Dobricova I, Krylov D. Reduced Enrichment for Research Reactors: Status and Prospects / Research Reactors: Safe Management and Effective Utilization Proceedings of the International Conference, Rabat, Morocco, 14-18 November 2011. – Vienna: IAEA, 2012. – CD-ROM.

8. Enin A. LEU Fuel for Research Reactors of the Russian Design / Regional Workshop on Russian Research Reactor Fuel Return Programme Lessons Learned, Tihany, Hungary, 12-15 June 2012. – CD.

EXPERIMENTAL MEASUREMENTS OF VOLUME, PRESSURE AND COMPOSITION OF GASES INSIDE SWELLING BUBBLES OF IRRADIATED FUEL ELEMENTS CONTAINING U-Mo/Al DISPERSION FUEL

O.A. Golosov, V.N. Nikolkin, M.S. Lyutikova, V.V. Bedin, A.A. Dyakov
Institute of Nuclear Materials
624250, Zarechny, Sverdlovsk region, Russia, 624250

ABSTRACT

One of the stages that precedes a damage of fuel elements of research reactors with dispersion U–Mo/Al fuel is the phase of a formation of swelling bubbles on fuel claddings and an accumulation of gas fission products (GFP) in the fuel elements. It is impossible to substantiate a safety operation of a fuel element with a dispersion U–Mo/Al fuel without an understanding of a GFP behavior under such conditions.
The results of the experimental determination of a free volume of swelling bubble, volume, composition and pressure of GFP in them are given in this paper.

1. Introduction

A safety operation of high-flux research reactors with a dispersion U-Mo/Al fuel is determined by a performance capability of fuel elements, whose life time depends on an ability of a fuel composition to retain fuel fission products and strength properties of a cladding material. One of the phases that precedes a fuel damage is a formation of cladding swelling bubbles due to a fission products release from fuel particles to under the fuel cladding with gas cavities formed. Data to characterize a condition of fission products in such cavities are practically not available in literature.

2. Materials and Methods

The object of this research is a fuel element with a dispersion U-Mo/Al fuel in a combined fuel element assembly designated "KM004" that had been irradiated to an average burn up of ~80 % in the IVV-2M reactor [1]. The fuel element under study had one cladding swelling bubble of a diameter ~25 mm and height ~1.1 mm.

Manometer measurements before and after a punch of a fuel cladding on the swelling bubble were made to determine a free volume of the swelling bubble, a total volume and a pressure of gases inside the swelling bubble. A special device (Fig. 1.*a*) was designed for making measurements and sampling the gases.

The device includes two calibrated vessels V1 and V2 of volumes V_1 and V_2, respectively, ~2.2 cm^3 each (at the same time being sampling apparatuses # 1 and # 2, respectively), a technological route V0 (its volume V_0 is ~1.8 cm^3), cut-off valves designated B0, B1 and B2, pressure gauges PG1 (absolute) and PG2 (differential) manufactured by Motorolla. In Figure 1.*b* the schematic diagram of the swelling bubble of an unknown volume V_x and unknown gas pressure P_x is shown.

The manometer measurements (made ~600 days after irradiation tests) were conducted as a sequence of stepwise operations.

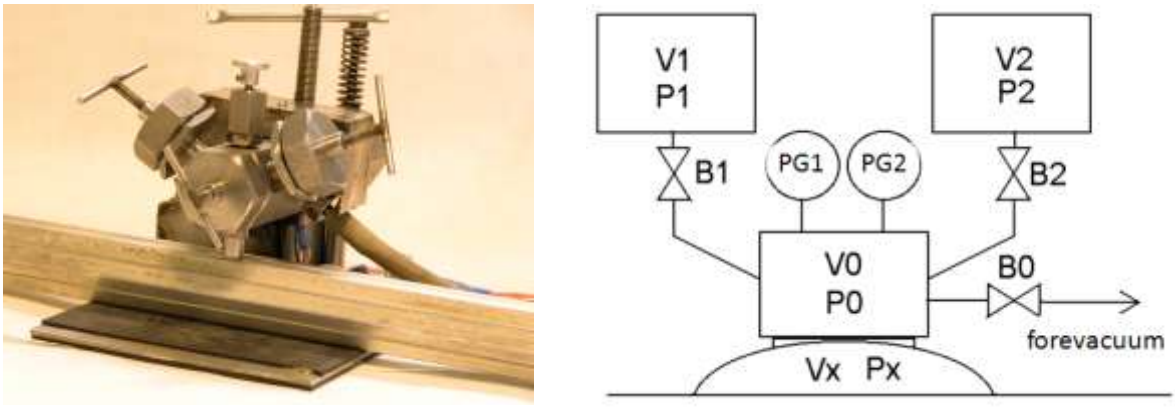

A b

Figure 1. An appearance (*a*) and schematic diagram (*b*) of the device to punch a swelling bubble on a fuel cladding

1st step. Press a punching unit against a fuel cladding. Open valves B0, B1 and B2. Evacuate sampling apparatuses V1 and V2 and technological route V0 and determine an initial pressure P00.

2nd step. Close valves B0, B1 and B2. Punch a fuel cladding and determine a fuel element pressure P0 in a total volume V_x+V_0. For this condition of the system under study, the following equation is true

$$P_xV_x = P_0(V_x + V_0) \quad (1)$$

3rd step. Open valve B1 and determine pressure P1 in a total volume $V_x+V_0+V_1$. Close valve B1. In this case for the system under study the following equation is true

$$P_0(V_x + V_0) = P_1(V_x+V_0+V_1) \quad (2)$$

4th step. Open valve B2 and determine pressure P2 in a total volume $V_x+V_0+V_2$. Close valve B2. For this condition of the system under study the following equation is true

$$P_1(V_x + V_0) = P_2(V_x+V_0+V_2) \quad (3)$$

5th step. Open valve B0 and pump the gas from the device's technological cavity of volume V0 and from a volume of swelling bubble into evacuated sampling apparatus # 3.

The free volume V_x and the gas pressure P_x inside the swelling bubble were determined by solving a system of equations (1)-(3).

The activity of radionuclides, chemical and isotopic composition of gas samples preserved in sampling apparatuses ## 1, 2 and 3 was determined by the methods of gamma– and mass–spectrometry.

3. Results and discussion

A gas pressure inside the fuel element was measured while punching through the fuel element in a place of swelling bubble, the manometer measurement results are given in Table 1.

According to data in Table 1, the average value of the swelling bubble free volume V_x= 0.54 cm^3 and that of the gas pressure inside the swelling bubble P_x=643 kPa. Taking into account that the manometer measurements are made at 23 ^oC (the temperature of ambient air of a hot cell), and by normalizing to normal conditions (T=273 K) the value of P_x will be 594 kPa and the gas volume inside the swelling bubble will be ~3.18 cm^3.

Table 1. Results of manometer measurements while punching fuel element cladding

Step #		Pressure, kPa	V_x, cm^3	P_x, kPa
1	P00	5.8	-	-
2	P0	142.5	0.55	635
3	P1	76.1	0.54	647
4	P2	38.9	-	649
		Average value:	0.54	643

A radioactivity of gas is mainly determined by the activity of gamma–emitting radionuclides ^{85}Kr and ^{137}Cs with total activities $A_{Kr\text{-}85}$=~$1.12\cdot10^9$ Bq and $A_{Cs\text{-}137}$=$1.42\cdot10^4$ Bq, respectively, at the moment of making measurements.

According to the mass-spectrometric analysis data obtained the gas inside the fuel element is the mixture of isotopes of xenon and krypton with a ratio equal to 8.33 (Tab.2).

Table 2. Isotopic content of gas

Isotope	Content, % (vol.)
^{83}Kr	11.20
^{84}Kr	25.49
^{85}Kr	7.32
^{86}Kr	55.98
^{131}Xe	8.61
^{132}Xe	16.02
^{134}Xe	27.95
^{136}Xe	47.42
^{83}Kr+^{84}Kr+^{85}Kr+^{86}Kr	10.73
^{131}Xe+^{132}Xe+^{134}Xe+^{136}Xe	89.27
∑Xe /∑Kr	8.33

The data in Tables 1 and 2 permit to estimate a volume of Xe-Kr mixture in the free volume of the swelling bubble and compare it with a quantity of GFP, that can form in the fuel meat of the fuel element with sizes of the swelling bubble under study during the period of fuel assembly testing.

The volume of the Xe-Kr mixture in the в free volume of the swelling bubble can be determined from the expression

$$V_{\Sigma(Kr+Xe)} = \frac{V_{Kr-85}}{\upsilon_{Kr-85}} + \frac{V_{Kr-85}}{\upsilon_{Kr-85}\cdot\beta_{\Sigma Xe/\Sigma Kr}}, \quad (4)$$

where $V_{\sum(Kr+Xe)}$ – the total volume of Xe-Kr mixture in the swelling bubble volume, cm^3;
$V_{Kr\text{-}85}$ – the total volume of ^{85}Kr in the GFP mixture in the swelling bubble volume, cm^3;
$\upsilon_{Kr\text{-}85}$ – the content of isotope ^{85}Kr in the GFP mixture in the swelling bubble volume, % (vol.);
$\beta_{\sum Xe/\sum Kr}$ – the ratio of the total content of the xenon isotopes in the GFP mixture in the swelling bubble volume, rel. units.

The unknown value $V_{Kr\text{-}85}$ in expression (4) can be determined from the data of the gamma-spectrometer measurements by using expression [2], that relates the radionuclide activity with its mass and half life

$$M = 2{,}41\cdot10^{-24}\cdot A\cdot A_n\cdot T^{1/2}, \quad (5)$$

where M – the radionuclide mass, g;
A – the radionuclide activity, Bq;
A_n – the mass number of nuclei of the radionuclide;
$T^{1/2}$ – the half life of the radionuclide, sec.

Then taking into account that 1 gram-molecule of gas is equal to 22.4 liter, one obtains an expression to determine the unknown value $V_{Kr\text{-}85}$ in (4)

$V_{Kr\text{-}85} = 22.4 \cdot M/A_n = 5{,}4 \cdot 10^{-20} \cdot A \cdot T^{1/2}$. (6)

Thus, according to expressions (4) and (6), the data in Table 2 and the activity of ^{85}Kr the calculation value of $V_{\sum Kr+Xe}$ is 3.1 cm^3, that correlates well with the data of the manometer measurements.

It is known from literature that 24.7 cm^3 of GFP [3] is formed from a burn up of 1 gram of uranium-235. Thus, knowing the geometrical sizes of the swelling bubble and a fuel burn up value in the region of the swelling bubble formation one can estimate a total volume of GFP that formed in the fuel meat with sizes of the swelling bubble by using the expression

$$V_{GFP} = v_{GFP} \cdot \hat{A}u \cdot m^{sb}_{U-235}/100 = v_{GFP} \cdot Bu \cdot \frac{m^{fe}_{U-235} \cdot \pi \cdot D^2 \cdot d \cdot L_{fe}}{4 \cdot 100 \cdot V_{fe} \cdot L_{al}}, \quad (7)$$

where V_{GFP} – the volume of GFP, cm^3;

v_{GFP} – the volume of the mixture of Xe–Kr isotopes, formed by a fission of 1 gram of ^{235}U, v_{GFP} = 24.7 cm^3 [3];

Bu – the ^{235}U burn up in the swelling bubble region, %;

m^{sb}_{U-235} – the ^{235}U mass per region of a swelling bubble size, g;

m^{fe}_{U-235} – the ^{235}U load in the fuel meat of the fuel element, g;

V_{sb} – the volume of a fuel element part, that corresponds to a region of a swelling bubble size, cm^3;

V_{fe} – the total volume of the fuel element, cm^3;

L_{fe} – the fuel element length, cm;

L_{al} – the active layer length in the fuel element, cm;

D – the diameter of the swelling bubble, cm;

d – the thickness of a fuel element wall, cm.

The calculation value of the GFP volume V_{GFP} equals to ~9 cm^3. Thus, only ~1/3 GFP, formed in the fuel meat in the swelling bubble region, came out of the fuel particles and aluminum matrix to form a gas cavity of a volume of ~0.54 cm^3 by the end of the fuel element test.

The gas pressure was estimated proceeding from the condition of an equilibrium of gas pressure inside the swelling bubble and stresses occurred in the region of swelling bubble in two fuel claddings of elliptical form as the result of a gas pressure impact on the claddings from within the swelling bubble [4]. For the estimate, it was assumed that the stresses in the elliptical claddings of the swelling bubble were equal to yield strength of the cladding material ($\sigma_{0,2}$(SAV-1)=160 MPa [5]), and the thickness of the elliptical claddings in the swelling bubble region was taken equal to a half thickness of the fuel element wall. The above calculations show that to make such form-changes on the fuel element the excess gas pressure inside the swelling bubble would have to be ~840 kPa, whose absolute value, with the account of an atmospheric pressure and a water column height, would be equal to ~1010 kPa. If so, then by the Charles law, the average gas temperature inside the swelling bubble at the final phase of its formation could make ~180 ^{o}C.

4. Conclusions

There were experimentally determined: the free volume inside the swelling bubble volume, pressure, gamma–activity, chemical and nuclide compositions of gas inside the swelling

bubble formed in the fuel element with a dispersion U-Mo/Al fuel in the fuel assembly ”KM004” irradiated to an average fuel burn-up of ~80 % in the IVV-2M reactor.

The free volume inside the swelling bubble is equal to 0.54 cm^3.

The gas inside the fuel element is the mixture of xenon and krypton with a ratio $\sum Xe/\sum Kr=8.33$.

The volume and pressure of the gas in the free volume inside the swelling bubble under normal conditions are 3.18 cm^3 and 594 kPa, respectively.

The volume of the gas inside the swelling bubble is ~1/3 of the volume of the GFP, formed in the fuel meat with the volume corresponding to the geometrical sizes of the swelling bubble. The calculation value of the temperature inside the swelling bubble could reach ~180 ^oC.

5. References

[1] Golosov O.A., Lyutikova M.S., Semerikov V.B. et al. “The results of studying uranium-molybdenum fuel elements irradiated in the IVV-2M reactor to high burn-up values” // 9th Int. Mtg. RRFM’2005, Budapest, Hungary, 10-13 April, 2005.

[2] Kozlov V.F. Reference book on radiation safety.- M.: Energoatomizdat, 1987. 192 p.

[3] Likhachev Yu.I., Pupko V.Ya. Strenght of fuel elements of nuclear reactors. M.: Atomizdat, 1975. 280 p.

[4] Norms of strength calculations for equipment and piping of atomic power installations (PNAE G-7-002-86).- M.: Gosatomenergonadzor, 1989. 525 p.

[5] Nikitin V.I. High-temperature strength, plasticity and corrosion of avial.- M.: Metallurgia, 1978. 152 p.

HIGH RESOLUTION REACTOR MODELLING FOR THE SIMULATION OF THE ACTIVITY DISTRIBUTION AND RADIATION FIELD AT THE GERMAN FRJ-2 RESEARCH REACTOR

D. WINTER[1], F. ABBASI[1], F. SIMONS[1], R. NABBI[1], B. THOMAUSKE[1], G. DAMM[2]

[1]Institute of Nuclear Fuel Cycle - RWTH Aachen, Elisabethstr. 16, 52062 – Germany

[2]Research Centre Juelich, Wilhelm-Johnen-Strasse, 52425 Juelich, Germany

ABSTRACT

The decommissioning of nuclear facilities demands detailed modelling efforts in order to optimise the quantification and characterisation of nuclear waste as well as to realise optimum radiation protection. For this aim, detailed activity and dose rate atlases (ADAs) are required for the approval of a decommissioning project in Germany [1]. At present, a comprehensive simulation tool is developed at the Institute of Nuclear Fuel Cycle – RWTH Aachen which has the capability to automatically cover the range of demands for ADAs. The main goal of this tool is not only the automated calculation of the ADAs in a high resolution, but also the 3D-visualisation in the form of a CAD-based virtual reactor. This paper encompasses the descriptions of the applied methods used by the simulation tool and algorithms for coupling of the different simulation codes as well as first results of the application to the German FRJ-2 research reactor.

1 Introduction

The decommissioning of nuclear facilities demands detailed modelling efforts in order to perform analysis in terms of the quantification and the characterisation of nuclear waste as well as to realise optimum radiation protection. Therefore, activity and dose rate atlases (ADAs) are necessarily required for a decommissioning approval from the domestic safety authorities in Germany [1].

For the generation of ADAs computer codes based on Monte Carlo methods are increasingly employed because of their potential for high resolution simulation of detailed neutron and gamma transport. However, the demand on the modelling effort and the simulation time increases with the size and complexity of the whole model resulting in a limiting factor for the detailed determination of flux, activity, and dose rates. For instance, the German FRJ-2 research reactor, consisting of a complex reactor core, the graphite reflector, and the adjacent thermal and biological shielding structures, represents such a case. For the solving of this drawback, various techniques such as variance reduction methods are applied. A further simple but effective approach is the modelling of only the regions of interest with appropriate boundary conditions e.g. source terms or reflective surfaces.

In the framework of an existing research project founded by the German Federal Ministry of Education and Research (BMBF), a high sophisticated simulation tool is developed at the Institute of Nuclear Fuel Cycle – RWTH Aachen which is characterised by:

1. CAD-based model generation for the Monte Carlo simulations
2. Production of high resolution activity and dose rate atlases
3. Application of coupling routines and interface structures for optimum and automated simulations

The whole simulation system is based on the Monte Carlo code MCNP5 [2] and the depletion/activation code ORIGEN2 [3]. The numerical and computational efficiency of the proposed method is discussed in this paper in terms of modelling and simulation of the FRJ-2 research reactor with emphasis on the effect of the application of variance reduction methods.

2 Details on the Reactor and Power History [4]

The FRJ-2 is a DIDO-class tank-type research reactor which is moderated and cooled by heavy water passing through the aluminium tank surrounded by the graphite reflector which is enclosed in a double walled steel tank. The core consists of 25 tubular MTR fuel elements arranged in five rows of 4, 6, 5, 6, and 4.

The active part of the tubular fuel elements is formed by four concentric tubes, having a wall thickness of 1.50 mm, and a length of 0.60 m. Each tube is formed by three material testing fuel plates containing highly enriched uranium oxide (80%) in a clad with pure aluminium. The annular water gap between the tubes has a width of about 2.5 mm leaving a central hole of 50 mm in diameter. The tubes are accommodated in a shroud tube of 103 mm in diameter, to which they are attached by four combs at the lower and upper ends.

The reactor is equipped with two diverse and independent shutdown systems: the coarse control arms (CCAs) and the rapid shutdown rods (RSRs). In case of demand, the six CCAs are released from their electromagnets and dropped into the shutdown position by gravity, whereas the three RSRs are shot in by their pneumatic actuators. The absorber plate of CCAs contains cadmium of natural isotopic composition. The shutdown position of the CCAs is at an angle of 56° with the vertical axis.

There are several channels for irradiation purposes passing through the reflector. For experimental purposes the reactor is equipped with a thermal column made of graphite.

The reactor reached its first criticality in 1962 and was operated till 1967 at a power level of 10 MW. Because of its capability and potential, the reactor power was increased first to 15 MW and finally to 23 MW in 1970 till shutdown in 2006. The analysis of the whole power history of the FRJ-2 reactor results in a total operation time of 19.6 years and an average power of 20 MW.

3 Modelling and Simulation Methods

In particular, nuclear material and testing reactors show a high complexity in the design and construction in comparison to nuclear power plants resulting from the use of different diagnostics and measurement systems applied for different scientific purposes. This high complex construction grade has to be taken into account for detailed nuclear simulations.

For the decommissioning, regions of interest (ROI) are located around the reactor core consisting of a graphite reflector and whole structures of the thermal and biological shield. All components and structures that are within the active reactor core are highly activated and considered for direct disposal. From this point of view, the geometry model of the reactor for nuclear simulations can be split into an active core and an out-core model.

The active core model is then used to perform neutron transport simulations in order to obtain the neutron source distribution for the subsequent application in the out-core structure model for neutron transport simulations. By this method, the model complexity and hence the simulation effort for the ADAs is then shifted to the beltline and outer regions, and the neutron transport throughout the complex active core zone need not be simulated in further steps.

In addition to the splitting of the whole model for the Monte Carlo calculation, a further variance reduction method is applied which is optimised weight windows. Weight windows artificially vary the number of particle histories that contribute to a specific tallied volume. Because the statistical uncertainties of the Monte Carlo results scale with this number, this approach leads to an effective reduction of the variances as well.

The employed simulation tools are the Monte Carlo N-Particle code MCNP5 (Version 1.60, [2]) and ORIGEN (Version 2.2, [3]). The former code is a general-purpose, continuous-energy, generalized-geometry, time-dependent, Monte Carlo radiation transport code and the latter code system is employed for the calculations of the build-up, decay, and processing of radioactive materials.

3.1 MCNP Model of the Active Core

The ADAs are not required for active core components because this part of the reactor shows a high level of radioactivity and the fuel assemblies are unloaded in an earlier stage of the decommissioning process. The components are consequently considered as high-level waste and are put into disposal. However, modelling of the active core is needed for the simulation of the neutron power history and distribution that causes the activation of the individ-

ual structures. By using the whole reactor geometry with a detailed core model, a source particle distribution for the subsequent out-core model is generated. This model was produced at the Research Centre Juelich for the MCNP code and is plotted in figure 1 [5, 6].

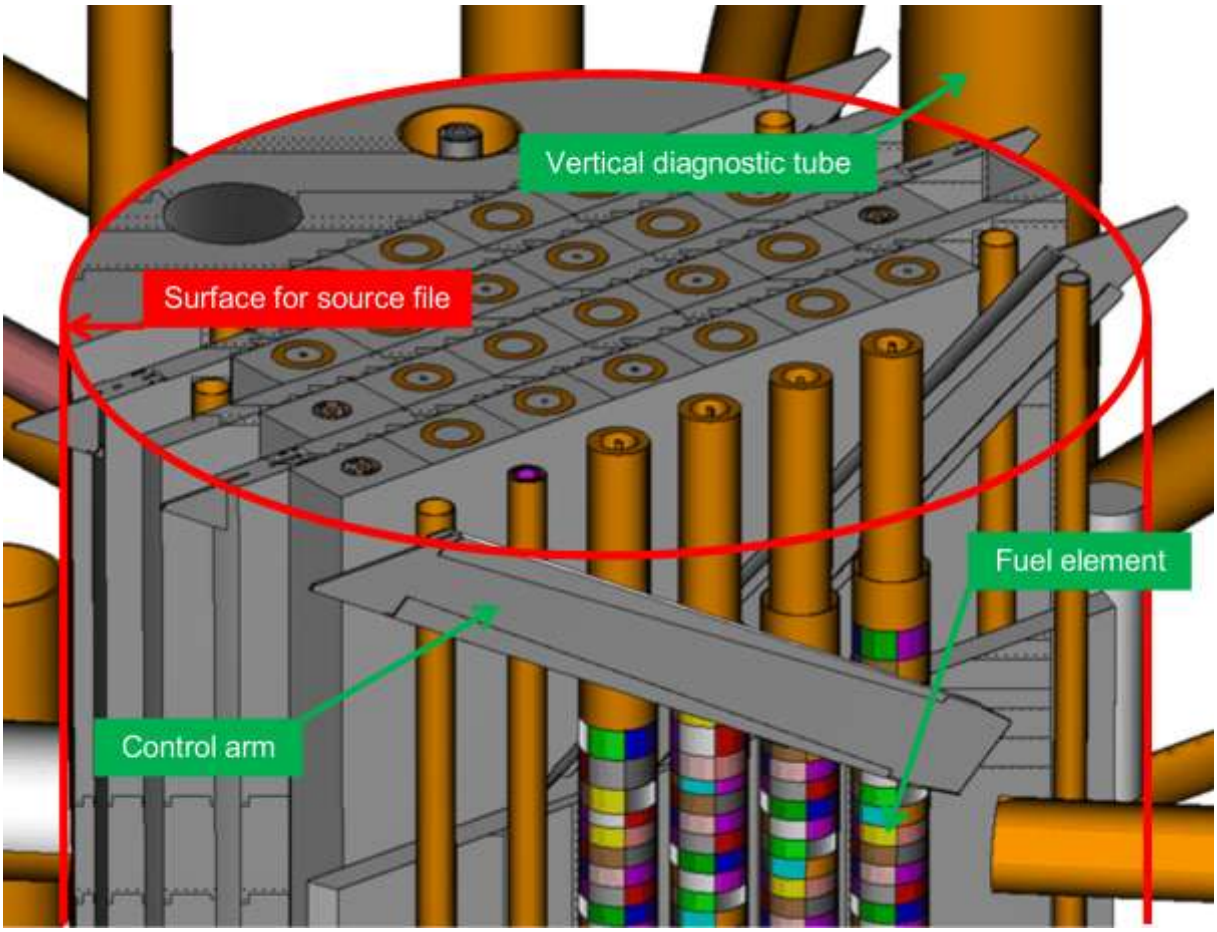

Fig. 1. MCNP model of the active reactor core plotted with Sabrina [7] (some components are made transparent)

The generation of the source particle distribution is achieved by the use of the surface-source-write/read cards in the MCNP input file (SSW/SSR). If the SSW card is activated, MCNP generates a source file containing data of all neutrons crossing an enclosed surface (red lines in figure 1) outward the core in terms of particle type, angle, and energy. The main advantage is that only particle histories are tracked which cross the defined surface and enters into the surrounding structures, whereas, all particle tracks crossing the surface backwards are skipped.
As a consequence, this technique allows a significant gain in simulation efficiency for the out-core structures and the CPU time is decreased by a factor of 20. The reason is that the fraction of neutrons interacting within the reactor core amounts to more than 95%.
In addition to the surface source approach, variance reduction methods in the form of mesh-based weight windows are applied to increase the efficiency of the simulation in terms of high accuracy in all activated zones of out-core structures (see chapter 3.3).

3.2 Out-Core Structure Model

The out-core structure model consisting of the graphite reflector and surrounding biological shielding structures was generated by the Research Centre Juelich in the computer-aided design (CAD) environment and consists of approximately 1200 different components. In order to adjust this geometrical model, some components were removed that have negligible or no influence on particle transport simulations because of their spatial position, material definition (small nuclear reaction cross sections), or respective volumes.

For neutron and gamma transport calculations, the CAD model is converted into the MCNP syntax. For this aim, the CAD-converter tool McCAD (version 0.3.0), which has been developed by the Karlsruhe Institute for Technology (KIT), was employed which processes CAD models in the STEP format ("STandard for the Exchange of Product") [8]. Additionally, this conversion code is limited to some specific volumetric solids and cannot deal with bodies generated by e.g. spline functions. However, only three parts of the whole model were defined by spline functions, but those could be removed as well because of negligible volumes and low influence on the neutron or photon transport.
The CAD-converter tool McCAD, firstly, cuts the solids in the STEP model into different solids representing the final MCNP cells which are constructed by simple surface definitions such as planes, cones, cylinders, and spheres. This step is called decomposition. Secondly, based on the decomposed CAD model, McCAD produces a voxel model for overlap testing and performs subsequently a collision test. Thirdly, with the results of the collision test, the solid MCNP cells are generated from the decomposed STEP model. Next, the empty spaces between the solids are discretised and defined as void cells. This step is necessary because the Monte Carlo code does not allow undefined regions in the geometry. Lastly, the material definition numbers and the respective densities, which are stored in an external file, have to be linked to the solid MCNP cells. The isotopic compositions associated with the material definition numbers are added to the MCNP input file by hand.
Figure 2 shows two cross section views of the CAD model (left) and the converted MCNP model (right).

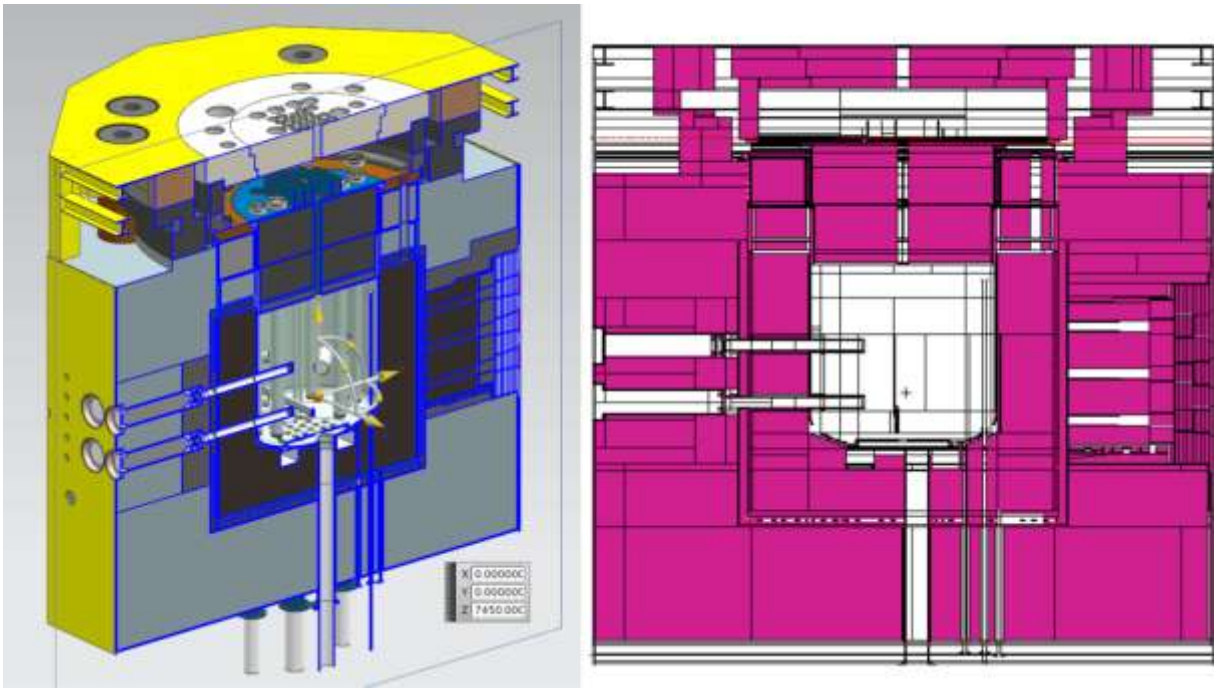

Fig. 2. CAD model of the out-core structures (left) and the converted MCNP model (right)

3.3 Utilisation of Variance Reduction Techniques

The main challenge when using Monte Carlo simulations for large systems which consists of strongly absorbing materials is the handling of the uncertainties in the outer structures of the whole model. In general, the uncertainty of a Monte Carlo result scales with $1/\sqrt{N}$, where N is the number of particles which reach a desired volume. Due to the neutronics effect of the graphite reflector and the surrounding boron layer the source neutrons originating from the active core are strongly attenuated and only a small fraction of the neutrons are sampled in the outer structures causing high uncertainties there. However, the number of particles can artificially be increased with MCNP by so called importance factors resulting in a reduction of the variances.

For instance, if a neutron enters a new cell the ratio between the importance of the actual and the preceding cell determines the multiplication factor of the particle. In this process, the total weight of the particular neutron has to be conserved (weight conservation law). By this way, the number of neutrons is artificially increased associated with lower uncertainties as depicted on the right hand side of figure 3.
Besides the adjustment of importance factors, particle weights are an effective approach for error minimising in Monte Carlo simulations. If the particle weight control is activated a lower and an upper bound of the weights are defined. If the neutron falls below the lower bound due to e.g. energy loss caused by collisions, the Russian roulette method is applied. This means, a random number decides whether the neutron track is terminated or the weight of the neutron is increased to the lower bound. On the other hand, if the neutron's weight is above the upper bound it is split into two or more neutrons with evenly distributed weights which are in turn within the defined limits. By all these methods, the total weight conservation is met.
MCNP provides a couple of variance reduction techniques such as the above discussed importance factors and particle weights. A combination of both methods is called weight windows (WW). These are applied to reduce the uncertainties of a certain tallied quantity. This is performed by the sampling of particle histories throughout the problem and, especially, storing those histories that contribute to the desired tally. Afterwards, importance factors are set according to the stored particle tracks in order to amplify them in a subsequent run. The importance factors can either be cell-based or mesh-based. Cell-based importance factors are appropriate for small cell volumes and mesh-based importance factors for larger cell-volumes where an internal distinction of the importance factors is required.
For mesh-based WW the user spans a mesh over the area of interest and tallies the designated particle in every mesh element. This approach is therefore independent from any MCNP cell. Figure 3 shows for the first MCNP model of the FRJ-2 the spatial distribution of the mesh-based importance factors (left) and the impact on the neutron spectrum for the same amount of computer time and same geometry (right). These results have been obtained for a volume tally of the lead layer enclosing the concrete shield indicated by the red lines.

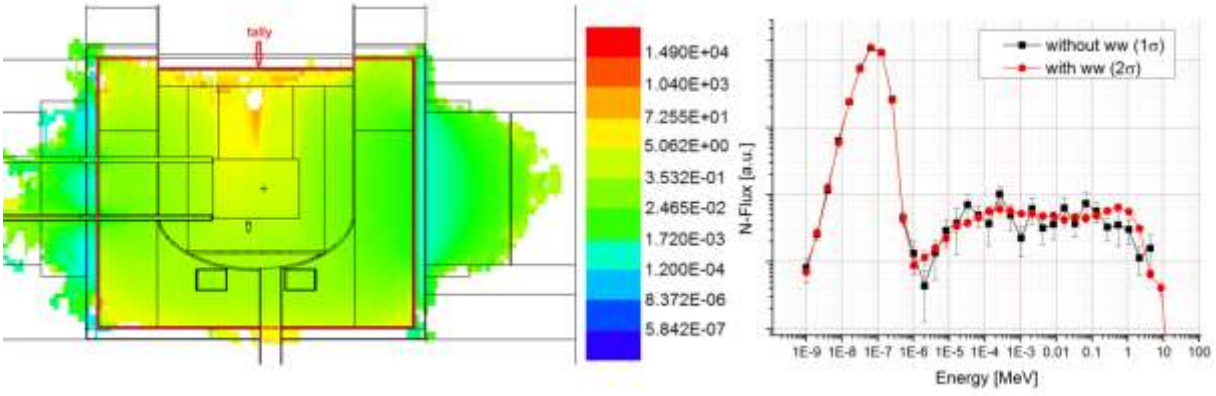

Fig. 3. MCNP results of the volume flux tally for the lead layer of the FRJ-2 (red lines, left): generated importance factors (left) and the neutron spectrum with and without the application of weight windows (right)

The white areas on the left side of figure 3 indicate that no neutrons are scattered into the tallied volume from these cells, therefore, the importance is set to zero in those zones in order achieve higher sampling in the tallied volume. Accordingly, the use of WWs results in significantly smaller uncertainties for the tallied quantities compared to results where no WWs were utilised as can be seen in the red and black curves on the right side of figure 3, respectively.

3.4 Activity and Dose Rate Distribution

The temporal activation of the components exposed to a neutron radiation field depends strongly on the neutron spectrum. The neutron spectrum in turn shows a strong spatial dependency due to the strong attenuation in the shielding materials.

For the activation calculations the Bateman solver ORIGIN is employed which requires amongst others one-group microscopic cross section values. These data can be generated either directly with MCNP by using MT numbers or with energy-dependent flux estimates tallies and subsequent reaction rate calculations. Within the scope of this project, the latter way is chosen because it occupies less computer memory during the MCNP calculation due to the shifting of the cross section calculations to a subsequent routine. This routine is then based only on the MCNP energy-dependent flux estimates and nuclear databases.

For this method, the neutron spectrum has to be tallied in as many as possible energy groups in at least every solid zone of the MCNP input. Based on these ultrafine spectra, one-group microscopic cross sections are generated for every material cell, for every nuclear activation reaction, and for every isotope of interest. Because of the standard format, the microscopic cross section data can be taken from any nuclear database such as the ENDF/B-VII or the EAF-2010 [9, 10].

These one-group cross sections are employed for activation calculations with ORIGEN. Besides the cross sections, ORIGEN requires the material composition, the irradiation time, and the absolute neutron flux value. The material composition and the irradiation time are known from the MCNP input and the operation history, respectively, and the absolute neutron flux value is obtained with a second MCNP flux estimates and a flux multiplication factor.

In order to achieve a high spatial resolution for the activity results, the neutron flux distribution is tallied using the mesh tally feature of MCNP which is, comparable to the mesh-based WW, independent from any MCNP cell. Although one-group cross sections exist only for single components, the activity can, in this way, be calculated with a spatial resolution under the assumption that the cross sections do not vary within the components. Finally, an activity atlas is created for later 3D visualisation.

Besides the activity, ORIGEN is capable to provide gamma sources in 18 energy groups. These data are available for every mesh element in which activity results exist. With these spectra a gamma source distribution is generated and can be subsequently used for radiation transport simulation by MCNP. Hence, MCNP calculates, via flux-to-dose coefficients, the dose rate which can be obtained with mesh tallies as well allowing the creation of a dose rate atlas for later 3D visualisation.

Because of complicated interface structures and coupling routines between different computer codes, the whole simulation tool for the generation of ADAs is complex. An overview of the entire method of the simulation scheme is depicted in figure 4.

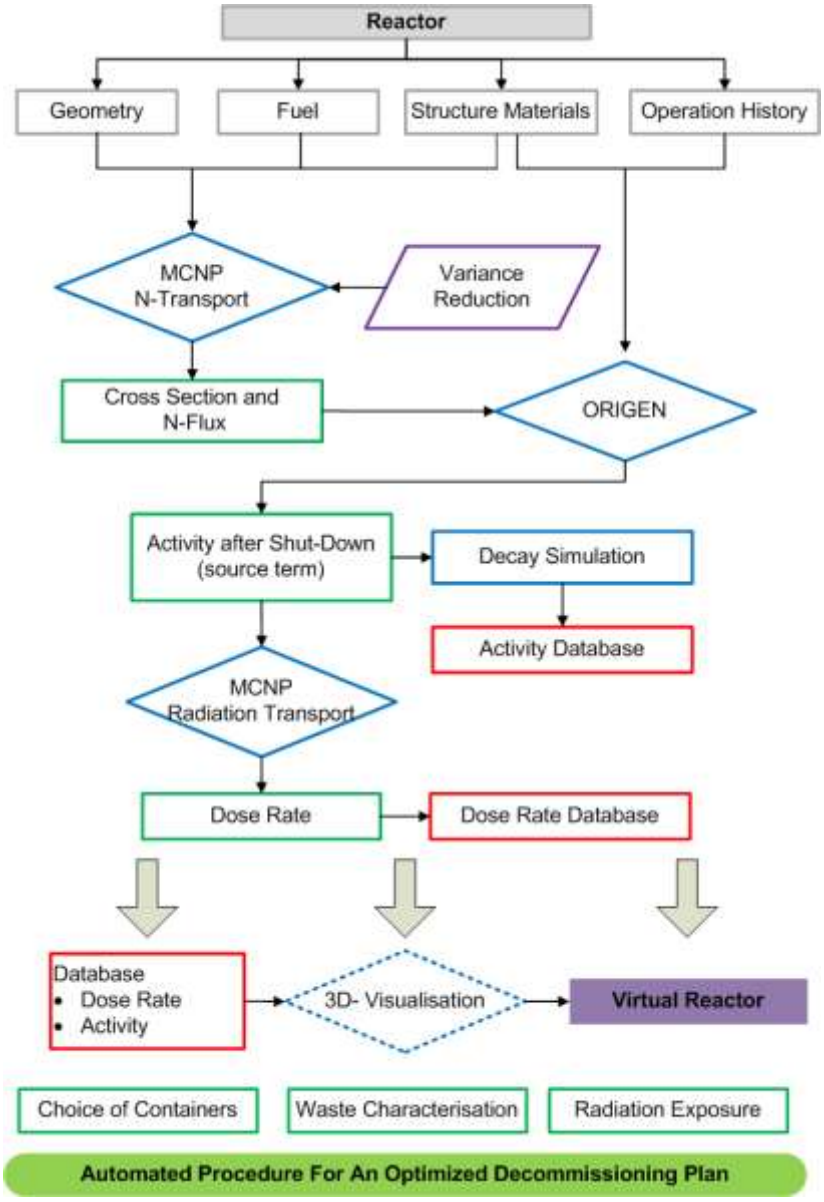

Fig. 4 Structure of the high resolution method for the comprehensive and automated simulation of the activity and dose rate distribution

4 Summary and Outlook

For the decommissioning of nuclear facilities in Germany, activity and dose rate atlases (ADAs) are required in order to realise and manage a decommissioning plan and optimise the radiation protection measures. Additionally, detailed ADAs support and lead to minimal radiation exposure of the staff involved in the dismantling issue. Finally, ADAs have the potential to efficiently minimise the cost for decommissioning because the nuclear waste can be characterised and quantified in more detail.

Therefore, the demand for high detailed ADAs exists and a sophisticated and automated simulation tool for the generation of ADAs is currently developed at the Institute of Nuclear Fuel Cycle – RWTH Aachen. Some chosen results obtained with the first models are presented in this paper and the new features of the entire simulation tool for the generation of ADAs are discussed.

The main features are

1. Generation of reactor-type-based activation cross section data libraries
2. Embedded variance reduction techniques
3. Algorithm for the conversion of CAD-based models to the MCNP model
4. Generation of ADAs in high spatial resolution

5. 3D visualisation of the fluence, activity, and dose rate results

The currently achieved milestones of this project are, first, the completion of the required Java-routines for the creation of the activation cross section libraries from neutron spectra obtained with MCNP flux estimates, second, the integration of variance reduction techniques were implemented and verified for the first FRJ-2 MCNP model and, last, the conversion of CAD models to the MCNP model showing a high level of resolution has been performed.

5 Acknowledgement

This project is funded by the German Federal Ministry of Education and Research (BMBF) within the framework of the research and development programme “Decommissioning, dismantling, and disposal of nuclear research reactors” under the project Number: 02S9042.

6 References

[1] E. Ziegler, *Atomgesetz mit Verordnungen*, 31. Auflage, Nomos, Baden-Baden, 2012

[2] X-5 Monte Carlo Team, *MCNP — A General Monte Carlo N-Particle Transport Code, Version 5*, Los Alamos National Laboratory, 2008

[3] A. G. Croff, *ORIGEN2: A Versatile Computer Code for Calculating the Nuclide Compositions and Characteristics of Nuclear Materials*, Nucl. Technol., **62**, p 335, 1983

[4] P. A. Palenberg, *Sicherheitsbericht fuer den Forschungsreaktor FRJ-2 (DIDO) mit einer thermischen Leistung bis maximal 25 MW*, NRW Landesamt fuer Forschung, 1962

[5] R. Nabbi, W. Bernat, *Application of Coupled Monte Carlo and Burn-Up Method for Detailed Neutronic Analysis for the FRJ-2 Research Reactor on High Performance Computers*, The Monte Carlo Method: Versatility Unbounded In A Dynamic Computing World, Chattanooga, Tennesse, 2005

[6] P. Bourauel, *Calculation of neutron flux distribution for the FRJ-2 research reactor with the Monte Carlo simulation code MCNP*, Master Thesis, Forschungszentrum Juelich, 2006

[7] K. A. van Riper, *Geometry creation for MCNP by SABRINA and XSM*, Eighth International Conference on Radiation Shielding, Arlington, 1994

[8] D. Grosse, H. T. Tamirat, *Current Status of the CAD Interface Programme for MC Particle Transport Codes McCad*, Internat. Conf. on Advances in Mathematics, Computational Methods and Reactor Physics, Saratoga Springs, N.Y., 2009

[9] M. B. Chadwick et al., *ENDF/B-VII.1 Nuclear Data for Science and Technology: Cross Sections, Covariances, Fission Product Yields and Decay Data*, Nuclear Data Sheets, **112**, Issue 12, 2011, Pages 2887-2996

[10] J.-Ch. Sublet, L. W. Packer, J. Kopecky, R. A. Forrest, A. J. Koning, and D. A. Rochman, *The European Activation File: EAF-2010 neutron-induced cross section library,* EASY Documentation Series CCFE-R (10) 05, Culham Centre for Fusion Energy, 2010

CALCULATED AND EXPERIMENTAL JUSTIFICATION OF A POSSIBILITY TO PROVIDE TEMPERATURE CONDITIONS FOR STRUCTURAL MATERIALS IRRADIATED IN REACTOR BOR-60

A.V. Varivtcev, S.G. Eremin, I.Yu. Zhemkov, A.N. Kozolup,
A.I. Plotnikov, N.S. Poglyad
JSC "SSC RIAR", 433510, Dimitrovgrad-10, Ulyanovsk region.

INTRODUCTION

When scheduling and performing in-pile tests of promising materials and items, the key task is to provide the required temperature conditions. If we do not have reliable data on the irradiation temperature of the materials under study, it is quite difficult to interpret correctly such processes as swelling, corrosion, creep, etc. At present, BOR-60 is used for in-pile tests of promising structural materials to be operated in hard neutron spectrum in liquid metal coolant. The BOR-60 irradiation temperatures range from 320°C ("cold" irradiation) to 700°C ("hot" irradiation), while the requirements to the stability and accuracy of temperature conditions become tougher.

The temperature conditions of experimental devices irradiation, including the gas gap between capsules and cooling sodium flow, mainly depend on heat rate in the capsules, reactor sodium temperature, composition and size of the gas gap and emissivity factor of the capsules walls (at high temperatures).

To justify a possibility to maintain the temperature during irradiation of structural materials as well as to improve the accuracy of the irradiation conditions calculations, a methodical experiment [1] was performed. The experiment showed that the difference between the calculated and experimental temperatures was within 20÷30°C for "hot" irradiation conditions (T=500÷600°C) and within 0°C÷7°C for "cold" irradiation conditions (T=350÷380°C). The heat rate was calculated by the technique for short-time scheduling of reactor tests developed by the authors [2]. It allows us to approximately evaluate the contribution of delayed gamma radiation from fuel composition nuclei fission products.

The purpose of work was to specify the calculated temperatures by means of the improved method of the heat rate calculation in the irradiation rig components [2].

EXPERIMENT

The methodical experiment to evaluate irradiation temperatures for different materials was performed in 2010. For this purpose, an irradiation rig (IR) was developed and located in the BOR-60 D23 cell.

Inside the IR, there was a structure consisting of five segments. Each segment was a leak tight welded design with two cavities, inner and outer. The outer cavity was filled with gas.

The segments, containing in their inner cavity capsules with hafnium hydride (HfH_x) in sodium medium, were located at levels 1 and 2 of the structure (core bottom). The axial and lateral sections of the hafnium hydride segment are given in Fig.1.

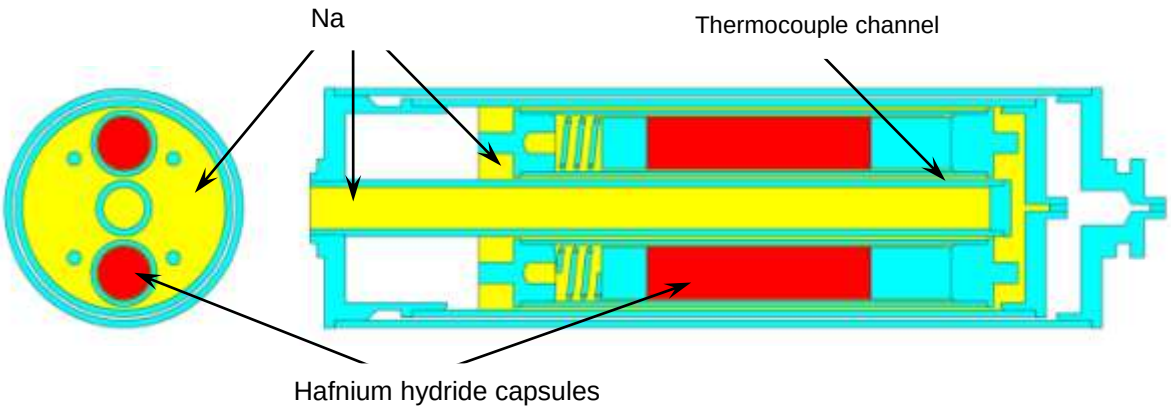

a) b)

Fig 1. Lateral (a) and axial (b) sections of hafnium hydride segments

A segment with sodium and steel was located at the level 3 corresponding to the core central plane. The segment inner cavity was filled with sodium. The segment had a channel to locate thermocouples. The lateral and axial sections of the sodium and steel segment are given in Fig.2.

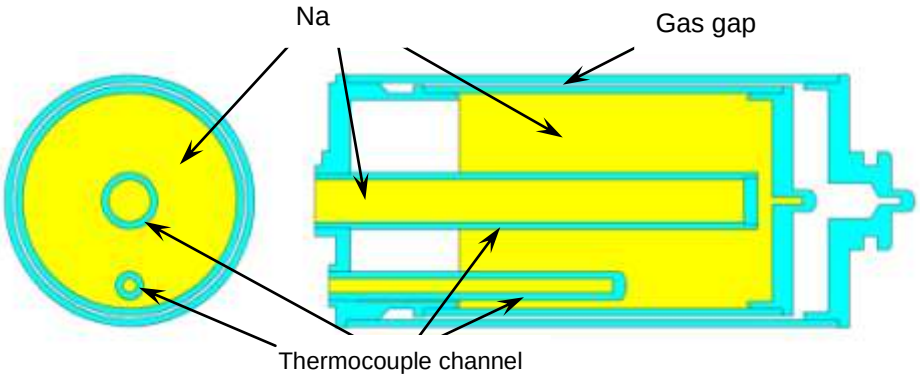

a) b)

Fig 2. Lateral (a) and axial (b) sections of sodium and steel segment

Segments having lead-cooled steel samples in the inner cavity were located at the levels 4 and 5 (core top). The segment had two pockets for thermocouples. The lateral and axial sections of the lead segments are given in Fig. 3.

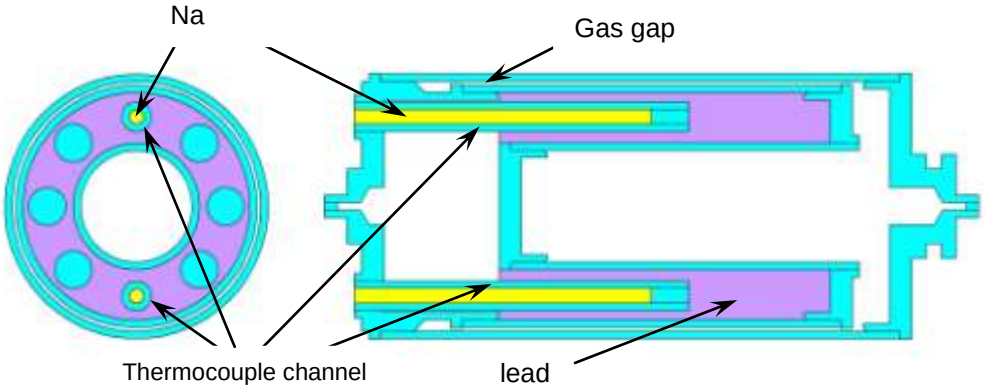

a) б)

Fig 3. Lateral (a) and axial (b) sections of lead segment

The calculations [1] resulted in the evaluation of required gas gap size and composition - helium. Once the IRs were fabricated, the actual gas gaps size was defined to

be a little different than required. Table 1 presents the required and measured gas gap sizes per levels.

Level	Material	Recommended gap, mm	Measured gap, mm
1	Na-cooled hafnium hydride	0.44	0.45±0.05
2	Na-cooled hafnium hydride	0.50	0.51±0.03
3	Na	0.10	0.12±0.05
4	Lead-cooled steel samples	0.18	0.18±0.02
5	Lead-cooled steel samples	0.32	0.33±0.04

Tab 1. Gas gaps (helium) size per IR levels (T~20°C)

On June 22, 2012, during the scheduled BOR-60 outage, an IR with 12 thermocouples was installed in cell D23; the thermocouples were connected to the data-measurement system (DMS) [3] to measure temperature. The temperatures recorded by the IR thermocouples differed from the one of the reactor sodium from –1°C to +9°C.

The DMS recorded the key parameters of the reactor and IR during the whole micro-run: reactor thermal power, coolant flow rate, inlet and outlet coolant temperature and temperatures recorded by the thermocouples in IR (Fig.4).

Fig 4. DMS readings during the methodical experiment

HEAT RATE CALCULATION

During the methodical experiment, the core was arranged of 113 standard fuel assemblies (FAs). In the steel blanket there was one breeding assembly made from depleted uranium. Figure 5 presents the BOR-60 core arrangement.

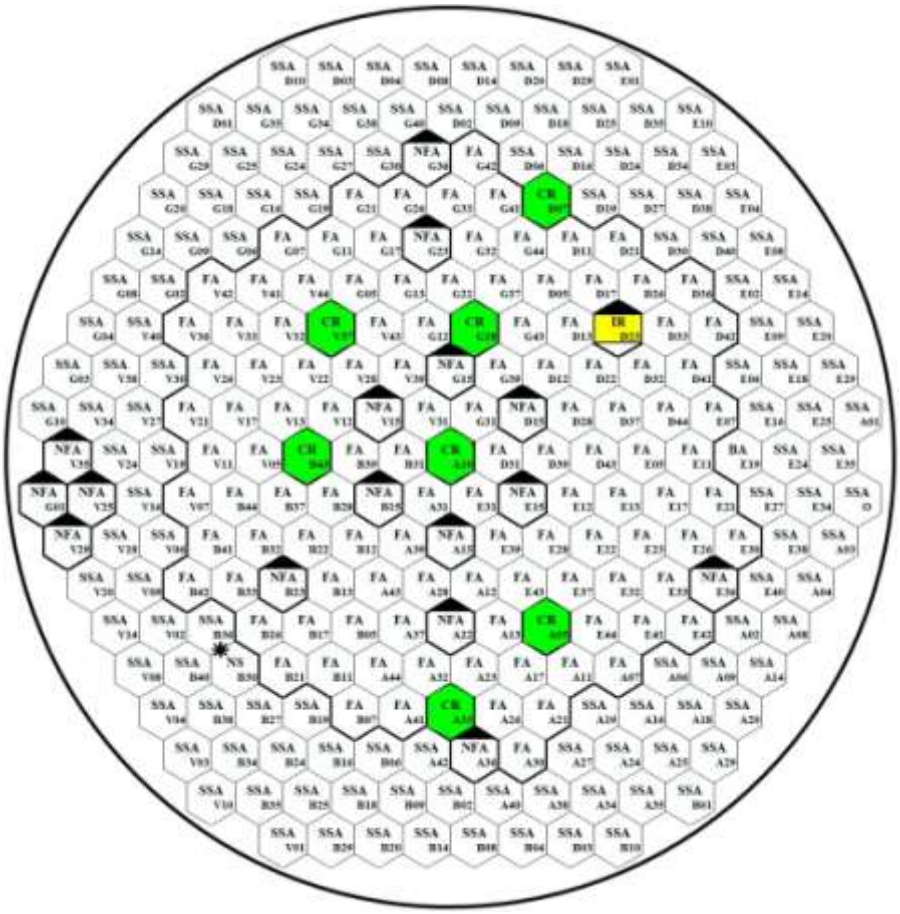

Fig 5. BOR-60 core arrangement
FA – fuel assembly; NFA – non-fuel assembly; BA – steel shield assembly;
BA –breeding assembly; CR – control rods, IR – irradiation rig.

3D reactor model was created by means of the BOR-60 automated computation system [4] intended for creating calculation models with the account of actual location of all assemblies, fuel composition, absorber and structural materials.

The earlier experiments [1] showed that the maximum difference between the calculated and experimental values was observed at the outermost levels located at the boundary between the core and breeder blanket. This difference was mainly caused by the overestimated heat rate values due to both inaccuracy in the reactor model and selected calculation method. At the IR designing stage, the heat rate was evaluated by a technique for short-time scheduling of reactor experiments. This technique estimates approximately the contribution of delayed gamma radiation from fuel composition nuclei fission products. The heat rate values calculated by means of MCU-RR software under the criticality-calculation mode were multiplied by a correction factor ~1.55 (in that micro-run).

It should be mentioned that this technique does not account the fact that the delayed gamma radiation contribution to the heat rate decreases at the radial periphery and edges of the core. That is why a decision was taken to calculate the heat rate by a improved technique. In addition, some updates were introduced into the reactor model to account more accurately the edge leakage of neutrons and gammas.

The calculation was performed to have IR heat rate values being the initial data for the thermo-hydraulic calculation.

At the first stage, the calculation was done by means of MCU-RR software [5] under the criticality calculation mode using a PNDOUS sub-module [6]. The following data were obtained:

- values of neutron- and prompt gamma- contribution to the heat rate;
- flux density and neutron spectrum in the core;

- distribution of nuclei fission rate over the core.

Then, the AFPA software [7] and public database TORI [8] were used to calculate the isotopics of irradiated fuel and characteristics of delayed gamma radiation – intensity and energy spectrum (15 groups).

The contribution of the delayed gamma radiation to the heat rate was calculated by MCU-RR. For this purpose, the same reactor model calculation was used but a fixed gamma-source was simulated having the set intensity and spectrum distributed over the core in proportion to the fuel nuclei fission rate. To account possible heat rate non-uniformities over the IR, each IR component was calculated. The calculation values were normalized to the thermal reactor capacity of 48 MW. Then, all the heat rate components were summed. Figure 6 presents the axial distribution of specific heat rate in IR materials (steel, sodium, hafnium hydride and lead).

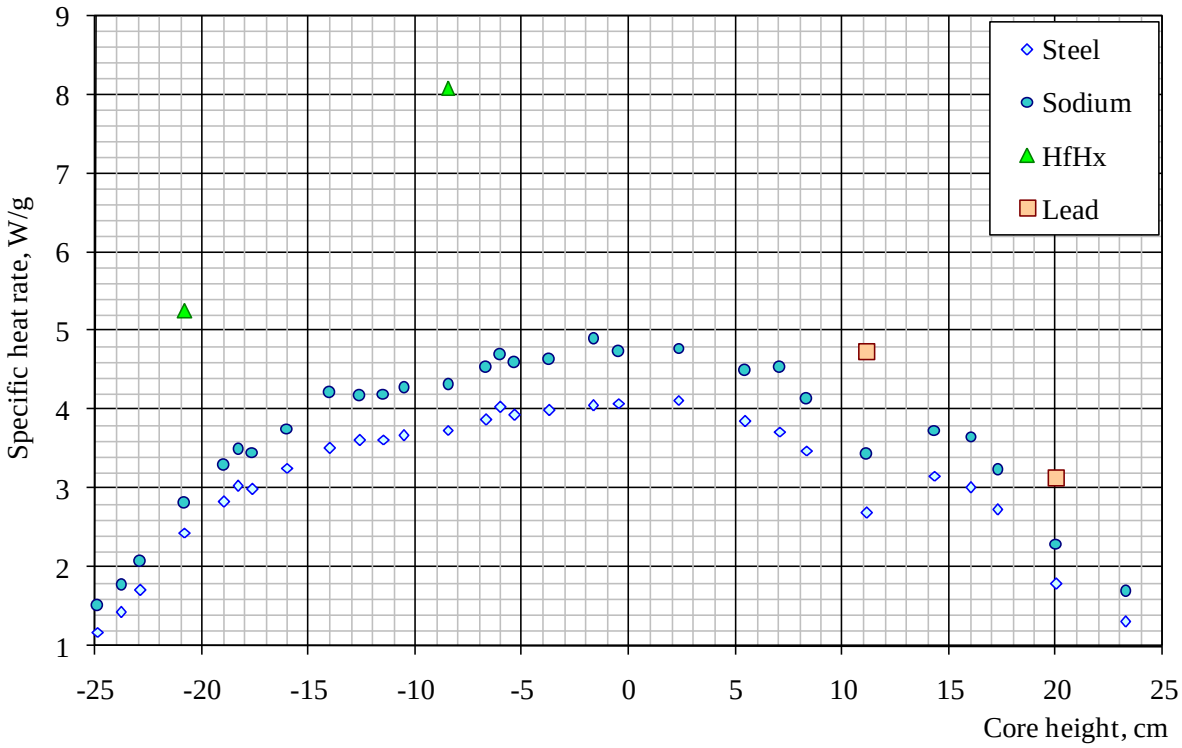

Fig 5. Heat rate axial distribution over IR

THERMO-HYDRAULIC CALCULATION

The IR thermo-hydraulic calculation was done on the basis of the heat rate values. The calculation took into account the heat rate distribution in the IR, samples and coolant along the height, radial and axial heat exchange and radiation heat transfer.

The calculation was done to generate temperature values along the IR levels with the account of the actual gas gap size and specified heat rate values.

The IR thermo-hydraulic characteristics were calculated by the TVEKCF software, a part of the certified DINBOR software [9]. The IR thermo-hydraulic calculation was done for the following parameters: reactor thermal capacity 48MW, inlet sodium temperature 315°C, capsule emissivity factor ε=0.7.

Calculated temperature values along the IR levels were generated. Table 2 presents the calculated and experimental temperatures at all IR levels. Calculated values correspond to average temperature of the samples at the level.

Level	T,ºC (calculation)*	T,ºC (calculation)**	T,ºC (experiment)
1	485	473	466; 460
2	565	560	557; 555
3	373	373	380; 373
4	505	498	483; 490
5	520	503	485; 490

Tab 2. Calculated and experimental temperatures at the IR levels
* – calculation by approximation technique;
** – calculation by improved technique;

As it can be seen from Table 2, the updated models and techniques for heat rate calculation allowed diminishing the discrepancy between the calculated and experimental temperature values.

The calculated temperatures at the central “cold” level did not change and the difference from the experimental values made up 0÷7°C. The highest discrepancy between the experimental and calculated values, 7÷18°C, was still observed at the periphery levels 1 and 5.

Despite the updates and improvements, there is still some overestimation in the calculated temperature values at the outermost levels of the IR and it should be taken into account when scheduling and performing materials in-pile tests.

CONCUSION

The studies show the application of reactor updated models and improved calculation method to be sufficient to have more accurate heat rate values and temperatures, respectively, especially for the IR components located at the core-blanket boundary.

The calculations and experiments show it possible to provide the required temperature conditions (within a 15÷20°C error) to irradiate different materials in the BOR-60 core (T=400÷650°C for “hot” conditions). As for “cold” conditions (T= 320÷400°C), the difference between the calculated and experimental temperatures made up 0°C÷7°C that proved the accurate provision of the required temperatures when irradiating materials in the BOR-60 core.

The improved method of calculation and updated reactor model tested in the frame of this work are widely used to schedule and support reactor test programs.

REFERENCES

1. Varivtsev A.V., Zhemkov I.Yu, Kozolup A.N., et al. Calculations and experimental research in substantiation of structural materials irradiation conditions in BOR-60 reactor. // Bulletin of RAS Samara Research Center, ISSN 1990-5378, 2012, Vol. 14, No.4(4), P. 990-995.
2. Varivtsev A.V., Zhemkov I.Yu. Improved method of irradiation heat rate calculation in BOR-60 reactor // Problems of Atomic Science and Technology. Series: Nuclear Reactor Physics, ISSN 0205-4671, 2012, No.4, P.31-38.
3. Ainikeev R.R., Kozhanov A.A., Kosachevsky V.S., Starozhukov D.I. Operating Manual. Automated sub-system to control basic process parameters (APK OTP BOR-60). SSC RIAR, 2002.
4. Zhemkov I.Yu. Automated computation system to calculate fast reactor characteristics. Proc. of SSC RIAR, Dimitrovgrad, 1996, No.4, P.55-67.
5. Gomin E., Maiorov L. The MCU Monte Carlo Code for 3D Depletion Calculation // Proc. of Intern. Conf. on Mathem. and Comput., Reac. Phys., and Envir. Analyses in Nucl Applications, Sept. 27–30 1999. − Spain: Madrid, 1999. V. 2. P. 997–1006.

6. Vaneev Yu.E., Marikhin N.Yu. Development of sub-module PNDOUS as a part of MCU-RR software to calculate dose characteristics of neutron and photon fields // Proc. of FSUE SSC RIAR, 2009, No.. 1, P.27-36
7. Arkhangelskaya G.A. Softwares to calculate changes in fast reactor fuel isotopics. Report of SSC RF IPPE, No. X 33100, 1980.
8. Chu S.Y.F., Ekström L.P., Firestone R.B. WWW Table of Radioactive Isotopes, database version 2/28/99 [сайт] URL: http://nucleardata.nuclear.lu.se/nucleardata/toi/ (reference date: 06.02.2012).
9. Antipin G.K., Efimov V.N., Kozolup A.N. Software DINBOR. Attestation passport No.179 as of 1.07.2004г.

LIFETIME TESTS OF FUEL RODS WITH LOW NEUTRON POISONING

A.V. KLINOV, N.K. KALININA, N.Yu. MARIKHIN, V.V. PIMENOV, A.L.PETELIN, V.A. STARKOV, V.E. FEDOSEYEV, S.V. MAINSKOV
Research Reactors Complex, JSC "SSC RIAR"
Dimitrovgrad-10, 433510 - Russia

ABSTRACT

The paper presents the results of determination of power density, thermal flux density and burnup of fuel rods with low neutron poisoning that were obtained during the experiment performed in the SM reactor and computational modeling. Thermo-physical parameters of the fuel rods operation are considered and the key controlled test parameters are presented. It is shown that all fuel rods have been successfully tested and preserved their performance under the conditions corresponding to the operation in the upgraded SM reactor core.

Introduction

The SM reactor is a high flux research facility with a peak value of thermal neutron flux density equaël to $5 \cdot 10^{15}$ $cm^{-2} \cdot s^{-1}$. The core design allows the accumulation of radionuclides and conduction of loop tests. The unique features of the reactor are mainly conditioned by the use of a special cross-shaped fuel rod that is able to withstand a thermal flux up to 15 MW/m^2.

Over the last years, the SM reactor core has been upgraded to extend its experimental capabilities related to the high dose irradiation of the nuclear engineering materials. At the first stage, fuel rods with U-235 loading increased by 20 per cent were fabricated and tested. In this context, additional irradiation volumes were arranged in the core, all key design features of the reactor being retained [1].

The second stage of the SM reactor upgrade is aimed at the enhancement of conditions for the radionuclides accumulation by the increase in the neutron flux density in the reactor experimental channels approximately by 1.5 times due to the decrease in the core volume, the reactor capacity being retained. The second stage is related to the development of a new fuel rod using structural materials with a lower neutron capture cross-section than in a standard version. Application of these fuel rods can make it possible to reduce neutron poisoning in the core and, therefore, to increase a share of neutrons to irradiate specimens, as well as to compensate reactivity losses related to the increase of the neutron escape. Moreover, annular consumption of fuel assemblies will decrease by 30 per cent [2].

Fuel rod with low poisoning

JSC “SSC VNIINM” (with the specialists of JSC "SSC RIAR" involved) has fabricated dispersed fuel rods with low neutron poisoning [3] using the following as a nuclear fuel:

– uranium dioxide with Al grits (Option 1);

– uranium dioxide with Al grits, an Al displacer with a square cross-section is located in the fuel rod center (Option 2);

– uranium intermetallic compound with the grits of the Zr and Al intermetallic compounds (Option 3).

Free space under the fuel rod cladding is impregnated with the matrix material, Si-Ni-Al alloy (silumin). Stainless steel is used as a fuel rod cladding material. Figure 1 shows the fuel rod design of Option 1. Comparative characteristics of the SM standard fuel rod and fuel rods with low poisoning are presented in Table 1.

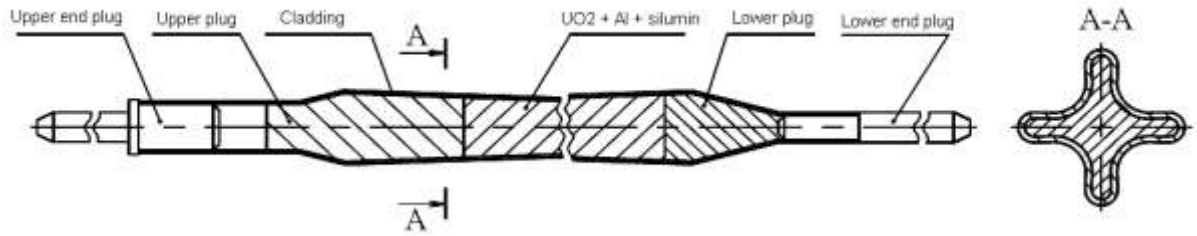

Fig.1. Fuel rod with low poisoning (Option 1)

The work is aimed at the obtaining of data to justify the choice of a design of fuel rods with low poisoning that are of high performance under the FA operation conditions in the SM upgraded core.

Parameter	Standard fuel rod	Options of fuel rods with low poisoning		
		1	2	3
Cladding thickness, mm	0,15	0,15	0,15	0,15
Fuel part length, m	0,35	0,35	0,35	0,35
Cross-section square, mm^2				
- fuel meat	8,05	7,12	4,29	7,12
- fuel rod	10,46	9,64	9,64	9,64
Fuel rod outer diameter, mm	16,57	17,26	17,26	17,26
Heat exchange area, m^2	0,0058	0,006	0,006	0,006
Fuel meat volume, cm^3	2,82	2,49	1,50	2,49
U-235 load in a fuel rod , g	6	5	4,5	5
Volume fraction of a fuel phase, rel. un.	0,31	0,25	0,45	0,5

Table 1. Comparative characteristics of fuel rods

Three experimental FAs (EFAs) with eight fuel rods of one option were fabricated to perform the tests. Irradiation rigs (IR) with EFAs were loaded into the loop channel installed in cell 2 of the SM reflector. Loop tests of EFAs were conducted one by one. The following was controlled during the tests: coolant flow rate through the channel, coolant temperature at the channel outlet and inlet, pressure at the channel inlet, pressure drop on the channel, readings of the fuel rod cladding failure detection system sensors.

Calculated parameters of tests

A key factor determining the fuel rods performance under irradiation is chemical compatibility of the fuel meat components among each other and their interaction with the cladding material. The available data show that the maximal allowable temperature of the UO_2+silumin composition is of the order of 430 ÷ 450°C (for fuel rods of Option 1 and 2), while for the $U(Al,Si)_3$+ silumin composition it is 550°C (for fuel rods of Option 3).

Preliminary calculation of neutron-physical conditions for the tests of fuel rods with low poisoning was performed using the SM reactor computational model created on the basis of the MCU code (MCU-RFFI/A version [5]). The calculation results show that the maximal thermal flux from the surface of the Option 1 fuel rods with low poisoning is 7,8±0,4 MW/m^2, for Option 2 – 9,1±0,5 MW/m^2, for Option 3 – 7,7±0,5 MW/m^2, calculated thermal capacity of the EFA being equal to 250±14 kW, 300±16 kW, 250±12 kW, respectively.

In modeling of thermal-hydraulic conditions for the EFA irradiation, techniques [6, 7] and code [8] that allows the calculation of a temperature field in the fuel rods with a complex cross-section profile were used. The techniques [6, 7] were tested for the departure from nucleate boiling based on the results of the in-pile experiments [9].

Figure 2 presents the dependencies of a maximal temperature of the fuel composition and cladding outer surface on the thermal flux density for three fuel rod options. The average coolant flow rate in the EFA is taken equal to 12,4 m/s, the coolant temperature at the EFA inlet is 50°C, that corresponds to the operation parameters of the thermally stressed standard FA of the SM reactor.

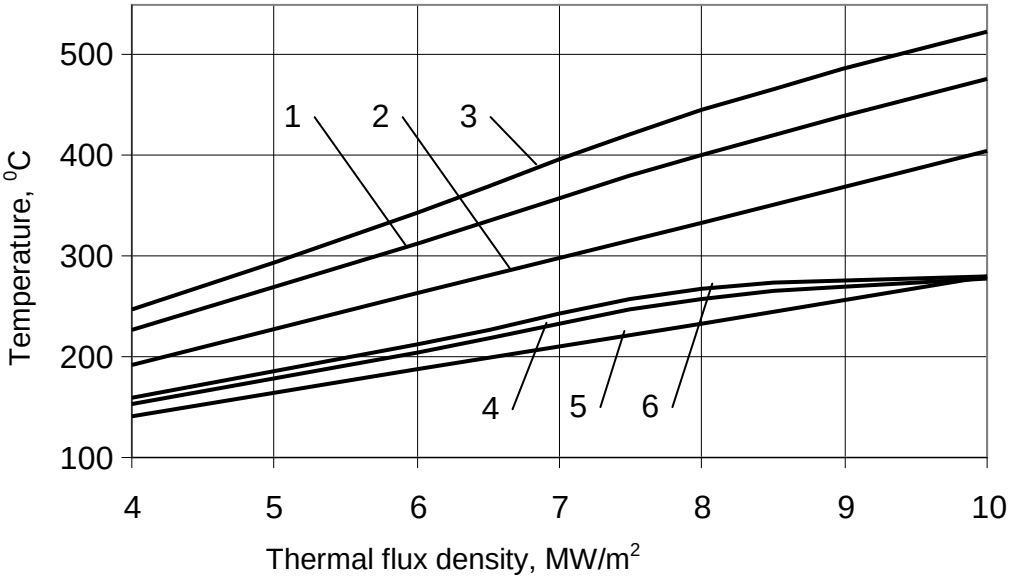

Fig. 2. Maximal temperature of the fuel meat (1,2,3) and temperature of the fuel rod cladding outer surface (4,5,6) as a function of maximal density of the thermal flux from the fuel rods surface: 1, 4 – Option 1; 2, 5 – Option 2 ; 3, 6 – Option 3.

Therefore, preliminary neutron-physical and thermal-hydraulic calculations identified the conditions under which at the maximal thermal flux density the maximal temperature of the fuel meat for options 1, 2 and 3 does not exceed the values of 395°C, 375°C и 435°C, respectively, while the cladding outer surface temperature doesn't exceed 260°C for all fuel rod options (Fig. 2).

Parameters of lifetime tests

Figure 3 shows a change of the EFAs power during the tests. General tendency of the power decrease is conditioned by the fuel burnup. The EFA power was determined based on the coolant flow rate and difference of temperatures at the EFA inlet and outlet. Table 2 presents the main test parameters.

Parameter	Option		
	1	2	3
Average coolant flow rate through the channel, m^3/h	7,7	7,8	7,7
Average coolant rate, m/s	14,4	14,6	14,4
Max coolant temperature at the EFA inlet, °C	75	56	50
EFA power, kW - average - max	 191 217	 225 257	 188 236
Max thermal flux density, MW/m^2	6,8	8,0	7,3
Max temperature of, °C - clad outer surface - fuel meat	 238 360	 215 333	 229 391

Table 2. Comparative characteristics of fuel rods

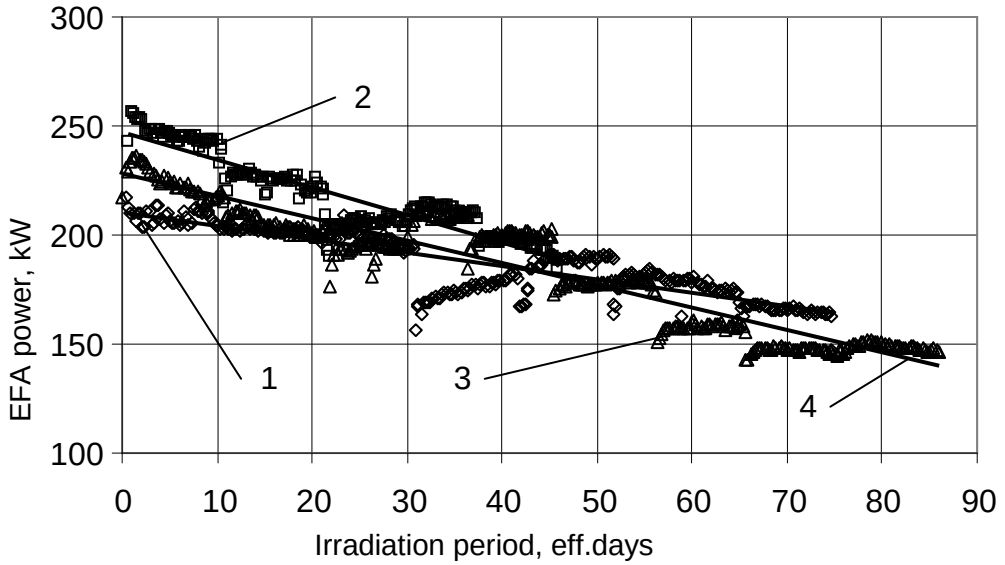

Fig. 3. Change in the EFA power with the irradiation time. 1, 2, 3 – power of EFAs with low poisoning fuel rods for Options 1,2 and 3, respectively, 4 – trend line.

Table 3 presents the results of calculation and experimental data. They show that the deviation of calculated values from the experimental data does not exceed 10%.

Option	Average power of EFA, kW	
	Calculation	Experiment
1	234±6	212±3
2	274±4	252±5
3	223±6	231±6

Table 3. Calculated and experimental power values

According to the calculated data, at the end of the tests an average and maximal fuel burnup (^{235}U decrease) in the EFAs makes up, respectively:

– Option 1 fuel rods – 50,6 и 57,4 %;
– Option 2 fuel rods – 40,7 и 44,6 %;
– Option 3 fuel rods – 57,4 и 64,2 %.

According to [10], the average fuel burnup in the unloaded standard FAs of the SM reactor makes up 37%. Therefore, the average fuel burnup in three EFAs achieved during the tests corresponds to the average fuel burnup in standard FAs.

Figures 4 and 5 present the graphs of the change of the maximal temperature of the fuel meat and outer surface of the thermally stressed fuel rods, on the assumption of the heat conduction consistency of the fuel meat and axial coefficient of power density non-uniformity.

During the irradiation (figures 4,5) the maximal temperatures of the fuel meat and outer cladding surface of the fuel rods with low poisoning, taking into account the experimental data on the coolant flow rate and temperature, changed within the following ranges, respectively:

– Option 1 – 360 - 260 and 238 - 167 ^{o}C;
– Option 2 – 333 - 250 and 215 - 162 ^{o}C;
– Option 3 – 391 - 240 and 229 - 143 ^{o}C.

The maximal temperature of the fuel meat and cladding outer surface in all three EFAs didn't achieve pre-test calculated values due to low initial thermal power of the EFAs and a bit increased coolant flow rate through the IR (see Table 2). Surface boiling of the coolant (saturation temperature is 260^{o}C) on all fuel rods during the EFA tests was not observed.

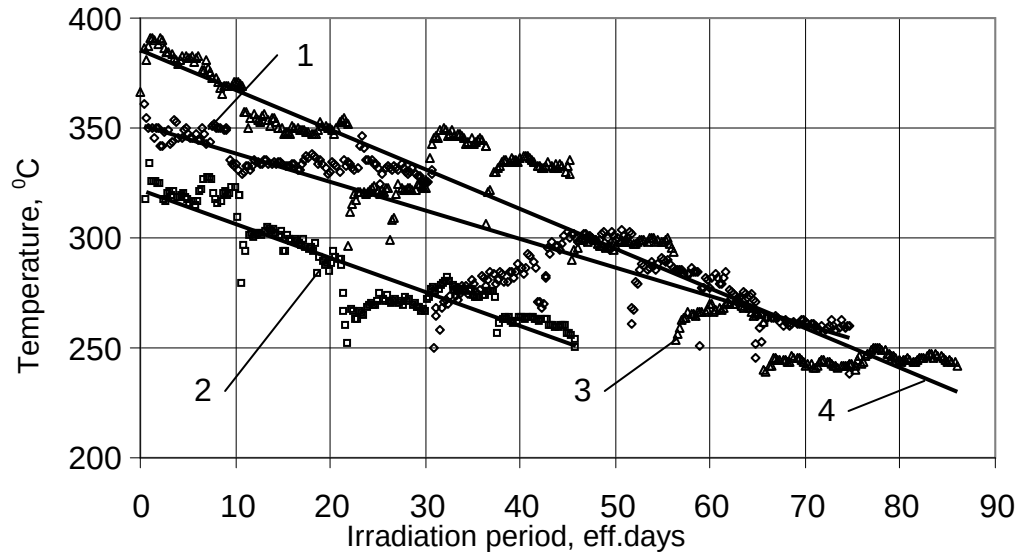

Fig. 4. Change of the maximal temperature of the fuel rod meat during irradiation: 1, 2, 3 – fuel rod options, 4 – trend line

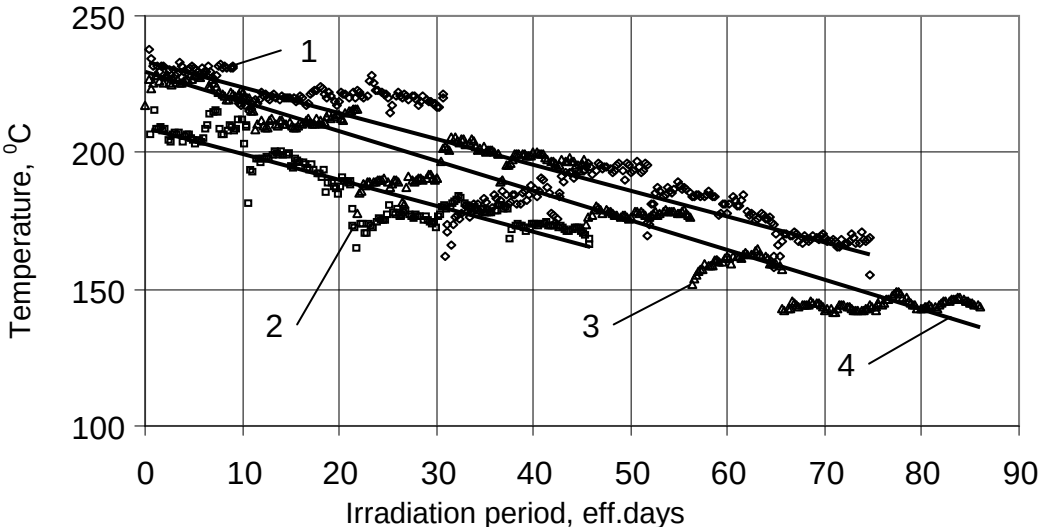

Fig. 5. Change of the maximal temperature of the fuel rod cladding outer surface during irradiation: 1, 2, 3 – fuel rod options, 4 – trend line

The coolant activity at the EFA outlet during the tests was stable, and the readings of the fuel rod cladding failure detection system in the channel with the IR didn't exceed the allowable value, i.e. no fuel rod cladding failure was detected.

Conclusion

It was demonstrated that all EFAs with low poisoning passed the loop tests and retained their integrity under thermal loads and fuel burnup depth that correspond to the operation conditions of the SM upgraded core:

– maximal thermal flux density from the fuel rods surface of Option 1 made up 6,8 MW/m2, Option 2 – 8,0 MW/m^2, Option 3 – 7,3 MW/m^2;

– average fuel burnup in the fuel rods of Option 1 made up 50,6%, Option 2 – 40,7%, Option 3 – 57,4%.

Therefore, the lifetime tests showed that the fuel rods with low poisoning in all options retained their integrity under the conditions similar to the operation conditions of the

upgraded SM core.

References

1. Klinov A.V., Tsykanov V.A., Starkov V.A., Pimenov V.V., Chertkov Yu.B. Upgrading of the SM Reactor Core to Solve the Material Science Tasks.//Atomnaya Energiya.-2002.-V.93.-No.3.-P.167.

2. *Tsykanov V.A., Klinov A.V., Starkov V.A., et al.* Features and Experimental Capabilities of the SM Reactor after Upgrading of its Core./Proceedings of the International Conference: "Research Reactors in the 21st century.". (Moscow, NIKIET, June 21–24, 2006).

3. *Volkov V.S., Klinov A.V., Starkov V.A., Morozov A.V. et al.* Development of the Fuel Rod with Low Neutron Poisoning for the SM High-Flux Research Reactor.// Atomnaya Energiya.-2009.-V.106.-Issue 6.-P.314–318.

4. *Samoylov A.G., Kashtanov A.I., Volkov V.S.* Dispersed Fuel Rods. Vol. 2. Design and Serviceability.- M.: Energoizdat, 1982.

5. *Gomin Ye.A., Gurevich M.I., Maiorov L.V., Marin S.V.* The MCU-RFFI/A Code with the Library of Constants DLC/MCUDAT-1.0.//Issues of Nuclear Science and Engineering. Series. Nuclear Reactor Physics.-2001.-Issue 3.-P.50-55.

6. *Starkov V.A., Fedoseev V.E.* Distribution of Temperature and Thermal Flux Density along the Perimeter of the Cross-Shaped Section Fuel Rods./Proceedings (Quarterly Proceedings) JSC "SSC RIAR".-2003.-Vol.2,-P.3-8.

7. *Garusov Ye.A., Grachev S.D.* Heat Removal from the Fuel Rod of the Cross-shaped Section./ LIYaF Preprint No.660.-L., 1981.

8. *Grachev V.D.* Some Issues of the Mathematical Realization of the Finite elements Method in the Reactor Physics Tasks./ Preprint RIAR-6 (652), 1986.

9. *Bobrov S.N., Spiridonov Yu.G., Makhin V.M., Grachev A.F.* Study into the SM Reactor Fuel Rod Behavior under the Conditions of the Departure of Nucleate Boiling./ Proceedings of JSC "SSC RIAR".-Dimitrovgrad, 1997.-Issue 1.-P. 75.

10. *Klinov A.V., Starkov V.A., Chertkov Yu.B. et al.* Tests of the SM Reactor Test Assemblies with Increased Uranium Load.// Bulletin of Higher Education Institutions. Nuclear Engineering.-2011.-No.3.-P. 28-36.

European Nuclear Society
56, avenue des Arts
1000 Brussels, Belgium
Telephone: +32 2 505 30 50 - FAX: +32 2 502 39 02
rrfm2013@euronuclear.org
www.rrfm2013.org